2-1-2017

Correlation between geometrical and structural properties of mixed oxide ultrathin nanotubes and their solar water splitting performance

Ayatullah Mohamed Adel Saleh Elsayed

Follow this and additional works at: https://fount.aucegypt.edu/etds

بسم الله الرحمن الرحيم

THE AMERICAN UNIVERSITY IN CAIRO
الجـامـعة الأمـريكـيـة بالقـاهـرة

School of Sciences and Engineering

Correlation between Geometrical and Structural Properties of Mixed Oxide Ultrathin Nanotubes and their Solar Water Splitting Performance

A Thesis Submitted in partial fulfilment of the requirements for the degree of
Master of Science in Mechanical Engineering

By:

Ayatullah Mohamed Adel Saleh Elsayed

Under the supervision of:

Prof. Mahmoud Farag (Thesis Advisor)
Department of Mechanical Engineering, The American University in Cairo
&
Associate Prof. Nageh Allam (Thesis Advisor)
Department of Physics, The American University in Cairo

December 2017

Abstract

The objective of this study was to study the effect of Nb alloying with Ti on the photoelectrochemical performance of the resulted oxide upon anodization. In this regard, nanotubes were grown on Ti-Nb alloy via electrochemical anodization and their corresponding photocatalytic behavior was investigated and compared with those grown on an ordinary Ti substrate. After preparing and optimizing the nanotubes dimensions for the required geometrical structure, the as formed tubes were annealed at different temperatures and in air), then characterized with respect to their morphological, structural, and photoelectrochemical properties. From the morphological and structural point of view, optimized and well aligned ultra-thin wall nanotubes were successfully synthesized on the surface of Ti-Nb alloy. To the best of our knowledge, these dimensions have not been reported before. One of the challenges was that the oxide layer formed on the surface of the alloy was not precisely identified in literature, where some authors reported the formation of combination of individual oxides (TiO_2 and Nb_2O_5), whereas, others claimed it was a mixed oxide $TiNbO_x$. Raman and X-ray diffraction test results confirmed the formation of individual anatase and monoclinic Nb_2O_5 phases. Detailed XRD analysis was performed and the crystallite size as well as microstrain were calculated and found to be minimal indicating negligible effect of lattice induced tension or compression. It is worth mentioning that insignificant structural changes are favorable to maintain good electron mobility. Hence, point defect equations were deduced and it was found that that oxygen vacancies were the prevailing ionic defects rather than electronic Nb compensation. From the aforementioned results, ultrathin wall nanotubes formed on TiNb alloy were achieved, for the first time, with clear representation of the oxide layer composition. Such oxide layer showed better stability upon annealing at high temperatures. Although, UV-Vis test results showed small or negligible enhancement in the absorption, profile the photo-electrochemical measurements showed much higher photocurrent for Ti-Nb oxide alloy than bare TiO_2 prepared at the same conditions for the sake of comparison. In conclusion, the Ti-Nb NTs showed enhanced stability over a wide range of temperatures, where the transition from anatase to rutile was shifted to higher temperature in addition to an increase in the photoconversion capability, resulting in a more efficient water splitting process.

Table of Contents

List of Figures

List of Tables

List of Abbreviations

1-D	One-dimensional
CB	Conduction band
DFT	Density function theory
EDX	Energy Dispersive X-ray spectroscopy
FESEM	Field emission scanning electron microscope
IPCE	Incident photon-to-current conversion efficiency
i-t	Current-time
I-V	Current-Voltage
NP	Nanoparticle
NR	Nanorod
NT	Nanotube
PEC	Photoelectrochemical
SCE	Saturated calomel electrode
SEM	Scanning electron microscope
VB	Valence band
V_O	Oxygen vacancy
UV-Vis	Ultra violet - Visible
WE	Working electrode
XPS	X-ray photoelectron spectroscopy
XRD	X-ray diffraction

Acknowledgements

Aya Adel Saleh

Chapter I

Introduction and Scientific Background

1. Chapter I: Introduction and Scientific Background

1.1. Problem Statement:

Currently, the main problem could be break down into three main issues. The climate change as one of the environmental concerns, fierce competition for the energy resources which might cause geopolitical conflict, and the shortage in energy supply for nearly 2-3 billion people around the world. Strategies to solve the energy crisis can be put down into two main tracks, developing new energy sources and maximizing energy efficiency at the same time of reducing the energy usage to its minimum [1]. In other words, two contradicting challenges facing humanity right now, which is increasing the standard of living and consequently the global energy consumption while at the same time reducing our greenhouse gas emission, in particular the carbon dioxide [2]. Fossil fuels such as the natural gas, coal, and oil are the primary source of energy with an amount of about 90% used mainly in transportation and industrial sectors to keep such high life style of mankind in the 21st century. Such depletion of these carbon-based resources will be on the expense of producing some valuable chemicals [2,3]. One approach is to mitigate the emission of greenhouse gases through converting carbon dioxide into fuel. However, this conversion suffers a lot of issues due to low energy content since carbon dioxide exists in very dilute conditions (~ 400 ppm in air) or could be present along with mixture of gases which requires large amount of energy to separate [4]. It was reported that the global energy consumption is expected to increase from 495 quadrillion British thermal units (Btu) that was recorded in the year of 2007 to estimated values of 739 quadrillion per year in the year of 2035. This in turn means power consumption rise from 16.6 terawatts (TW) to 24.7 TW and it is expected to further increase to 34 TW by 2050 [3,5]. Figure 1.1 shows the difference between energy consumption and energy demand [6]. Therefore, it is the main goal now to look for and explore alternative renewable and clean sources of energy instead of depleting fossil fuels to reduce the greenhouse gas emission and alleviate climate change raising environmental issues as well as mitigating the dependency on foreign oil [4,7, 8-9].
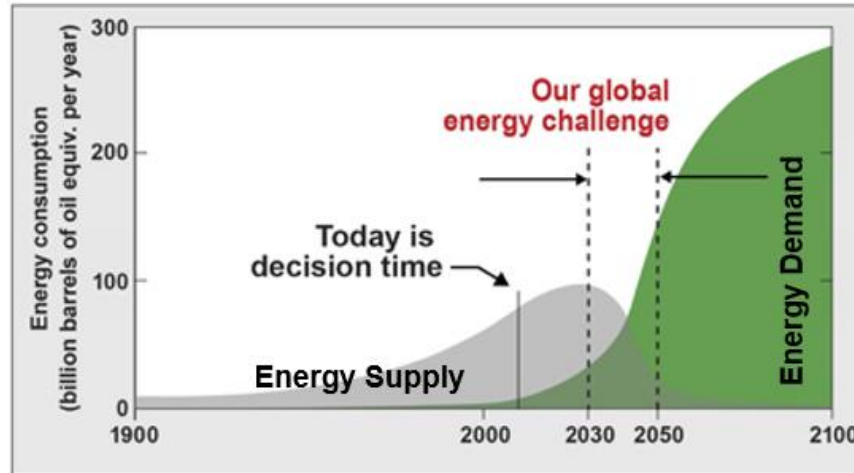
Figure 1.1. The energy supply and energy demand over years [6].

1.2. Clean Energy Resources:

Various alternative energy resources are available such as geothermal, wind, hydropower and solar. Although they are sustainable and relatively clean compared to fossil fuels, they possess some drawbacks which limit their use and make it somehow challenging to replace the fossil fuels. For instance, geothermal is very expensive to extract since it is limited in lifetime. Noise and ecosystem disruption are caused by wind turbine blades in addition to difficulty in storing the generated electricity. Hydropower as well suffers from high cost and consequent environmental issues [10].

1.3. Solar Energy Resources:

Unlike the previously mentioned energy resources, solar energy is plentiful, unlimited, free and renewable which could be used to generate energy in the form of either electricity or heat. Solar energy arriving the earth in only one hour exceeds the world energy consumption in a whole year [11]. (~1.2 × 10 14 kJ are received at the Earth's surface every second)

Accordingly, it can provide enough power to the whole humanity for several hundreds of times. Yet, it is unpredictable and intermittent as it depends on many factors, for example, the coordinates of the place, time during the day, and which season of the year are we in [12,13]. Another drawback of the solar energy is the low density of solar irradiation per unit surface area of the Earth.

Figure 1.2 shows the solar irradiation distribution in the word. It can be seen that the Middle East, Africa, Australia, the Indian subcontinent, Central America, and South America have the

abundance of solar energy resources. 6 kWh/m^2 of solar radiation is delivered to these areas per day. In comparison, Europe, Asia, and Northern America receive relatively lower amount. Moreover, the availability of solar energy over time near equatorial regions is slightly fluctuating and therefore these consider promising locations to install fuel refineries.
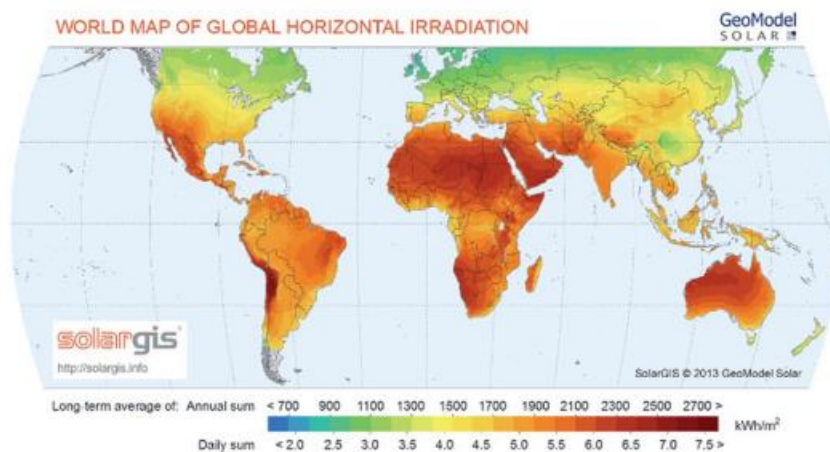
Figure 1.2. World map of horizontal solar radiation globally [14]

Solar energy can be utilized in different applications. For example, incident light can produce direct current electricity using semiconductor materials as photons can be used to actuate chemical reactions in photo-electrochemical, photolysis, and photo-catalytic reactions. Accordingly, it is essential to develop continuous, storable, renewable and clean energy source in which efficient harvesting and storage is achieved in order to satisfy the energy demand. One solution is to use such renewable resource "sun" to split water into hydrogen and oxygen [14].

1.4. Water:

Water is considered the solar refinery second key resource. It can be converted directly to hydrogen and oxygen by a various number of solar technologies. On the other hand, water can be consumed directly during CO_2 reduction (without intermediate forming of hydrogen) to various fuels. Generally, locations with high availability of solar resource may not possess high availability of water. However, water withdrawal could be a source of water giving that transportation cost to the solar refinery is relatively low compared to the overall process cost [4].

1.5. Hydrogen:

In 1788, Hydrogen is named by Lavoisier which comprises of two Greek words, 'hydro' means water and 'genes' means born of. It was once mentioned by an electrochemist called J.O'M

4

Bockris in a brainstorming session held at the Technical Laboratory of General Motors, Warren, MI, "We should be living in a hydrogen society", and in reply to that, Neal Triner declared: "There will be a hydrogen economy". Hydrogen economy means that hydrogen would be considered as the energy carrier which is to be transported wherever easily. Future transportation fuel selection criteria includes safety, economics, efficiency, versatility and environmental friendly. Additionally, this new energy carrier must link the renewable energy sources to the consumption sectors and easily replace the hydrocarbons market avoiding the big hustle of such switch. This means it has to be produced, transmitted, and stored in an easy, cheap, clean, renewable, and more efficient way than currently existing fuels [15]. Hydrogen is considered an excellent energy carrier as it has many advantages such as: elevated energy yield; availability and can be obtained from different sources in large quantities and at high efficiencies (water or biomass); clean and environmentally friendly as it does not produce any greenhouse gases or pollutants that may harm the environment; easy to store (gas, liquid, and metal hydride form); high transportation capabilities (pipelines or tanks for long distances); can be efficiently converted into other energy forms in more than one way [2]. Although hydrogen has unique properties that qualifies it to ideally alter the conventional energy sources, yet it has some drawbacks limiting its use as fuel such as additional costs associated with compressing hydrogen to be stored as compressed gas or liquid, shortage of available infrastructure for hydrogen, lack of dependence on renewable generation since its production is mainly relying on fossil fuels through natural gas reforming. Accordingly, enormous efforts have been carried out to study the possible methods of producing hydrogen using renewable resources [2,15]. The hydrogen production from hydrocarbons is done via three main techniques: autothermal reforming, hydrocarbons steam reforming, and partial oxidation. Such processes involve the emission of both carbon monoxide and dioxide as well as hydrogen. Hydrogen produced can be enhanced in terms of quantity and purity quality via preferential oxidation of exiting CO and water-gas shift. This promotes the use of solar energy to obtain clean renewable fuel like hydrogen through water electrolysis, thermochemical water splitting, photo-catalytic water splitting, and photo-electrochemical water splitting [4].

Solar energy can be directly converted into chemical energy through splitting water into oxygen and hydrogen by sunlight in photoelectrochemical cell. This is considered one of the most promising strategies to supply clean and sustainable energy in the future. For a device to store solar energy, it is important to make use of incident solar radiation so that a chemical reaction can be

carried out and therefore that energy can be stored as a chemical fuel [16]. In this respect, coupling solar irradiation to water splitting through electrochemical process is of increasing interest. There are two available routes for this process. The first one is called "indirect solar-to-hydrogen production" at which the conventional solar panels are used to run electrolyzers. The second one is called "direct solar-to-hydrogen production" at which a single device is developed to carry out both light absorption and consequently water splitting. An indirect approach receives an advantage of using conventional, tried-and-tested technologies, however, it suffers from the efficiency losses due to the extra step involved, as a photovoltaic cell is firstly used to generate electricity which is then consumed through a following electrolysis step in a different device. Therefore, recently, a lot of activities have been exploded targeting the evolution of devices for direct solar-to-fuels. This method will hopefully become more efficient compared to other indirect methods. Furthermore, the direct solar-to-fuels devices can implement 'artificial photosynthesis', where these devices can capture and store the energy of the sunlight through a chemical bond acting as "solar fuel" which is hydrogen in this case [14].

Producing hydrogen by one of the most promising technologies which is solar photoelectrochemical (PEC) can potentially secure the supply of a cost-effective, domestically produced, and clean energy carrier taking the advantage of the huge amount of the solar radiation (120,000 TW) that strikes the surface of the earth continually [4,17]. One of the main criteria for the devices used to split water is to be cheap for production and operation, as they become widely adopted. Therefore, electrocatalysts that comprise only earth-abundant, inexpensive elements must be developed for water splitting. Accordingly, special concern towards the investigation of the progress of such electrocatalysts is given, with emphasis on the incorporation of them into photoelectrocatalytic water splitting systems. The challenges that may face the development of these devices should be taken into considerations as well [14].

1.6. Photoelectrochemical (PEC) Water Splitting:

1.6.1. Fundamentals of PEC Method

Recently, the increase of the human population and consequently the energy consumption requires a greater demand for the source of clean energy. Sustainable and clean energies are essential in the future for ecotopian society. Jules Verne once mentioned in his book that: "...water will one day be employed as fuel, that hydrogen and oxygen which constitute it, used singly or together, will

furnish an inexhaustible source of heat and light...". In 1972, this came true when splitting water into hydrogen and oxygen through photoelectrochemical (PEC) method was investigated by Fujishima and Honda [18]. H_2 is the most optimum solution to the demand of energy in the future, especially when it sourced in an efficient and clean manner. However, for the PEC method, a bias on the electrocatalyst must be applied, powder of TiO_2 in 1979 was found to split water without applying a bias voltage when exposed to sunlight using a sacrificial reagent. This uncovered the most economical and promising method to produce H_2. Figure 1.3 shows the number of publications concerning photocatalytic process in the last decade indicating a tremendous progress in this process. Review articles summarizing the progress of the semiconductor photocatalysis are being frequently published [19-23].
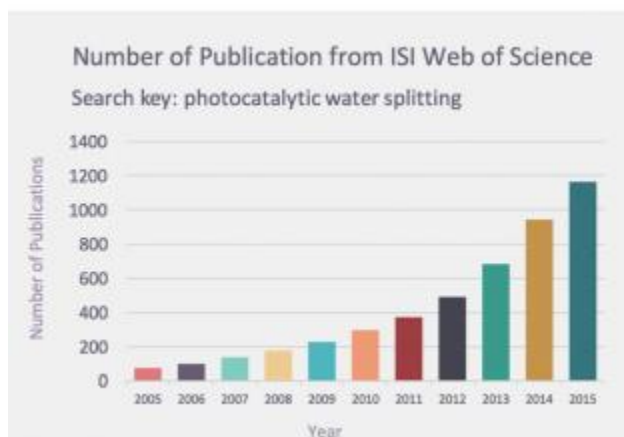
Figure 1.3. Number of yearly publications about photocatalytic water splitting for the last decade [24].

Photocatalytic water splitting depends on the high redox capacity of photogenerated electron-hole (e-h) pairs. According to where the excitation initially takes place, photocatalytic water splitting was classified by Linsebigler et al. [19] into two classes. For the first process which called the **sensitized photoreaction**, the initial photoexcitation occurs in a catalyst substrate before the excited electron is being transferred to a ground-state molecule. The second one referred as the **catalyzed photoreaction** at which the initial photoexcitation takes place in the adsorbate molecule before interacting with the catalyst at the ground-state. Regarding the first case, the semiconductor electronic structure plays a vital role for water splitting. When semiconductor materials absorb a photon having energy higher than that of a bandgap energy, a valence band (VB) electron is excited and transferred into the conduction band (CB), and consequently a hole is created in the VB (Figure 1.4). Due to the existence of the bandgap, the migration of the photogenerated (e-h) pairs to the

7

semiconductor surface occurs before the recombination, where these pairs can exchange energy and charge with adsorbed species (O_2, O_2^-, OH^-, etc.). New high redox capacities species (O_2^-, OH, etc.) will be created. These species are the reagents to produce H_2 and O_2. A direct interaction between the e-h pairs and these reagents can also be occurred. Eq 1.1 represents the overall process of photocatalytic water splitting through the following reaction;

$$2H_2O(l) \xrightarrow{\text{photon energy} > 1.23 \text{ eV}} O_2(g) + 2H_2(g) \qquad (1.1)$$
$$\Delta E^0 = 1.23 \text{ V}$$
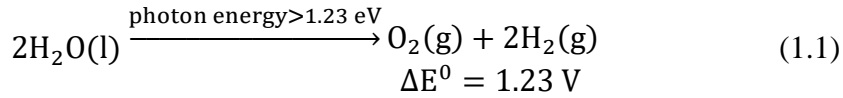
where ΔE^0 is the equilibrium potential under standard conditions. The reduction and the oxidation half-cell reactions are involved through the path of PEC to water splitting (Equation 1.2 and 1.3).

$$\text{Reduction: } 4H^+(aq) + 4e^- = 2H_2(g) \qquad (1.2)$$
$$\Delta E^0 = 0.00 \text{ V vs. SHE}$$

and
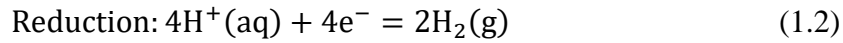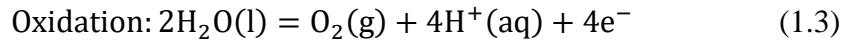
$$\text{Oxidation: } 2H_2O(l) = O_2(g) + 4H^+(aq) + 4e^- \qquad (1.3)$$
$$\Delta E^0 = 1.23 \text{ V vs. SHE}$$

The redox potentials change under different conditions and this can be described by Nernst equation (Equation 1.4):

$$E^e = E^0 - \frac{RT}{zF} \ln \frac{\text{oxidized}}{\text{reduced}} \qquad (1.4)$$

where E^e is the electrode potential, R is the universal gas constant, T is the temperature, z is the number of moles of electrons involved in the reaction, and F is the Faraday constant. In this respect, owing to qualified photocatalysis, the CB potential level must be more negative compared to the potential of the H^+/H_2 for the reduction to proceed (Equation 1.2), whereas the energy level of the VB must be more positive compared to the potential of OH^-/O_2 to let the oxidation proceed (Equation 1.3). Therefore, the bandgap criteria for photocatalysis is related to the lower potential difference which is 1.23 eV (Figure 1.4). A lot of semiconductor materials can meet the criteria of the bandgap but the alignment of the band misses the levels of the redox of water. However, some semiconductors could be eligible for photocatalytic water splitting as the H^+ (pH value) concentration can alter the reaction potential (Equation 1.4) [24].
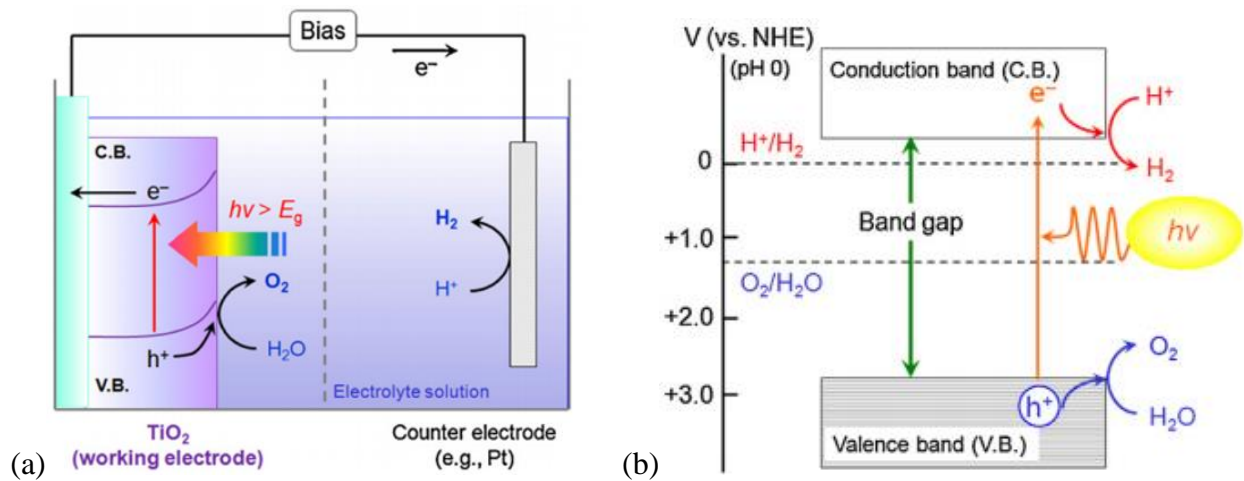
Figure 1.4. Schematic representation of the process of photocatalytic water splitting: (a) PEC water splitting by a photoanode, and (b) Overall water splitting basic principle on a semiconductor [25].

1.6.2. Requirements for PEC Semiconductor Electrodes (the four criteria):

As mentioned above, photocatalyst material plays essential role in determining the efficiency of the conversion of water photo-electrolysis. Hence, applying material science and engineering to photoelectrode materials is of great importance to boost hydrogen production using water and solar energy. Generally, the two main functions required in a PEC photoelectrode material are:

- Optical function to capture as much as possible of the solar spectrum;
- Catalytic function for the electrolysis and decomposition of water into hydrogen and oxygen.

For the photoelectrode material to satisfy the above functions, some requirements need to exist in the material such as band gap, flat band potential, Helmholtz potential, electrical resistance, Schottky barrier, microstructure, and photocorrosion and chemical corrosion resistance. These electrochemical and semiconducting properties can be achieved by semiconductor material and consequently they are considered as photoelectrode for PEC and made of oxide material to maintain their performance for prolonged duration [26,27].

Regardless the basic criteria, Goldilocks principle must be fulfilled for efficient photocatalysts of water splitting. This principle is: (a) high efficiency of photon-harvesting in the region of the visible light; (b) charge carriers' good mobility; (c) e-h pairs with low recombination rate; (d) plentiful active sites along with rapid exchange rate of energy and charge with other species [24].

9

Accordingly, it is essential to fabricate materials to satisfy all of the above-mentioned properties for the photo-electrode to perform in the highest efficiency possible. Hence, photoelectrodes are to be fabricated in a way to ensure combination of high efficiency, low cost, ease of fabrication, and durability. Such objective requires exploring new processing techniques as well suitable characterization methods to examine the photoelectrochemical properties of the photoelectrodes. Additionally, the materials of such photoelectrodes needs to be readily available where needed such as earth-abundant elements [26,27].

In this regard, Titanium dioxide semiconductor has been extensively studied the past 30 years for photocatalytic reactions [27]. Some of its issues were resolved while others are still under research. The following section of literature review, we will be covering in detail the various efforts to produce efficient photoelectrodes for hydrogen through solar water splitting.

Chapter II

Literature Review

2. Chapter II: Literature Review:

Having discussed the basic background for photocatalytic water splitting, summarizing the photoelectrochmical conversion process into three essential reaction steps: (i) the generation of the electron-hole pair, (ii) the separation and transport of the electron-hole pair, and (iii) the surface engineering and the corresponding required characteristics of the photoelectrodes, a survey on what have been done so far to obtain an efficient photoelectrode is presented in the following section.

Some efforts were exerted to modify crystal structure or introduce another material in order to enhance the absorption and broaden the spectrum of the light being absorbed. Other attempts were to passivate surface traps, create shorter lateral length, providing unidirectional pathway for the charge carriers, and develop heterojunctions to improve charge carrier separation and transport. Additionally, certain crystalline facets are being created in order to boost reaction occurring at the surface of the photocatalyst through enhancing the adsorption of the reactants, and desorption of the products. This factor relies on the number of the crystal surfaces and their quality in the semiconductor being studied [28].

2.1. PEC Electrode Structures:

2.1.1. One-Dimensional Structures (Nanotubes, NTs):

Semiconductors in the nano scale including zero-dimensional nanoparticles, one-dimensional nanotubes, nanowires, nanorods, two-dimensional nanosheets and the three-dimensional construction of these structure assembly such as mesocrystals have superior photocatalytic properties. It is obviously understood that materials in the nanoscale have higher surface areas available for any kind of reactions, particularly one-dimensional as well as two-dimensional materials having dangling bonds [24,28]. It was found that one-dimensional (1-D) structure has advantages compared to two-dimensional structure such as planar compact metal oxide in the sense of higher surface area since nanotubes allows for larger surface area to be exposed to electrolyte as the inner surface of the tube participate in the reaction between the electrolyte and the photoanode while at the same time it is not far away from the metal substrate. This also favors the nanotube structures (NTs) over nanorods (NRs). NTs would also possess higher light absorption due to increased optical path length within the layer because of strong light scattering [29]. The collection of the photogenerated electrons is crucial for efficient photo conversion. Studies showed

that quicker electron transfer from the oxide surface to the metal substrate and lower charge carrier recombination were attained for 1-D nanotubes structures in comparison with 0-D nanoparticles as this geometry has lower grain boundaries across which charge carriers will have to pass. In other words, the nanotubular architecture provides some order and interconnections for the path of the charge carriers, hence reduce the randomness of the grain boundaries and such structure lowers the losses of charge carriers crossing grain boundaries [27,30,31]. Electron efficiency of nearly 100% at the bottom of 1-D layer was recorded by Mukul and Hongshan [29]. Wang et al. [28] investigated the difference between well aligned nanotube structures and random nanoparticles and found that nanoparticles had higher defects, surface states and grain boundaries acting as sources of trapping and detrapping sites along the pathway of the charge carrier transport and lead to charge carrier losses by recombination and eventually reduce collection efficiency. Moreover, 1-D structure can be easily prepared via very simple process called "Anodization". This makes the fabrication easy and cost effective to be produced on a large scale [27]. Among the advantages of nanotubes and the production technique "anodization" is that their morphological parameters can be easily adjusted and controlled. It is important to attain nanotubes with certain dimensions for several reasons. Small wall thickness which is in the range of the summation of width of the depletion layer and the diffusion length is favored to avoid recombination. As charge carriers generated at the material surface within such retrieval length will escape recombination. TiO_2 nanotubes with wall thickness of around 20 nm are mostly prepared by Grimes group so that the transport distance (10 nm) would be shorter than the retrieval length. As a result of reducing recombination, quantum efficiency will increase. However, minority carriers might get trapped in the states at the surface [30,31]. A proposed schematic for the charge carriers walk mechanism was given for nanotube (NT) and nanoparticle (NP) structures (Figure 2.1). The NTs are well arranged in an array perpendicular to the metal substrate. Accordingly, electrons would move rapidly in one direction from top to bottom of NTs without having to go through any of the other 3D network of nanoparticles [27,29,32].
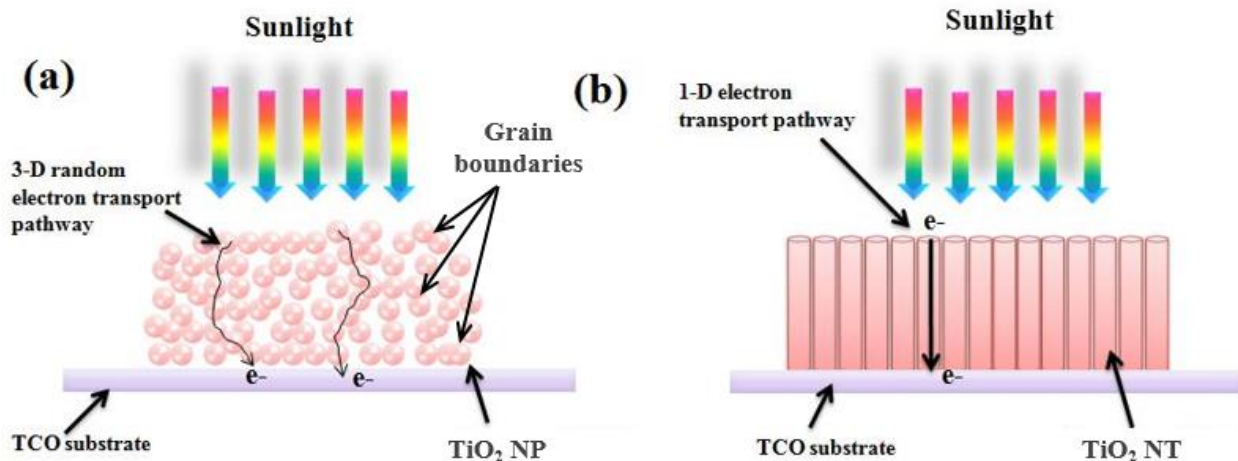
Figure 2.1. Schematic representation of the electron transport in TiO$_2$ NP based photoelectrode; (b) electron transport in TiO$_2$ NT based photoelectrode [29].

2.1.2. Nanotubes Preparation:

2.1.2.1. Anodization Process and its Advantages:

One of the distinguished technologies to obtain 1-D nanostructures is **anodization**. It is an electrochemical process to produce self-ordered structures in various sizes ranging from nanometers to as large as micrometers. It is widely studied due to its simplicity, easiness, and capability to scale-up. Several self-organized structures have been prepared via anodization such as nanopores and nanotubes whether on top surface of pure metal or alloy [33]. Controlling the composition, concentration, and pH of the anodization electrolyte, as well as applied voltage and time will lead to the formation of wide range of 1-D structures with controlled diameter, wall thickness, and length. In order to have control over the obtained 1-D structures, clear understanding of the process have been developed. The following section will explain in detail the mechanism of nanotube formation via anodization. Eventually, this will enable us to design and develop a protocol for the fabrication conditions of desired dimensions [33,34]. Numerous studies reported the formation of TiO$_2$ nanotubes on surface of titanium with various diameters and lengths in different electrolyte types (aqueous or organic) [35-42]. Also, self-organized and ordered nanotubes formed on the surface of metal alloys such as Ti-Nb, Ti-Nb-Ta-Zr, and Ti-Zr were reported [43-45]. For this reason, a comprehensive survey for the influence of these factors on the resulting nanotubes dimensions and morphology will be discussed later in section (2.1.2.3).

14

2.1.2.2. Nanotube Formation Mechanism:

Mechanism of nanotubes formation is divided into several stages as shown in Figure 2.2. First, oxidation occurs due to metal interaction with O^{2-} or OH^- ions (from H_2O) of the electrolyte at the metal surface. These anions continue to interact with metal at the metal/metal oxide interface. At the same time, metal cations will start to migrate from metal/ metal oxide interface towards metal/electrolyte interface due to the effect of electric field. The applied electric field will lead to oxide dissolution located at the interface of metal oxide/electrolyte as a result of metal-oxide bond weakening and polarization, called "field-assisted dissolution". Simultaneously, chemical dissolution occurs owing to electrolyte containing pitting elements such as Fluoride ions (F^-) which is essential to the formation of nanotubes over the expense of nonporous structures. At the beginning, field-assisted dissolution prevails chemical dissolution since the oxide layer is thin over which electric field exists. Naturally, there is a competition between rate of metal oxidation and the rate of chemical dissolution of metal oxide. When the rates of oxide formation at the bottom (metal/metal oxide interface) and oxide dissolution at the top (metal oxide/electrolyte interface) become equal, nanotubes grow at steady state. Hence, the nanotubes growth is governed by the rate of diffusion of solution and the electric field. And in case of alloys with different phases, these processes preferentially occur at certain locations of the alloy. Generally, the nanotube layers are formed through eating away the metal substrate. Nanotube formation is dependent on the rate of chemical dissolution, it cannot be neither too high nor too low, since it decreases the metal oxide layer (known as the barrier layer) thickness and hence maintain the oxidation and field-assisted dissolution going (both referred to as electrochemical etching). The rate of chemical dissolution depends on the concentration of F^- ions as well as pH of the electrolyte. Knowing that rising the concentration of F- or having more acidic electrolyte (more H^+) will in turn increase the rate of chemical dissolution. As for the electrochemical etching, it is controlled by the potential of the anodization in addition to the electrolyte concentration. Applying higher potential entails higher F^- content in the electrolyte [45-47].
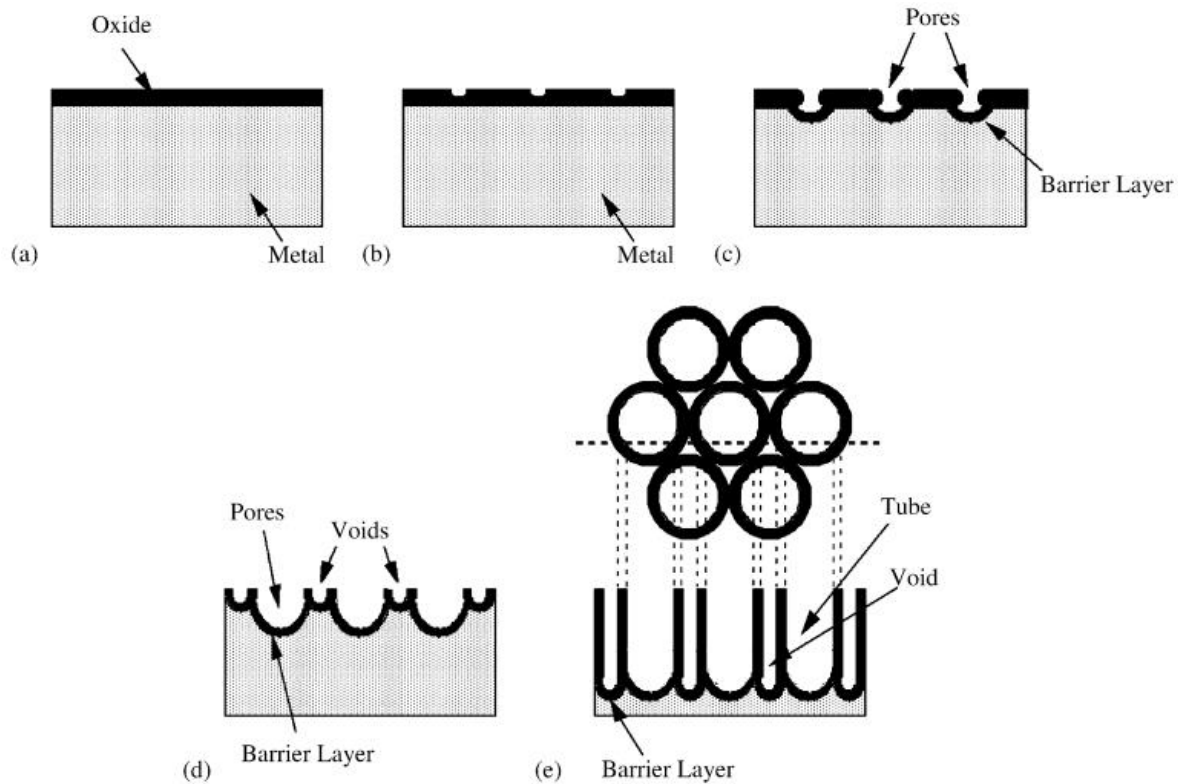
Figure 2.2. Schematic representation of a nanotube array evolution at constant anodization voltage: (a) formation of oxide layer; (b) formation of pit on oxide layer; (c) pit growth into pores with scallop shaped; (d) metallic part between field assisted dissolution and pores undergoes oxidation; and (e) top view of fully developed nanotubes array [45].

2.1.2.3. Anodization Factors affecting NTs Dimensions:

The type of electrolyte is considered one from the most important factors that affect the final structure of the NTs arrays formed by the anodization process. Acevedo-Pena et al. [48] showed that varying the electrolyte composition resulted in a different TiO_2 NTs morphology. Wherein, increasing the concentrations of NH_4F and the content of H_2O in Ethylene glycol based electrolytes at anodization voltage (30 V) and time (2 h) resulted in a transition in the morphology of TiO_2 from a nanoporous structures to a nanotubes and end with a sponge film [48], as shown in Figure 2.3.

16
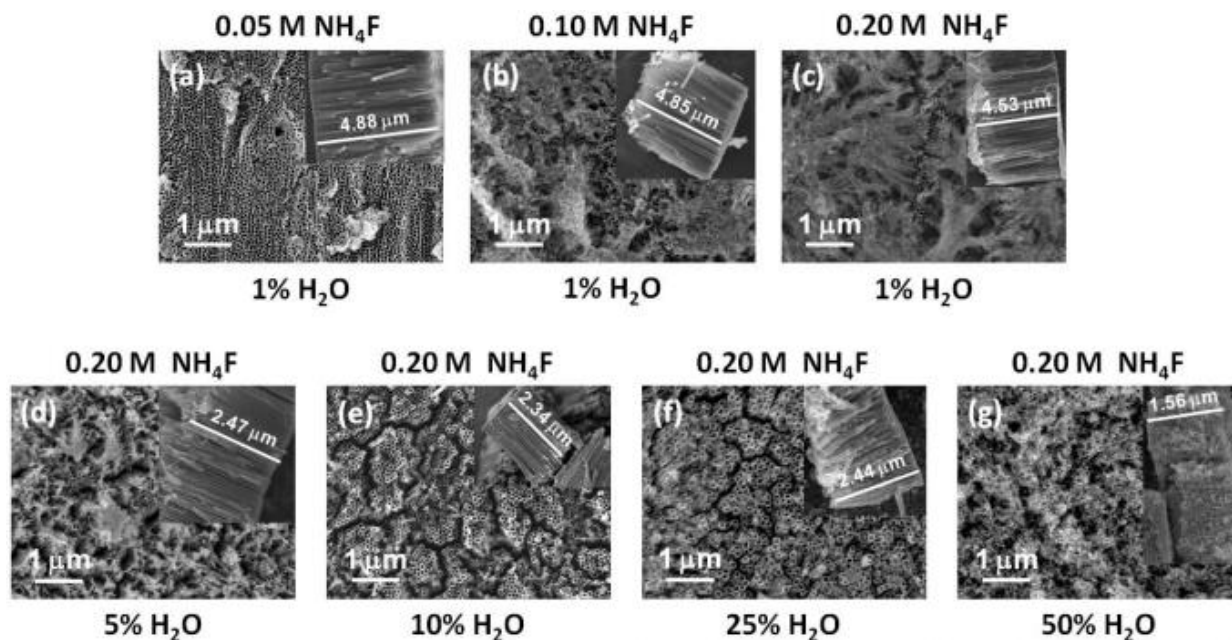
Figure 2.3. Effect of electrolyte composition in terms of amount of NH_4F and H_2O percentage (shown on each figure) on the obtained morphology of TiO_2 when anodizing at 30 V for 2 h, before heat treatment [48].

In another study, Deyab et al. [49] proved that the dimensions of Ti-Mo-Ni mixed oxide NTs arrays fabricated by anodization in a formamide-ethylene glycol based electrolyte are dependent on the composition of the electrolyte. Wherein, using a volumetric ratio of formamide to ethylene glycol (75:25) at anodization time (18 h) and voltage (20 V) resulted in 8.5 μm nanotubes length in comparison with 4.0 μm nanotubes length when using equivolumes of ethylene glycol and formamide at the same anodization conditions [49]. It worth mentioning that Ning et al. [50] had to change the composition of ethylene glycol based electrolyte in order to obtain Mn-doped TiO_2 NTs arrays similar in morphology to that of the pure TiO_2. Wherein, doping TiO_2 with manganese increase the solubility of the oxide, thus, decreasing the dissolution ability of the electrolyte (by decreasing the water content) was essential to obtain Mn-doped TiO_2 NTs with the same morphology as that of pure Titania NTs [50].

The length and the diameter of the NTs formed by electrochemical anodization are function of the **dopant content** in the bare Ti [51]. Jang et al. [51] reported that Ti-Nb alloy with different concentrations of Nb (10 wt%, 20 wt%, 30 wt% and 40 wt %) anodized in a 1 M H_3PO_4 electrolyte with 0.8 wt % NaF at anodization time (2 h) and voltage (20 V) showed an increase in the average tube length when increasing the Nb content. Tubes lengths of 730 nm, 940 nm, 1.5 μm and 2 μm

17

in case of using Ti-Nb alloy with Nb content 10 wt%, 20 wt%, 30 wt% and 40 wt %, respectively were obtained [51]. Along the same line, the pore diameter of the NTs varied with the Nb content, whereas in case of 10 wt% Nb content a NTs with diameter size 225 nm were obtained, while in case of higher Nb content a bimodal size distribution of tubes with 220 nm diameters surrounded by smaller tubes (55 nm diameter) were obtained, as shown in Figure 2.4. It was noticed that the formation of the smaller tubes increased with increasing the Nb content, and were located in areas where nucleation had not occurred which indicated its formation in a secondary nucleation process [51]. Oppositely, Jin et al. [52] reported that changing the Nb content in TiO_2 did not affect the dimension of the formed NTs by anodization in ethylene glycol and NH_4F electrolyte at anodization time (0.5 h) and voltage (60 V).
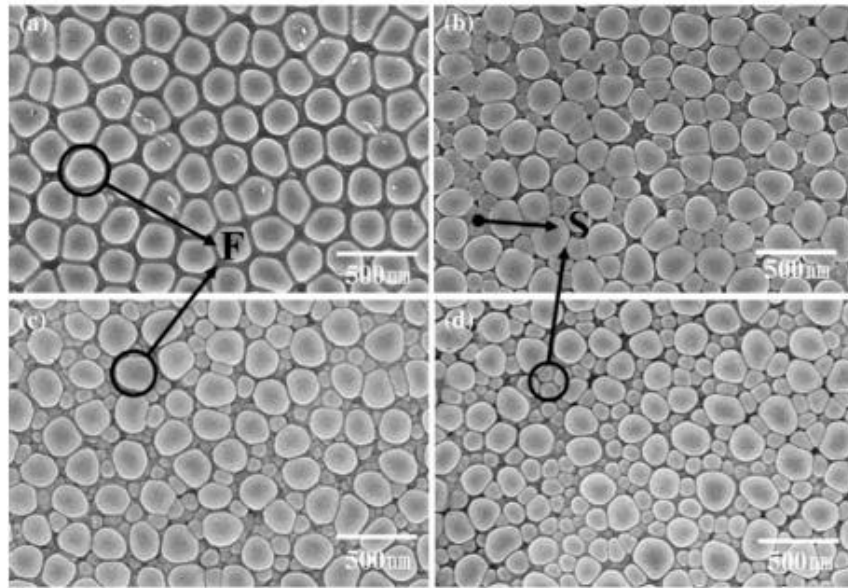
Figure 2.4. SEM bottom-view images for the formed nanotubes via anodization of Ti alloy with different Nb content (a) 10, (b) 20, (c) 30, and (d) 40; in 1 M H_3PO_4 + 0.8 wt.% NaF (F and S refer to First and Second nucleated nanotubes, respectively) [51].

In this regard, it is worth mentioning that Xu et al. [53] found that single phase microstructure of Ti20Nb is more favorable for forming NTs than dual phase microstructure of the same alloy under different heat treatment conditions (furnace cooling and water quenching, respectively). Upon anodization at 20 V and 0.5 h in (0.5% HF aqueous solution) electrolyte, no NTs were formed in case of dual phase microstructure Ti20Nb alloy as shown in Figure 2.5a, while in case of single phase a uniform NTs with 120 nm diameter and 1 μm length were formed as shown in Figure 2.5b and Table 2.1. When using an electrolyte with weaker dissolution strength (0.5% HF aqueous

18

solution adjusted to pH 3.5 by ammonia) a NTs were formed in case of dual phase microstructure Ti20Nb, as shown in Figure 2.5c, however, the NTs formed in case of single phase microstructure were more uniform, longer and larger in diameter as shown in Figure 2.5d and Table 2.1. [53].

Table 2.1. Different anodization conditions and the corresponding resulted morphology [53].

Samples	Crystal Structure	Electrolyte	Voltage (V)	Time (h)	Tube length (μm)	Tube diameter (nm)
TiNbO-NT-1	Dual phase	0.5% HF aqueous solution	20	0.5	---	---
TiNbO-NT-2	Single phase	0.5% HF aqueous solution	20	0.5	1	120
TiNbO-NT-3	Dual phase	0.5% HF aqueous solution (adjust to pH 3.5 by ammonia)	20	0.5	1	92
TiNbO-NT-4	Single phase	0.5% HF aqueous solution (adjust to pH 3.5 by ammonia)	20	0.5	2	100
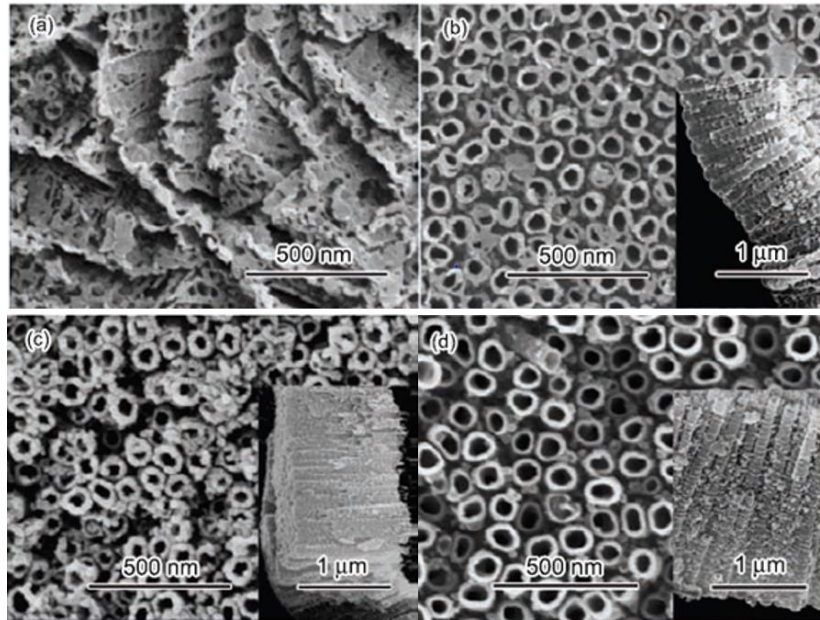
Figure 2.5. SEM top views of TiNbO-NT and TiO_2 -NT: (a) TiNbO-NT-1, (b) TiNbO-NT-2, (c) TiNbO-NT-3, (d) TiNbO-NT-4 [53].

On the other hand, Liu et al. [47] indicated that varying the content of Zr in Ti-Nb-Zr alloy affected the length and the diameter of the NTs formed by anodization in 1 M NaH_2PO_4 electrolyte containing 0.5 wt% HF. Table 2.2. shows that increasing the Zr content significantly increases the average length of the tubes at the different voltages used. However, increasing the Zr content from 5 wt % to 10 wt % caused a significant decrease in the average tubes diameter. While increasing the the Zr content from 10 wt % to 15 wt % slightly increase the tubes diameter at the different voltages used [47].

Table 2.2. Summary of average length and diameter of the nanotubes grown at different anodization voltages [47].

Samples	Anodization voltage [V]	Average length [µm]	Average diameter [nm]
Ti35Nb5Zr	30	4.75	170
	40	4.8	220
Ti35Nb10Zr	20	2.26	98
	30	5.23	150
	40	6.12	206
Ti35Nb15Zr	20	3.25	103
	30	5.84	153
	40	8.13	210

Another factor that affect the dimensions of NTs formed by electrochemical anodization is the **voltage** at which the process is carried. Whereas, increasing the anodization voltage causes the increase of average length and diameter of the NTs formed in the different compositions of Ti-Nb-Zr alloys, see Table 2.2. [47]. In another study, Ding et al. [54] showed that increasing the anodization voltage transform the porous structures formed in Ti35Nb alloy into nanotubular structures. Wherein, Figure 2.6 shows that porous structures were formed at anodization voltage (10 V), while at 15 V and 20 V a well aligned NTs were formed [54].
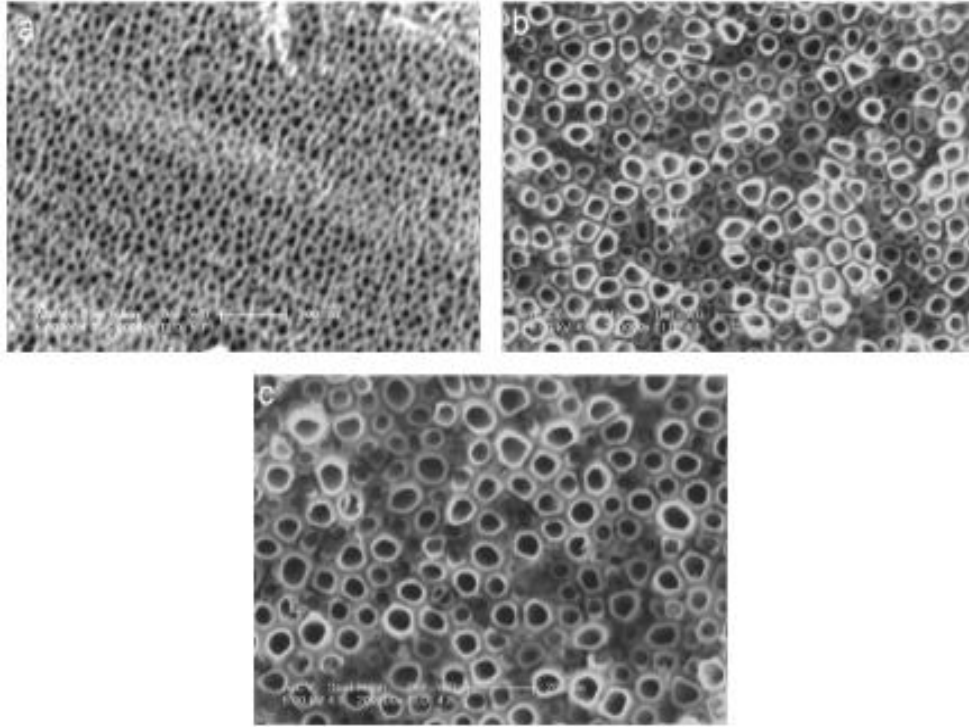
Figure 2.6. Anodization of Ti-35NB at different voltages produced Ti–Nb–O nanostructures: (a) 10 V, Porous without nanotubes, (b) 15 V, nanotubes and (c) 20 V, nanotubes [54].

Fornell et al. [55] showed that anodization of Ti-21Nb-11Sn alloy in ethylene glycol/water electrolyte containing 0.31 M NaF at anodization time (1 h) and anodization voltage (10 V) resulted in the formation of uniform NTs with unimodal size distribution, as shown in Figure 2.7a. However, on increasing the anodization voltage a bimodal size distribution of the tubes was noticed as shown in Figure 2.7b and Figure 2.7c, whereas tubes with large diameter are surrounded with small ones at 20 V and 25 V [55]. Figure 2.7d illustrates that increasing the anodization voltage increase the tube diameter as well as the tube length and result also in a bimodal size distribution of the NTs above 10 V. Whereas at 10 V a NTs with pore diameter (20 nm) and length (500 nm) were formed, while at 30 V a NTs with pore diameter (110, 40 nm) and length (1.7 µm) were formed [55]. On the other hand, Figure 2.8 shows the effect of variation of applied potential on the diameter and length of NTs formed at anodization time (12000 s) by Tsuchiya et al. [46]. Whereas the length and the diameter of the tubes increased linearly with increasing the applied potential from 5 V to 40 V, however, the length and the diameter increased steeply between 40 V and 50 V. Figure 2.8 also illustrates a rough surface when anodizing at 50 V in comparison with lower potentials [46].
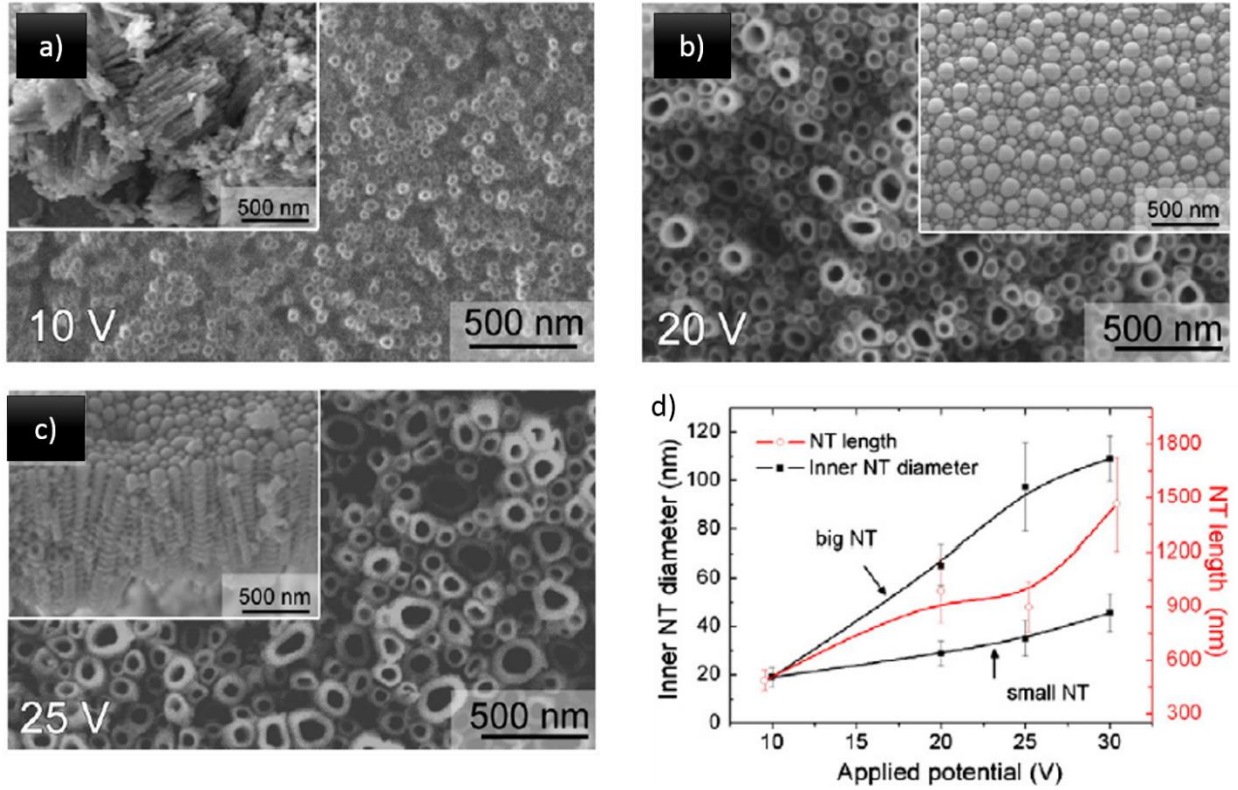
Figure 2.7. SEM top surface image of NTs formed on Ti-21Nb-11Sn via anodization at (a) 10 V, (b) 20 V, and (c) 25 V with insets of cross-section for (a) and (c) and bottom view for (b). Graph (d) effect of applied potential on the NT diameter and length [55].
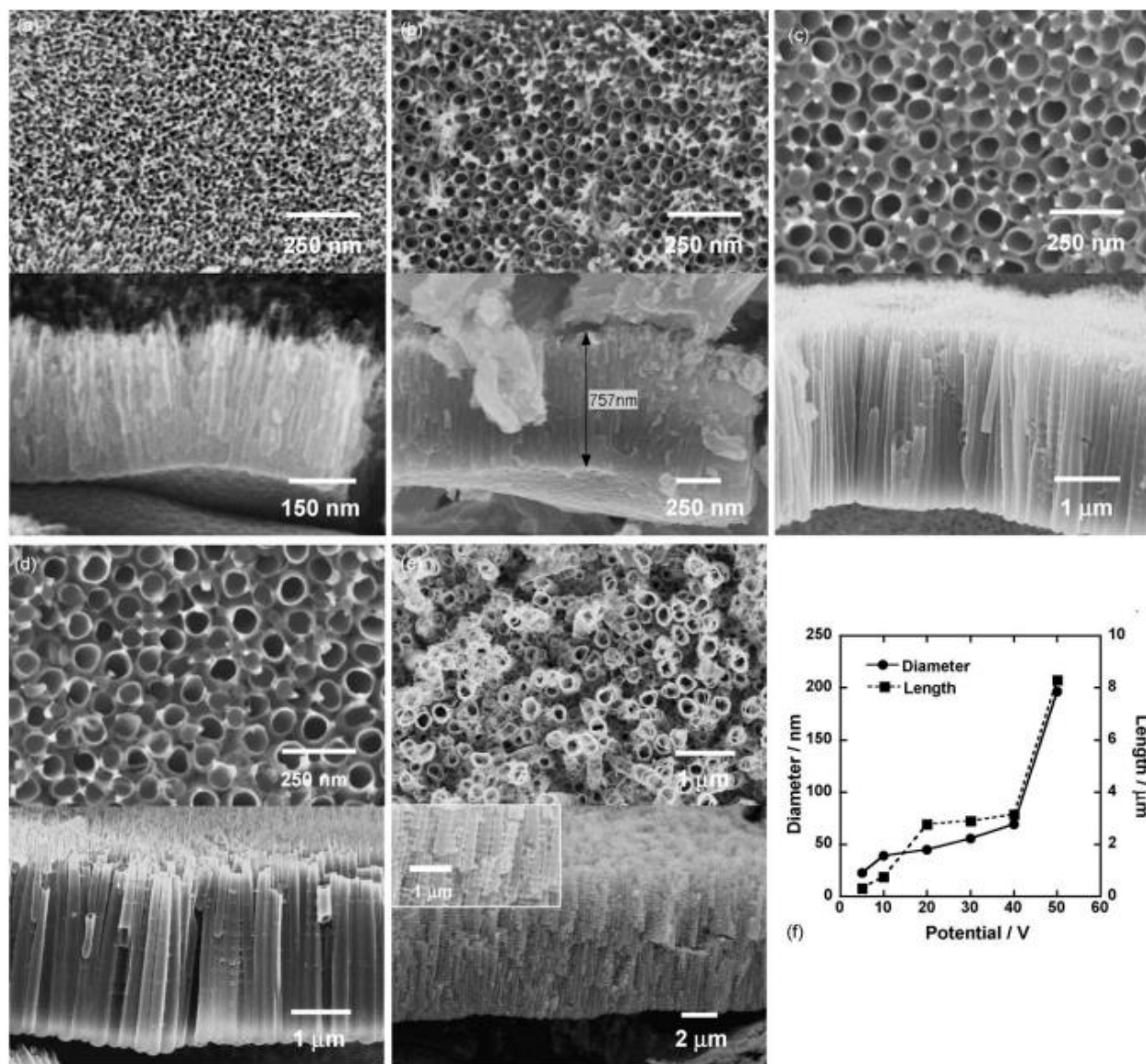
Figure 2.8. SEM images for different NTs anodized for 12,000 s at various potential: (a) 5 V; (b) 10 V; (c) 30 V; (d) 40 V; (e) 50 V, and (f) graph for effect of potential on the obtained diameter and thickness [46].

Deyab et al. [49] reported in their study that increasing the **anodization time** results in increasing the conductivity of the electrolyte because a higher concentration of ions is leached from the anodized substrate to the electrolyte. This increase in the electrolyte conductivity allow the anodization process to benefit from a larger proportion of the applied voltage, which in turn cause the length and the diameter of the formed NTs to increase and the wall thickness to decrease [49]. Whereas, increasing the anodization time of Ti-0.3Mo-0.8Ni alloy in formamide-ethylene glycol based electrolyte to 18 h resulted in a tube length of 4 μm, tubes diameter about 116 nm and tube

wall thickness of 17.5 nm at anodization voltage (20 V), see Figure 2.9 [49]. In the same manner, Lopez et al. [56] showed that increasing the anodization time transform the produced structure from nanoporous to a well-defined NTs [56]. Their study showed that anodizing Ti35Nb5Zr alloy at 20 V in (1 M H_2SO_4 + 34.5 mM HF) electrolyte for only 5 minutes resulted in the formation of nanoporous structures with pore diameter of 25 nm and average tube length about 71 nm, as shown in Figure 2.10a and Figure 2.10b [56]. On the other hand, increasing the anodization time to 60 minutes resulted in the formation of NTs with diameter between 75-100 nm and average length of 900 ± 100 nm, as shown in Figure 2.10c,d [56].
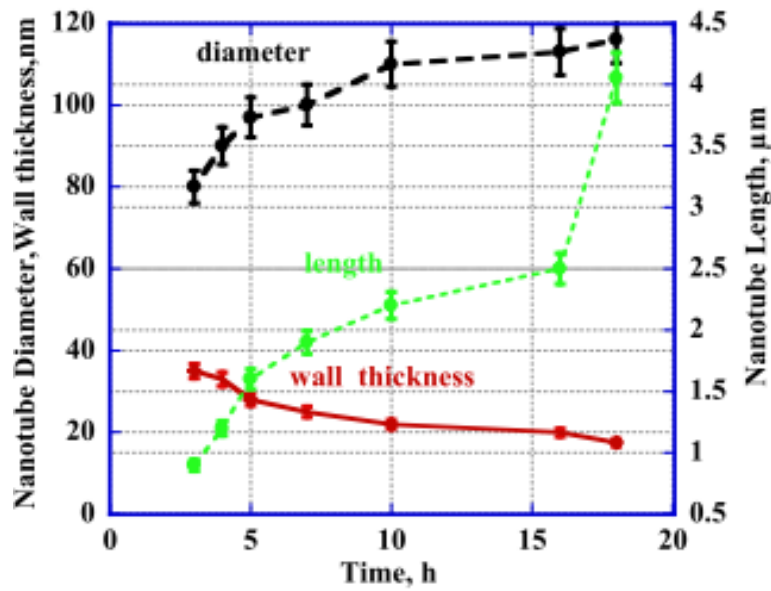
Figure 2.9. Dependence of NT length, diameter, and thickness on the anodization time of Ti-0.3Mo-0.8Ni formed at 20 V in electrolyte of 50% FA and 50% EG with 0.2 M NH_4F and 3% H_2O [49].
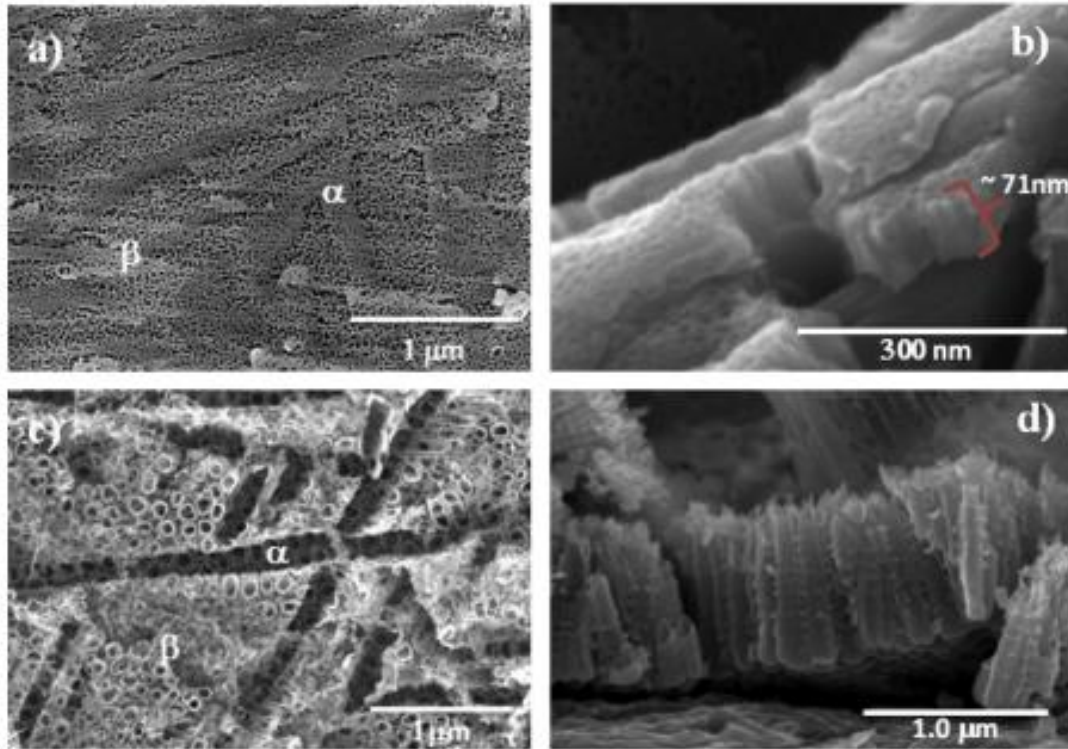
Figure 2.10. SEM image of the anodic layers formed at (a,b) 5 min, and (c,d) 60 min; giving nanoporous (NP), and nanotubes (NT) with their corresponding cross-section [56].

In agreement with Deyab et al. [49] and Lopez et al. [56], Feng et al. [34] reported that increasing the time of anodization of Ti–Zr–Nb alloy in (1 M $(NH_4)_2$ SO_4 + 0.25 M NH_4F) solution increases the NTs diameter and length [34]. At anodization time (5 min) a NTs with two diameters were formed (98 nm and 159 nm) as shown in Figure 2.11a, however, increasing the anodization time to (240 min) increased the larger tubes diameter from 159 nm to 175, while the small tubes diameter was not changed, as shown in Figure 2.11b and Figure 2.11c [34]. However, the ratio of the large tubes to that small tubes increased with the anodization time as shown in Figure 2.11d which shows that the Ratio of Density (small tubes number / large tubes number) had significantly decreased with increasing the anodization time. On the other hand, the length on NTs increased from 2.5 μm to 22 μm upon increasing the anodization time from 5 min to 480 min [34].
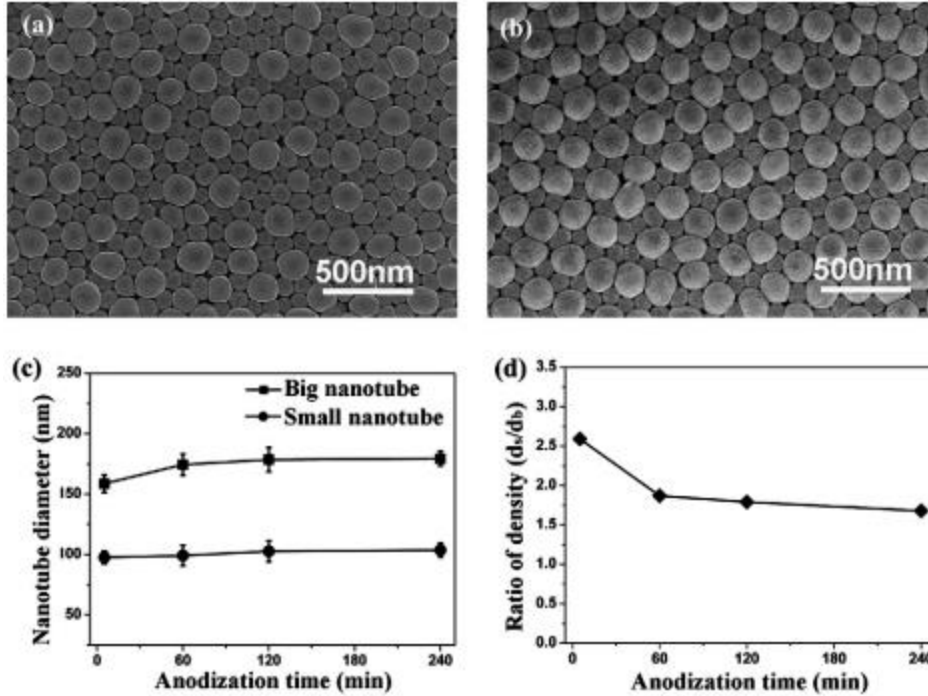
Figure 2.11. SEM top and bottom images (a,b) of two-size-scale NT anodized for 5 and 240 min, respectively. (c) Effect of anodization time on the large and small nanotubes diameter and ratio of density (smaller diameter/larger diameter), respectively [34].

Along the same line, Tsuchiya et al. [46] studied the effect of varying the time of anodization Ti–29Nb–13Ta–4.6Zr alloy in $(NH_4)_2SO_4$ electrolyte at constant voltage (20 V). Figures 2.12-2.14 show the scanning electron microscope (SEM) images of the prepared layers by anodization at 0 s, 1200 s, 4000 s and 12000 s [46]. Whereas at 0 s a top layer of nanoporous structure was formed and an underneath nanotubular layer, as shown in Figure 2.12a. Similarly, at 1200 s (Figure 2.12b) a bottom layer of NTs with a nanoporous layer above it were formed, however, the thickness of the NTs layer (approximately 750 nm) was significantly greater than that at 0 s. At 4000 s, the top nanoporous layer disappeared and only the NTs layer appeared, wherein the NTs showed a bimodal size distribution with two distinct diameters (30 nm and 50 nm) as shown in the top SEM image in Figure 2.12c [46]. However, the bottom SEM images showed a diameters sizes of tubes (50 nm and 100 nm), as shown in Figure 2.14c. This increase in the bottom NTs diameter in comparison with the top NTs diameter clearly indicates that the diameter of the NTs increases with increasing the anodization time [46]. Figure 2.12d, shows that the NTs diameter was significantly increased at anodization time (12000 s) in comparison with that at anodization time (4000 s),

26

moreover the length of the NTs was increased from 1.6 μm to 2.8 μm when increasing the anodization time from (4000 s) to (12000 s) [46].
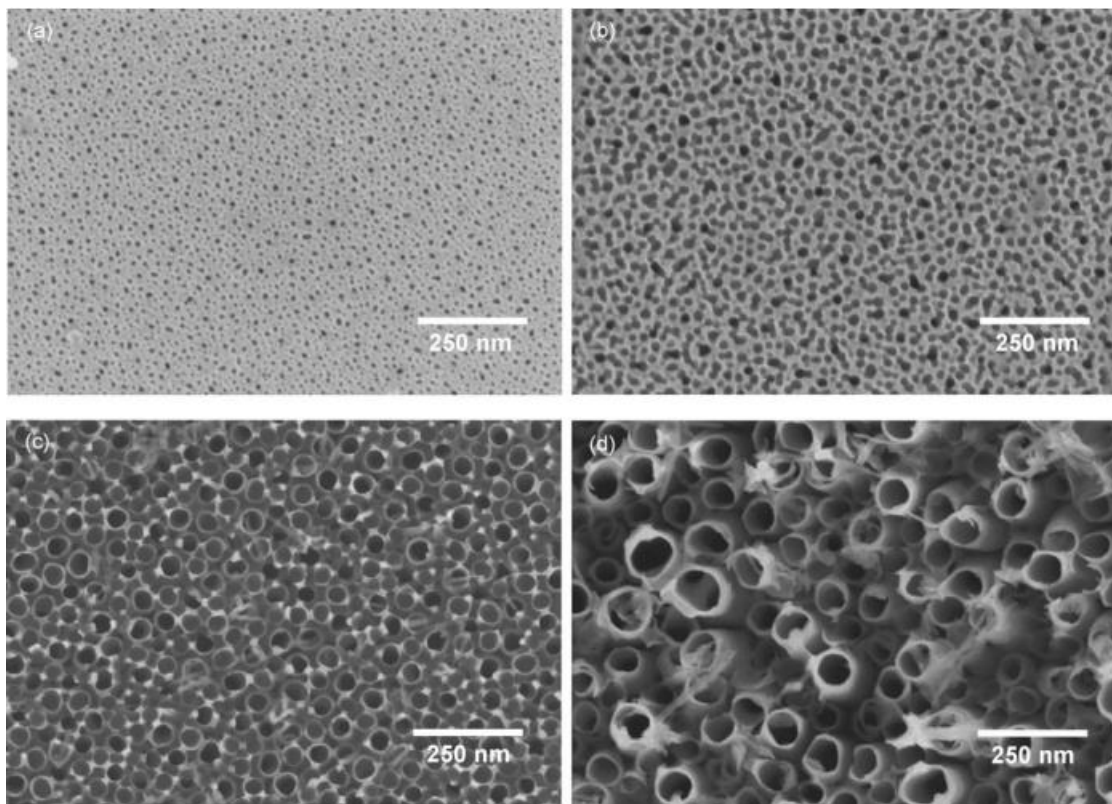
Figure 2.12. SEM top images for nanotubes anodized at 20 V and (a) 0 s; (b) 1200 s; (c) 4000 s; (d) 12,000 s after potential sweep [46].
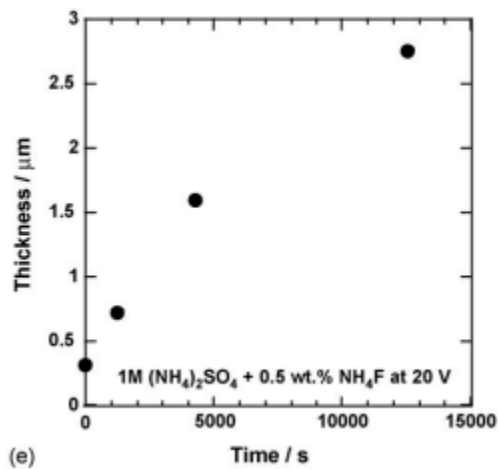
Figure 2.13. Effect of time on the thickness of the nanotube layers [46].
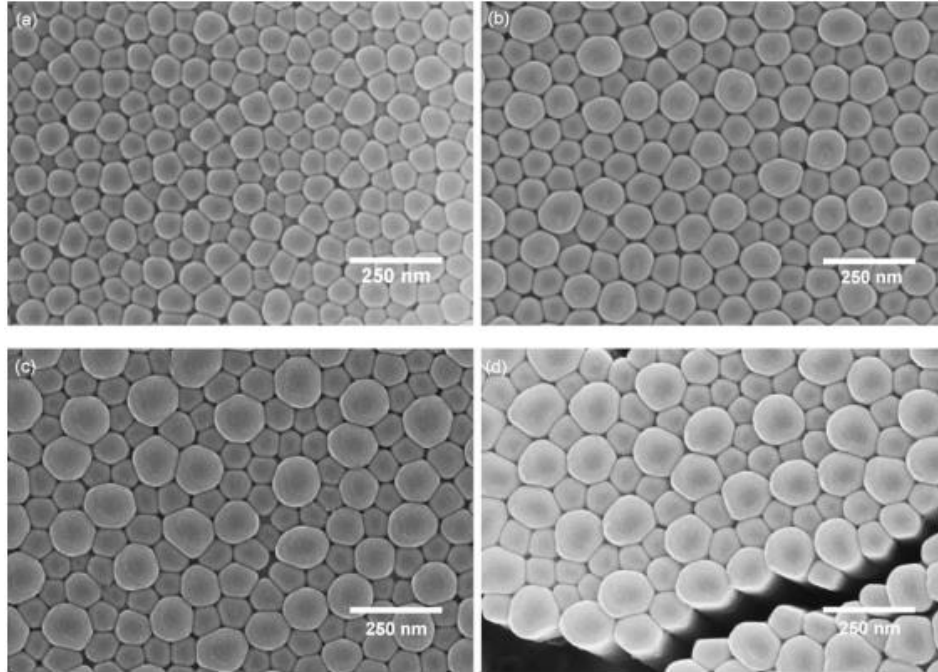
Figure 2.14. SEM bottom images for nanotubes anodized at 20 V and (a) 0 s; (b) 1200 s; (c) 4000 s; (d) 12,000 s after potential sweep [46].

When studying the effect of varying both the anodization voltage and time, Saji et al. [57] showed that a highly ordered NTs is formed when increasing the anodization voltage as well as the anodization time of Ti-35Nb-5Ta-7Zr alloy in a 1M H_3PO_4 electrolyte with 0.5 wt % NaF. Whereas, at anodization voltage (15 V) and anodization time (90 min) a nanoporous structures were formed, while at anodization voltage (20 V) and anodization time (180 min) a well aligned nanotubular structures were formed as shown in Figure 2.15 and 2.16 [57].
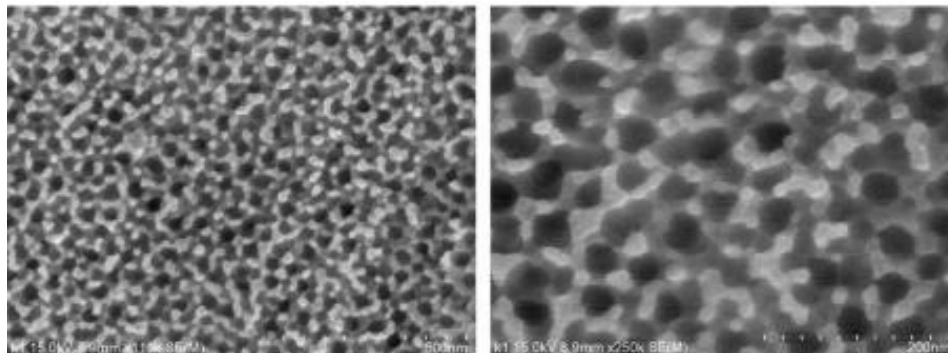
Figure 2.15. SEM images of the surface oxide layer formed at 15 V and 90 min giving nanoporous structure [57].

28
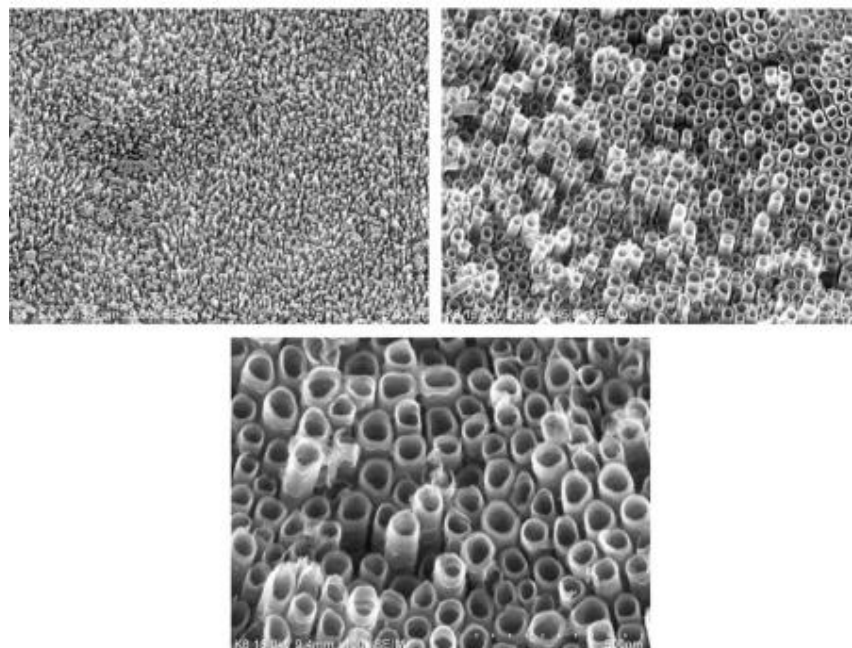
Figure 2.16. SEM images of the surface oxide layer formed at 20 V and 180 min giving nanotubular structure [57].

From all the above, it can be seen that electrochemical anodization techniques in different F⁻ containing electrolyte were used to produce different nanostructures ranging from nanoporous to highly ordered nanotubes in an economic and efficient way. Nanostrucutres were achieved either for single material such as Ti [35,37], Nb [58], Ta [59], and Zr [60]; or binary, ternary, and quaternary alloys with Ti as the base element in the substrate such as TiZr [43], TiNb [33], Ti-30Ta-XZr [61], Ti-6Al-7Nb [62], and Ti–29Nb–13Ta–4Zr [46].

2.2. PEC Electrode Material:

2.2.1. TiO₂ Nanotubes and its Drawbacks:

TiO₂ NTs have many potential applications in different fields of solar energy conversion, catalysis and sensors as a result of their photoelectrochemical and semiconducting characteristics [63,64]. TiO₂ forms three crystal structures upon crystallization, anatase, rutile, and the less stable phase brookite. Although anatase has indirectly slightly larger band gap than rutile (3.2 compared to 3.0 eV), it has faster electron mobility than rutile (4 compared to 0.1 $cm^2V^{-1}s^{-1}$). This is why it is favorable for photoelectrochemical applications [65]. The use of titanium dioxide (TiO₂) as inorganic semiconductor photocatalyst has been very promising and is now converting from an emerging technology into maturing and commercial technology. It has been extensively studied

for the past four decades since Honda and Fujishima first discovered the use of TiO_2 for water electrolysis when subjected to irradiation [18]. It has many advantages including elevated photocatalytic activity, indirect band gap, chemical and photo-corrosion resistance, abundance, low price, and non-toxicity [66,67]. However, there are some drawbacks of TiO_2, wide band gap (3.2 eV for anatase and 3 for rutile). This means absorption in the ultraviolet region only, while for photocatalytic reactions utilizing sun light, it is desirable to extend the absorption to visible region in order to make use of most of the solar spectrum (UV account for less than 5% of the solar radiation). Additionally, TiO_2 has d-shells which are partially filled and influence charge carriers' low mobility, thus the photo-generated electron hole pair within TiO_2 suffers fast rate of recombination as well as slow hot charge carrier diffusion which lowers the performance efficiency of TiO_2 as photocatalytic material [16,66]. These drawbacks limit the use of TiO_2 in economical practical applications.

2.2.2. TiO_2 Modification Approaches:

To overcome TiO_2 deficiencies, several approaches have been carried out in terms of bulk, surface, and the environment [68]. The approaches are in three main aspects in terms of photocatalysis; (1) generation of electron-hole pair, (2) separation and transfer of charge carriers (electron and hole), and (3) surface engineering [64]. Considering the first aspect, efforts were done to narrow down the band gap, and hence enlarge the portion of the solar spectrum over which electros will be excited. This might be achieved through addition of new material or crystal structure adjustment. As for the second aspect, to enhance charge carrier separation and transfer, passivating harmful trap sites at the surface, growing heterojunctions, allowing unidirectional passageway for the carriers while at the same time shorten lateral distance. While the third aspect is engineer the surface in order to produce certain facets at the reaction surface where reactant adsorption and product desorption would occur. Optimizing both quantity and quality of the crystal surface of the semiconductor would affect the resulting performance [64]. Among different approaches, we will explore the efforts done in some areas for the sake of enhancing charge separation and transfer, in addition to decreasing the recombination sites and defects. These include: doping and alloying, morphology optimization, and defect engineering.

2.2.2.1. Doping and Alloying:

However, some of TiO$_2$ NTs drawbacks are not overcome yet despite the enormous efforts carried out to resolve them. In this regard, considerable attention has been drawn to enhance TiO$_2$ NTs photocatalytic efficiencies via several techniques among which is impurity doping [69], whether anion using N, F, P, C or S to replace the oxygen in the lattice or cation by substituting Ti cations with Mn, Nb, V, Fe, Ni, and Cr atoms. Other techniques involve the use of perovskites and binary oxides [70,71]. The latter is very promising since it somehow avoids some of the problems associated with doping for the sake of enhancing charge carrier mobility, such as the formation of recombination sites and deep localized band gap states that causes the excited electron-hole pair separation to be less efficient. Although doping is a widely-investigated technique, it encounters the problems of non-homogenous distribution. Also, nanoparticles decoration for TiO$_2$ nanotubes could be considered another approach. Yet it suffers serious problems such as nanoparticle size variation, nanoparticles aggregation, non-uniform distribution on the surface and walls of the nanotubes, and possible lack of cleanness. Although bad distribution could be overcome through the use of some molecules as linker to attach both nanoparticles with nanotube, this would further cause more recombination problems of the charge carriers [72]. Another technique for doping as well is ion implantation, however, it possesses some limitations such as the relative high cost and special equipment needed to carry out the doping besides the high possibility of damaging the nanotubes. Likewise, cation doping achieved by immersing the nanotube structure into a solution containing the metal cation followed by thermal annealing to form nanoparticles of separate oxide phase does not happen without problems of being detached [70].

Alloying, on the other side, which is the use of an alloy as a substrate for nanotubes anodization, might aid in the homogenous distribution of an element being inserted into the unit cell, hence creating nanotubes with one of two, mixed oxides or doped TiO$_2$. Nanoporous and nanotubular strucutres of oxide layers have been anodically grown on the surface of TiNb, TiW, TiTa, TiZr, TiAl, TiCu, and TiMo alloys [70]. Nevertheless, it is difficult to obtain uniform nanotubes grown on bi-phase Ti-alloy substrate [62,72,73]. Others fabricated NTs on the surface of single-phase alloy or solid solution such as Ti50Zr, Ti28Zr8Nb, Ti29Nb13Ta4.6Zr and Ti35Nb, respectively [34,43,44,54,73]. An interesting and extensively studied option is Nb insertion [74-78]. Nb presence overcomes another drawback of TiO$_2$ which is the microstructure destruction with increasing annealing temperature as a result of rutile formation, which is also known for its weak

carrier transport properties. On one side, it increases the conductivity. On the other side, Nb was found to stabilize anatase and hinders its phase transformation to higher temperatures providing thermal stability [76-78]. Schumki et al. [79] proved that NTs having Nb exhibited higher photocurrent compared to TiO_2 NTs due to higher electron mobility, which indicated lower recombination rate with the surface trapped holes. Mei et al. [62] studied the effect of Nb doping on the photoelectrochemical behavior and found conductivity enhancement due to replacing Ti^{4+} with Nb^{5+} and hence shifting Fermi level towards the conduction band. Thus, recombination would be lower due to better charge collection as a result of enhanced electron mobility. Similar findings were reported by Xu et al. [73] where they mentioned the significance of adding Nb to Ti to enhance the conductivity and decrease the charge transfer resistance which in turn will improve the electrode activity due to higher transfer rate of electrons. However, this behavior varied with the amount of Nb doping and the method of preparation which lead to inconsistent results [62]. Schmuki et al. [79] also presented that adding Nb in different content affected the conductivity when the nanotubes were annealed at 650 ºC. Nb doping and alloying have been studied by different researchers for its enhanced photocatalytic activity. However, contradicted results and performance variations were obtained [47,67,80]. Hence, it is of great importance to develop good understanding of the chemical and physical properties of the formed oxides microstructure and its correlation with photoelectrochemical response. Once this correlation is found, tailored repeatable and reliable performance will be achieved. Yet, it is quite hard to deduce the point defects introduced into the structure and directly relate them to the optical and photoelectrochemical behavior. Furthermore, controlled fabrication of nanotubes with desired dimensions is of great importance too since it will impact the microstructure, charge carriers transfer mechanism, optical and electrical properties.

2.2.2.2. NTs Morphology Optimization:

Along with passivating defects to improve the charge carriers' dynamics through doping and alloying, many studies have reported the influence of nanostructure dimensions on the material functionality. Accordingly, it is essential to optimize the material properties in order to enhance the charge carriers' transfer and collection. As stated earlier in section (2.1.2.3) that optimum morphology is required to enhance catalytic performance in terms of absorption and charge carrier transfer through the photoelectrode. In this regard, many attempts were carried out to control the nanotubes morphology and dimensions in terms of tubes length and diameter. It was found that it

enormously affected the performance for solar energy conversion positively. Having tubes with a diameter large enough to collect most of the solar spectrum and at the same time, thin walled nanotubes will fasten the charge carrier mobility and reduce recombination. It is worth mentioning that wall thickness of nanotubes is a determinant factor playing crucial role in the charge carrier dynamics and hence the photo-electrochemical behavior [81-84]. Although most published work deal with nanotubes with wall thickness larger than diffusion length, Amer et al. [85] and Mohamed et al. [86] reported the fabrication of ultrathin wall nanotubes of ZrO_2 and TiO_2, respectively. In the study of ultrathin wall TiO_2 nanotubes, the great improvement in the photocurrent (almost the double compared to thick-walled nanotubes) was attributed to the photogenerated holes easily diffusing through the thin walled nanotubes to the interface between the semiconductor and electrolyte, and thus better charge separation [86].

2.2.2.3. Defect Engineering:

In addition to ions incorporation and morphology optimization of TiO_2 nanotubes photoelectrode, which have been extensively studied to improve semiconducting properties, defect disorder was reported to affect TiO_2 properties as well as composition and structure. Consequently, defect engineering is to be the at most solution to improve the solar energy conversion performance. Second generation of modified TiO_2 NTs is the goal through defect engineering to create in-situ defects [87]. Structural defects exist in all materials due to thermal processing and processing kinetics and greatly influence the materials properties [88]. In that sense, thermal annealing is used to reduce the number of structural defects and promote material crystallinity. Generally, during thermal annealing, the structural defects and dislocations transfer to the surface where adsorption/decomposition would occur and subsequently material would change its stoichiometric ratio and structure [89]. Such crystallinity and symmetry plays essential role in the optical and electronic properties of semiconductor material. The structure of the electronic band is dependent on the crystalline lattice. Therefore, any defects in crystalline structure would affect the structure of the electronic band. In crystalline lattice, atoms are arranged and the accompanied electrons orbitals overlap and their energies form states. For this reason, it is important to study defects and correlate their existence to the corresponding electronic properties [90]. For instance, the improvement of silicon industry the past 50 years, which mainly depended on tailoring its defects to adjust transport characteristics [88]. The crystal defects including point defects such as Ti^{3+} or oxygen vacancy (V_O) in the crystal lattice of TiO_2 was found to influence the functional properties of TiO_2 namely

33

the charge transfer, electronic band structure, and the catalytic performance, therefore, it is favorable to overcome the drawbacks of TiO_2. Introducing V_O into the lattice would create a band below TiO_2 conduction bad and hence contribute to better charge separation at the metal oxide/electrolyte interface as it acts as shallow donors [66]. Moreover, Marchiori et al. [91] proposed two point defects associated with charge compensation for the addition of Nb^{5+} into TiO_2, valence induction to introduce Ti^{3+} or Ti^+ vacancy creation per each four Nb. Khan et al. [67] used density functional theory (DFT) along with experimental work to study the point defects introduced into Nb-doped TiO_2 compared to pure TiO_2 anatase and their effect on the optical transitions and photocatalytic activities. They found that O_2 annealed Nb-doped TiO_2 had the highest photocatalytic activities compared to N_2 or air annealed samples. While for the pure anatase TiO_2, O_2 annealed samples had the least value for the photocatalytic activity [67].

Chapter III

Objectives and Scope of Work

3. Chapter III: Objectives and Scope of Work:

The objective of this study is to enhance the efficiency of Ti-based photoanodes for solar water splitting through incorporating Niobium (Nb) as an alloying element to the base substrate upon which mixed oxide of vertically oriented, highly ordered, and ultrathin smooth nanotubes will be grown. Among many elements, Nb was found to increase conductivity when mixed with Ti in addition to enhancing photogenerated charge carrier (electrons) mobility, allowing better charge collection along with lower recombination as Nb can act as blocking layer restraining the recombination process. Moreover, Nb was reported to shift anatase-to-rutile transformation to higher temperatures. In addition, controlling and adjusting the obtained morphology as well as adding Nb are expected to enhance charge carrier dynamics and boost efficiency of the photoanodes. The successful fabrication of NTs on Ti-45Nb alloy with certain required dimensions and investigation of the evolving NTs structure to correlate the geometry, phases, and induced defects within the microstructure with the photoelectrochemical behavior was achieved through the activities shown in Figure 3.1.

Figure 3.1 describes the flow and work strategy of the present study. First, broad and intensive literature survey was done to get familiar with various photoanodes prepared of TiO_2 and/or TiO_2-xx nanomaterials prepared in different nanostructures for hydrogen production via solar water splitting shedding light on some of the efforts to overcome the problems of TiO_2 nanotube arrays. It shows how photocatalytic performance is greatly affected by several factors such as topography, morphology, internal structure, and composition of the semiconductor for the photoelectrode. Then a description of the materials and experimental procedures followed to fabricate and characterize photoanodes of the current study is given. Nanotubes were grown on Ti-Nb alloy via electrochemical anodization and their corresponding photocatalytic behavior was investigated and compared with those grown on an ordinary Ti substrate. After preparing and optimizing the nanotubes dimensions for the required geometrical structure, the as formed tubes were annealed at different temperatures in air, then characterized with respect to their morphological, structural, and photoelectrochemical properties. Results were then reported with data analysis and interpretation. The results were compared to pure TiO_2 NTs as reference material since it is often hard to compare with results from literature due to different preparation conditions. Accordingly, the photocatalytic performance enhancement was reported versus TiO_2 NTs prepared in the same electrolyte

conditions. Furthermore, experimental results were correlated with the chemistry of point defects present in the structure where Nb insertion into the TiO_2 phases occurred.

Objective

Enhance the efficiency of TiO$_2$ based photoanodes by incorporation another element such as **Nb** and develop a correlation between the obtained structure and the resulting photocatalytic behaviour.

Literature Survey

- Electrode structure and its preparatioon technique
- Electrode materials previously studied and their drawbacks
- Some approaches to enhance the efficiency of the photoanodes

Experimental Work

- Photoanodes Preparation
  - Substrate Anodization
  - Subsequent thermal Annealing
- Photoanodes Morphological and Compositional Characterization
  - Optical Microscope
  - Scanning Electron Microscope (SEM)
  - X-ray Photoelectron Spectroscopy (XPS)
- Photoanodes Structural Characterization
  - Raman
  - X-ray Diffraction (XRD)
- Photoanodes Optical and Photoelectrochemical Characterization
  - UV-Vis
  - Photoelectrochemical Measurements

Results and Discussion

- Result analysis and interpretation
- Comparison with previous findings
- Correlation between morphological, structural defects and photocatalytic characteristics

Conclusion and Future Work

- Conclude the findings of the study
- Make a future recommendations based on interpreted results

Figure 3.1. Thesis Objective and Work Flow Chart

Chapter IV

Experimental Work

4. Chapter IV: Experimental Work

4.1. Materials:

Nanotube arrays comprising the photoanodes were grown on Titanium-45 Niobium Grade 36 (Ti-Nb) sheets were purchased from Tico Titanium, Inc. and Titanium metal foil with purity of 99.95% purchased from Alfa Aesar. Chemicals used in the preparation process were brought from Sigma Aldrich. Hydrogen gas used in thermal annealing if the obtained nanotubes was supplied by Airgas Company.

4.2. Methods of Nanotubes Formation:

4.2.1. Sheet Preparation:

Ti and Ti-Nb alloy sheets were cut into plates of 2×1 cm^2. As for Ti-Nb sheets, mechanical grinding and polishing was applied before cleaning. The sheets were mechanically grinded with Silicon Carbide papers of coarse grit followed by finer grits under running water. SiC papers employed were of 600, 800, 1000, and 1200 grits respectively. In order to get even smoother surface of lower crystal structure deformation, the sheets were then polished with Alumina suspension and piece of cloth on a disc to eliminate the damage caused by the grinding process. Finally, the sample were placed under running water to remove the Alumina residuals of the specimen surface.

4.2.2. Potentiostatic Anodization:

First, Ti-Nb sheet as well as Ti foil was ultrasonically cleaned by immersion in acetone, ethanol, and distilled water for 15 minutes, respectively. The sonicator was set at 25% of its maximum amplitude. Then potentiostatic anodization was carried out using two electrode electrochemical cell in order to form the nanotube arrays on Ti-45Nb and Ti substrates. The substrates (Ti-45Nb and Ti) were connected to the positive pole of the Agilent E3612A DC power supply (working electrode) while a platinum foil (counter electrode) was connected to the negative pole of the electrochemical cell. Three electrolytes were used in the optimization of nanotubes morphology and dimensions, two ethylene glycol-based and one aqueous-based containing different amounts of fluoride. Electrolyte A: 0.3 M NaF + (C$_2$H$_6$O$_2$ + Water 50/50), Electrolyte B (Aqueous): 1 M (NH$_4$)$_2$SO$_4$ + 0.25 M NH$_4$F, and Electrolyte C (Organic): 25 ml C$_2$H$_6$O$_2$+ 25 ml H$_2$O + 0.5 gm NH$_4$F.Voltage was applied with ramp of 0.1 V /sec. and kept at 40 V. for various time intervals.

The anodization was carried out at room temperature of approximately 23 °C. The obtained samples were rinsed in acetone and distilled water after anodization and then left to dry in air.

4.2.3. Thermal Annealing:

The as-formed amorphous nanotube arrays were thermally annealed using LINDBERG/Blue M TF55030C tube furnace. The samples were placed in a quartz tube inside the tube furnace and heated to different temperatures 350, 450, 550, and 650 ℃ at an upward ramp of heating rate 5 ℃/min for 2 hours in air.

Figure 4.1 shows a flow chart for the preparation procedure of the photoanodes.
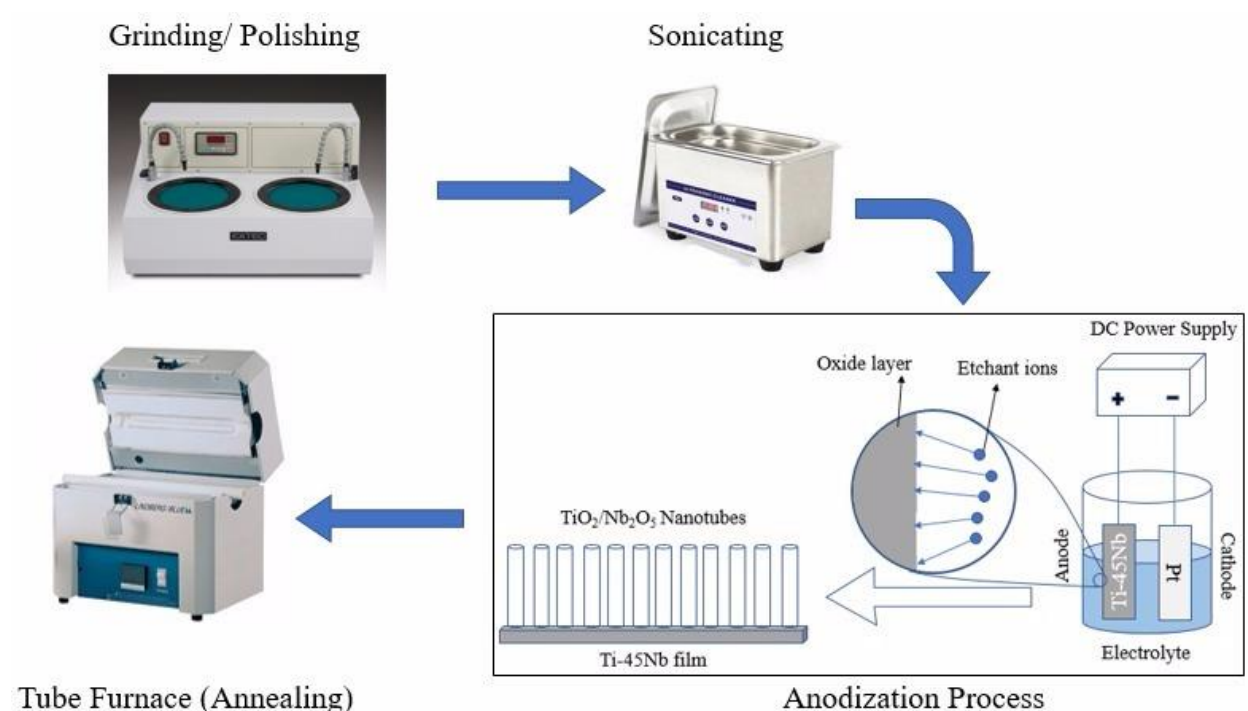
Figure 4.1. Flow chart of the preparation procedure of photoanodes.

4.3. Methods of Nanotubes Characterization:

4.3.1. Morphological and Compositional Characterization:

In order to tailor the surface oxide properties, good understanding of the chemical and physical properties of this surface is crucial to be able to control these interactions effectively.

4.3.1.1. Optical Microscope:

The as received substrates were grinded and polished in order to investigate the microstructure of the alloy using optical microscope.

4.3.1.2. Field Emission Scanning Electron Microscope (FESEM):

The surface morphology of nanotubes produced at different conditions were examined using was investigated using field emission scanning electron microscope FESEM-Zeiss SEM Ultra 60. The average nanotubes length, diameter and wall thickness as well as the standard deviation were calculated from three different FESEM images of five different locations on the sample surface.

4.3.1.3. Energy Dispersive X-ray Spectroscopy (EDX):

Elemental composition in addition to the distribution were determined by Energy Dispersive X-ray spectroscopy (EDS; Oxford ISIS 310, England) at an accelerating voltage of 22 kV, working distance 9.5 mm, and aperture of 60 µm for the EDX detector.

4.3.1.4. X-ray Photoelectron Spectroscopy (XPS):

Composition determination of alloyed samples is difficult. Accordingly, the chemical state and the surface composition analysis of the samples were investigated using Thermo-Scientific K-Alpha X-ray photoelectron spectroscopy (XPS) with an Aluminum anode. The operating mode was Constant Analyzer Energy (CAE 50). Background was subtracted from Ti2P, O1s, S2p, and Nb3d core level spectra and fitted using Gaussian-Lorentzian peaks in order to find the components peak. O1s carried out at 532 eV was taken as charge reference for the spectra. It is worth mentioning that XPS analysis is confined to the surface layer and does not provide information concerning the bulk composition of the samples.

4.3.2. Structural Characterization:

4.3.2.1. Raman:

Phase composition as well as samples crystallinity and vibrational properties were characterized using Raman spectroscopy. Raman-scattering is favorable to analyze the presence of oxides which cannot be detected by other methods due to sensitivity of its signals to crystal structure and defects.

Raman spectra of both Ti and Ti-Nb nanotube arrays annealed at different temperatures and atmospheres were recorded at room temperature using Raman Spectroscopy (ProRaman-L Analyzer). Laser Beam of 532 nm wavelength was used for the excitation as a source of monochromatic light. Scans were performed on a range (100 -1000 cm^{-1}) with exposure time of 20 sec. in order to allow the recognition of different phases present in the samples.

4.3.2.2. X-ray Diffraction (XRD):

In order to identify and detect crystalline phases present in the structure of as-formed and thermally annealed nanotubes grown on Ti and Ti-Nb substrates, X-ray diffraction pattern was recorded on PANalytical X'Pert PRO XRD diffractometer using monochromatic Cu-Kα radiation (λ=0.1548 nm) at 40 kV and 40 mA. The samples were scanned from 10º to 90º with a step size of 0.02 º2Th.

4.3.3. Optical and Photo-Electrochemical Characterization:

4.3.3.1. Ultra Violet – Visible (UV-Vis):

The optical properties of both Ti and Ti-Nb nanotube arrays were evaluated using UV-Vis spectrophotometer with an integrating sphere and reflectance attachments consisting of solid-sample holder for the reflectance measurements. Diffuse reflectance spectra were recorded over a wavelength range of 200 – 900 nm and then transformed mathematically using Kubelka−Munk function, $F(R) = (1−R)^2/2R$. Tauc plots were created using this function and the band gaps were determined from the absorption spectrum onset.

4.3.3.2. Photoelectrochemical Measurements:

Evaluation of photocatalytic water splitting performance was studied for the photoelectrode trough two tests. First, Current-Voltage (I-V) measurements were recorded applying linear sweep voltammograms mode with a scanning potentiostat (CH Instruments, model CHI Model 600B Series) Electrochemical Workstation which was used to plot dark and illuminated currents at a scan rate of 10 mV/s for applied bias from -1 to 1 V versus Saturated Calomel Electrode (SCE) acting as the reference electrode. Photoelectrochemical measurements were conducted in a standard three-electrode cell configuration utilizing 1 M KOH solution to increase the conductivity of the water (Figure 4.2). The working electrode (WE) comprised of the nanotube arrays grown on the substrate surface of photoanode, which was connected to the cell through attaching copper sheet via conductive silver paste to the metallic contact of the samples, while a platinum foil served as a counter electrode.

The cell with quartz surface was enlightened with a Spectra Physics 300 W Xenon lamp passing by Air Mass 1.5 filter (Oriel) in order to simulate solar light arriving the surface of the earth. The cell position with respect to the light source was set so as to acquire incident light power of 100 mW/cm^2.

Second, photcurrent-time measurements (OR open-circuit potentitial) was carried out at 0.5 V using Amperometric current-time (i-t) curve over period of 200 s.

Under illumination and bias application, holes are generated at the anode in addition to the electron, as a consequence, electrolyte oxidation occurs at the anode while the electrons flow through the wire to the cathode where water molecules are reduced to produce hydrogen.
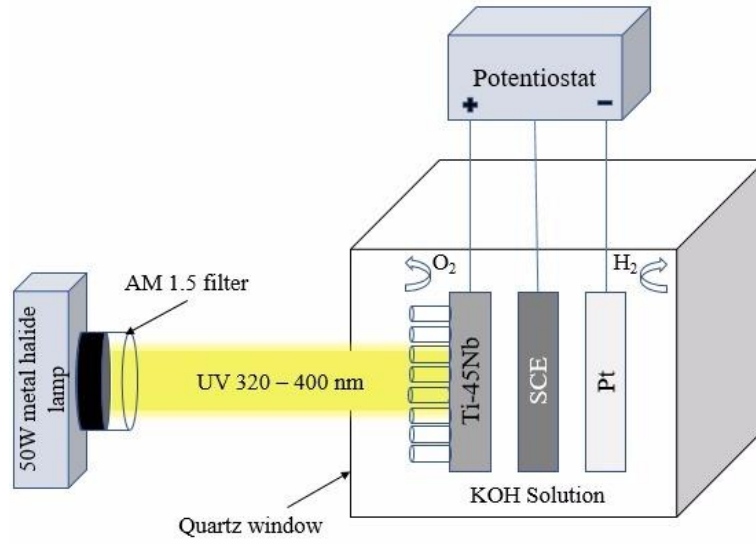
Figure 4.2. Schematic representation of the photoelecrochemical measurements device.

4.3.3.3. Incident Photon-to-Current Conversion Efficiency (IPCE):

For further investigation of the nanotubes quantum efficiency and to better understand the role of defects and their influence on the collection of charge carriers, incident photon-to-current conversion efficiency (IPCE) was measured. The IPCE is a measure of the magnitude of electrons photogenerated and collected per photon irradiated on the photoelectrode surface. The test was taken out in an arrangement of two electrodes with the nanotube being the working photoelectrode and a platinum foil as the counter electrode. The two electrodes were immersed in 1M KOH electrolyte and subjected to irradiation from a 300 W Xenon lamp coupled with monochromator at different wavelength. At each wavelength, the IPCE was calculated in accordance to the following equation (Equation 4.1) [92]:

$$IPCE = (1240 \times I_{PH}) / (\lambda \times P_{light}) \qquad (4.1)$$

Where, I_{PH} is the photocurrent density at certain λ, λ is wavelength of the incident light, P_{light} is the intensity of incident light or in other terms photon flux (mW/cm^2) and 1240 is unit correction factor

exemplifying incident light photon energy. The measurements were recorded utilizing New port QEPVSI-B with no applied bias.

It should be noted that each semiconductor has a critical maximum efficiency that can be reached depending on its band gap and corresponding to whether Xe lamp or AM 1.5 G is used. Figure 4.3 shows such efficiencies.
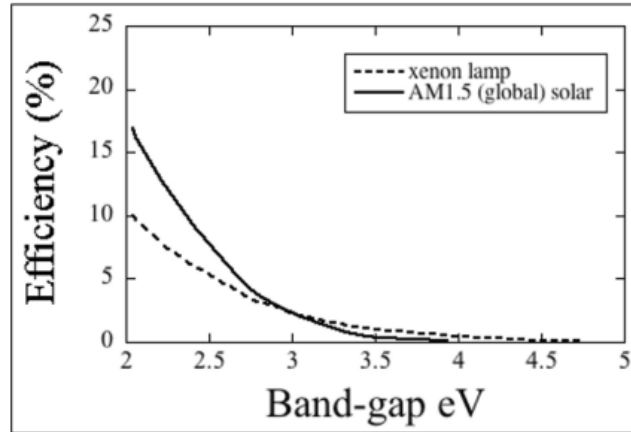
Figure 4.3. Maximum critical efficiency of different semiconductor band gap for both xenon arc lamp and AM 1.5 [92].

Another way to express hydrogen generation efficiency is calculating the output power to the input light power. The power generated within the photoelectrochemical cell to drive the chemical reaction of water splitting divided by the input light irradiance represents the efficiency as in Equation 4.2 [92]:

$$\eta = \frac{I\,(1.23 - V_{bias})}{J_{light} \times A} \times 100\% \tag{4.2}$$

Where I is the photocurrent (mA), 1.23 V is the required potential to cause water-splitting, V_{bias} is the external applied bias (V), J_{light} is the simulated solar light irradiance (mW/cm^2), and A is the irradiated area (m^2). This efficiency expression follows the assumption that all the charges being photogenerated are depleted in the chemical reaction.

Chapter V

Results and Discussion

5. Chapter V: Results and Discussion

5.1. Morphological and Geometrical Characterization:

The as received Ti-45Nb alloy substrate was examined under optical microscope to ensure the formation of solid solution β single phase. The substrate consisted of equiaxed β-grains with an average grain size of 52.85 μm, as illustrated in Figure 5.1a. Nb is a β stabilizer. This step is very important and determinant for developing anodization scheme to be followed in order to obtain uniform sized nanotubes with ultrathin and smooth walls. As stated in the literature review section, substrates of dual phase would be more difficult to grow nanotubes on their surface due to the possibility of dealloying. Figure 5.1b displays such grains above which Nanotubes have been grown.
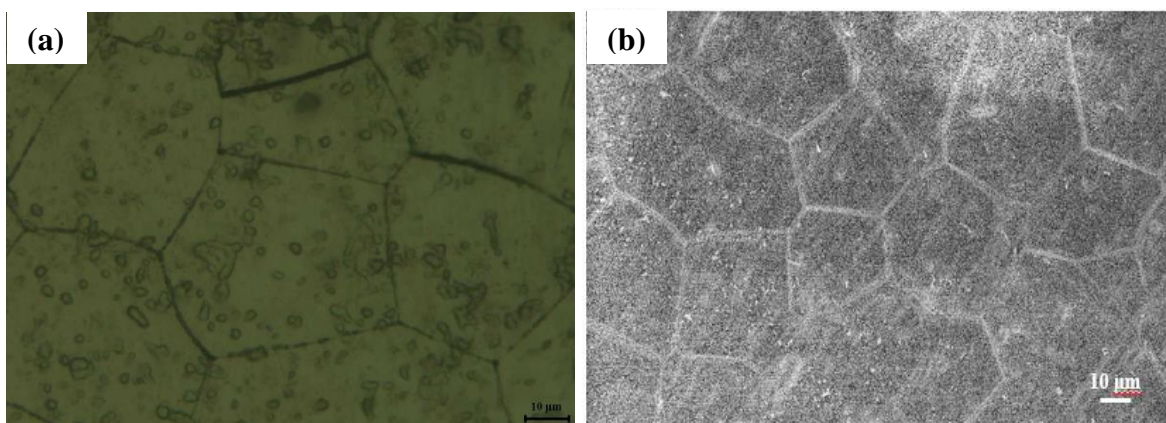
Figure 5.1. (a) Optical image of the Ti-45Nb metal substrate, (b) FESEM image of NTs formed on the Ti-45Nb alloy upon anodization.

It is challenging to grow uniform homogenous NTs on the surface of Ti-45Nb alloy as the diffusion coefficient of the two metals differs. During oxide formation, Ti migrates faster than Nb [52]. First, bimodal size nanostructure was obtained upon using **Electrolyte A,** which was in agreement with what Das et al. [93] reported earlier due to difference in dissolution rate of TiO_2 and Nb_2O_5 in fluoride containing electrolytes as a result of dissimilar geometrical situations. Moreover, obtained nanotubes were of very thick walls as depicted in Figure 5.2. Accordingly, modifications were done to the electrolyte by trying aqueous electrolyte instead of organic counterparts with the addition of ammonium fluoride to the electrolyte that caused an increase in current densities as higher amounts of F⁻ ions lead to higher current densities during anodization due to the greater oxide dissolution rate as a result of formation of water soluble TiF_6^{2-} complex [94]. With

anodization time, reaction temperature increased leading to higher electrolyte dissolution ability. Hence, oxides solubility is decreased upon reducing the electrolyte dissolution ability in order to produce NTs of similar morphologies [50]. NTs reach steady state growth rate when electrochemical etching rate at the bottom equals the chemical dissolution rate at the top [47].
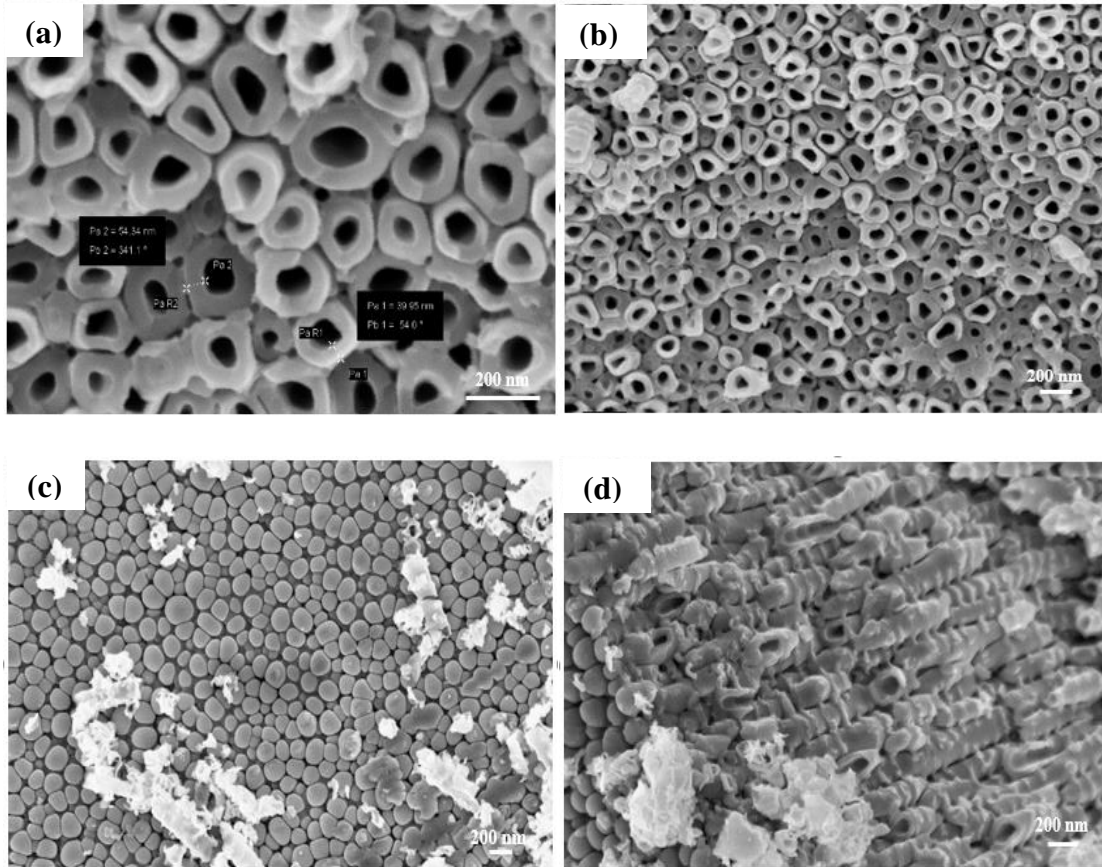
Figure 5.2. FESEM images of (a,b) top surface, (c) bottom, and (d) cross-section of the nanotubes formed in Electrolyte A

In order to fabricate nanotube arrays with the required morphology and dimensions, applied voltage was kept constant at 40 V as while changing the time intervals (10, 20, 30, 40, 50, 60, 120, and 180 min) for anodization carried out in electrolyte B, so as to develop model of nanotube growth onto the surface of an alloy consisting of single phase solid solution. At the beginning of the anodization, oxide layer is formed instantaneously on the surface of the alloy substrate as a result of surface positive ions reacting with negative oxygen ions present in the electrolyte. The oxide layer is formed uniformly across the surface according to the following reactions (Eqs. 5.1 and 5.2):

48

$$2H_2O \rightarrow O_2 + 4e^- + 4H^+ \qquad\qquad (5.1)$$

$$Ti + O_2 \rightarrow TiO_2 \qquad\qquad (5.2)$$
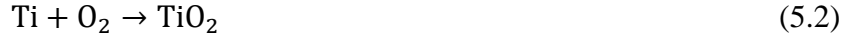
For small time interval anodization, porous structure was observed as seen in Figure 5.3 a due to the localized field-assisted dissolution, which prevailed chemical dissolution since the formed oxide layer was thin and therefore the electric field was relatively large. The small pits served as centers for pore formation and were formed according to Eq. 5.3:

$$TiO_2 + 6F^- + 4H^+ \rightarrow TiF_6^{2-} + 2H_2O \qquad\qquad (5.3)$$
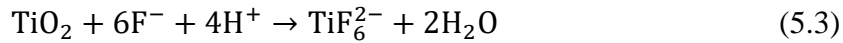
Afterwards, the pits grew into larger pores, increase in density, and then they become distributed uniformly across the whole surface as show in Figure 5.3b,c of the structure obtained after slightly longer anodization times. The pores grew in size as a result of the formation of more dense oxide inward at the bottom of the pore. The positive ions would migrate inward from the metal to the oxide/electrolyte interface and hence get dissolved by the F$^-$ ions. The oxide growth and dissolution rate occurring at the interface of metal/oxide and pore bottom/electrolyte, respectively, reach a point where they become equal. The nanotube length would continue to grow until chemical dissolution rate equals electrochemical etch rate (field-assisted oxidation and field-assisted dissolution). It is worth mentioning that the rate of electrochemical etching is dependent on the applied potential of anodization as well as electrolyte composition, while the rate of chemical dissolution is dependent on the F$^-$ ions concentration within the electrolyte in addition to the electrolyte pH [45]. Figure 5.3d shows top FESEM image of the nanotubes anodized for sufficient period. The smallest obtained wall thickness was 8 nm for NTs prepared for 120 min as presented in Figure 5.4, which is the smallest reported so far and smaller than the hole diffusion length in TiO$_2$.
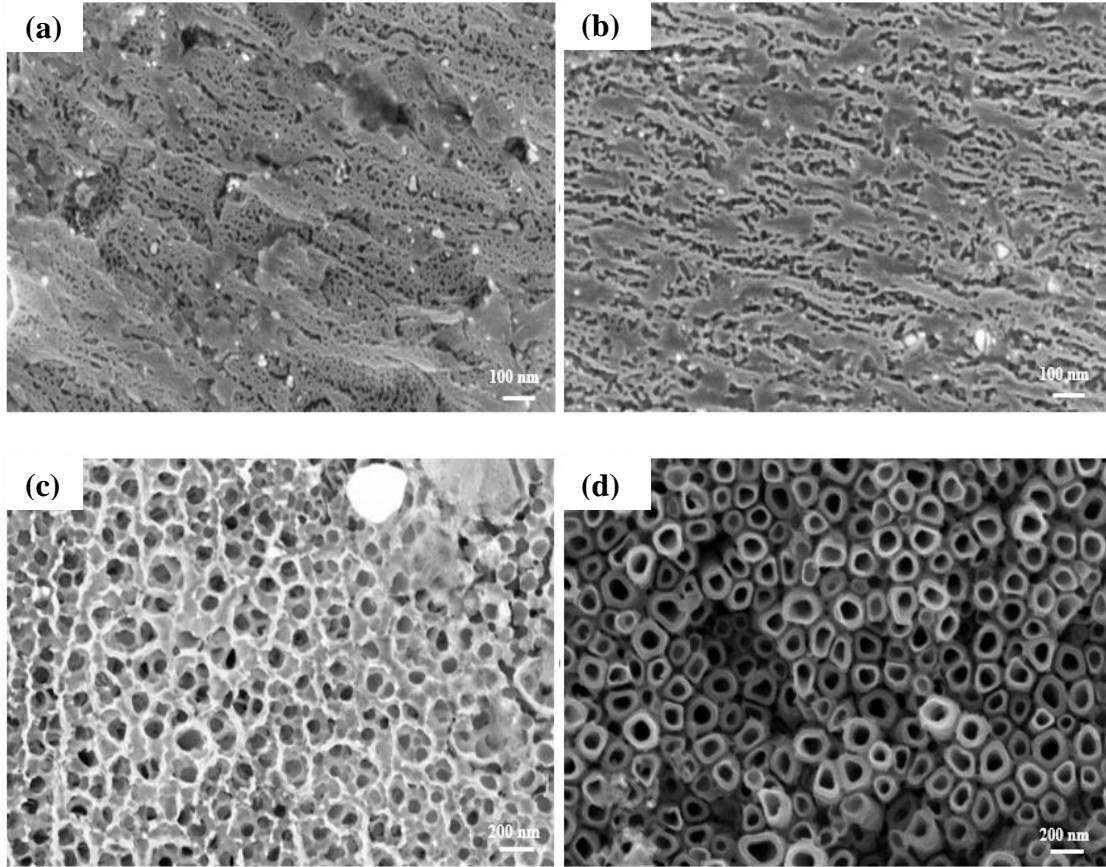
Figure 5.3. FESEM images of nanotubes formed on Ti-45Nb in electrolyte B at 40 V for (a) 10, (b) 20, (c) 40, and (d) 120 min.
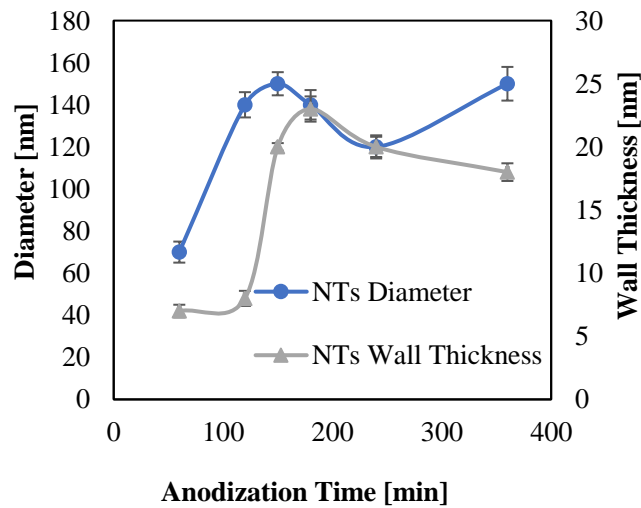
Figure 5.4. Effect of anodization time on the NTs diameter and wall thickness prepared in electrolyte B.

To further decrease the wall thickness of the anodized nanotubes, ethylene glycol was used to obtain uniform unimodal size NT arrays (Figure 5.5) as suggested by Xu et al. [53]. The less

corrosive organic electrolyte would result in uniform NT arrays formed on alloys. The mechanism of NTs formation encompasses two opposing processes, electrochemical etching occurring at the metal/oxide interface while at the tips of the NTs, chemical dissolution takes place [49]. NTs formed from anodizing Ti-45Nb alloy was successfully achieved with optimized dimensions of large diameter and ultrathin wall thickness. It is also interesting to notice that NTs preserved their shape after annealing at 650 ℃ which was not the case with NTs grown on Ti. This makes NTs formed on the surface of the Ti-45Nb alloy much more stable against scratch test compared to NTs grown on the Ti substrate. Similar observation was reported by Yang et al. [95]. Top view FESEM images of NTs grown on Ti-45Nb are shown in Figure 5.5a. The tubes are not all perfectly circular. These variations in the circumferential shape of the NTs were still observed due to differences in chemical composition as reported for Ti13Nb13Zr [56]. The outer diameter of the NTs reached 180-200 nm with ultrathin wall thickness as small as 5-8 nm due to the higher dissolution of oxides as well as migration of anions form the electrolyte as a result of electric field, which in turn is determined by ion size and electrical conductivity. This is of significant importance for better charge carrier dynamics. The layer thickness of the NT arrays was 2-2.8 µm. Figure 5.5b displays the change in NTs diameter and wall thickness with anodization time. From the above results, NTs prepared in electrolyte C at 40 V for 60 min would be used to further characterize their properties (structural and photoelectrochemical).
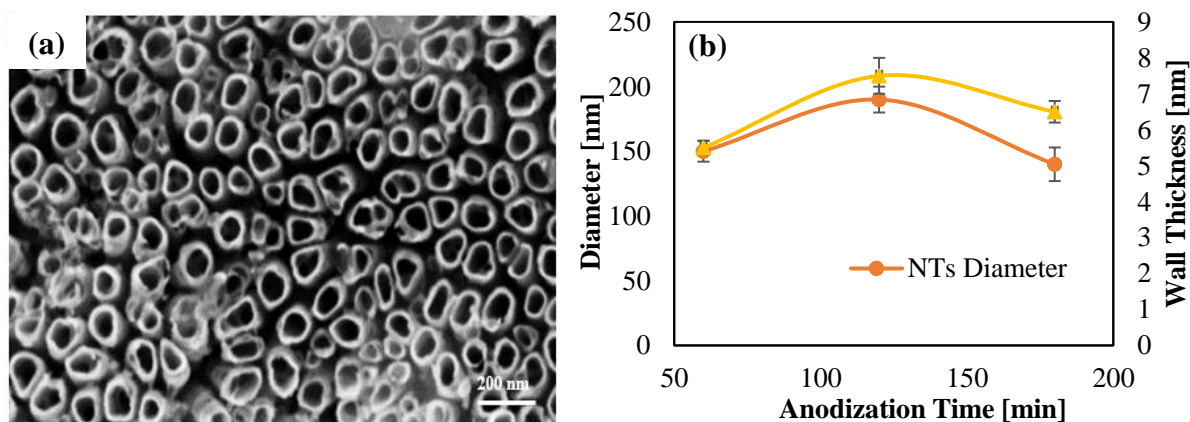
Figure 5.5. (a) FESEM top image of ultrathin NTs prepared in electrolyte C, (b) Effect of anodization time on the NTs diameter and wall thickness anodized in electrolyte C.

It is very difficult to perform BET measurements to get the surface area of the NTs due to the attachment of the tubes to the metal substrate. Hence, geometric roughness factor (R) can be

calculated to indicate the real surface area through the ratio of flat and cylindrical surfaces of the tube arrays (top, bottom, inner, and outer) to the congruous projected area, which is in return a function of length, inner diameter, and wall thickness of the NTs [86]. NTs porosity was also calculated using the same parameters. Porosity and roughness factors were calculated using Eqs. 5.4 and 5.5, respectively [48].

$$P = 1 - \frac{2\pi w(w+d_i)}{\sqrt{3}(d_i+2w)^2} \qquad\qquad (5.4)$$

$$R = 1 + \frac{4\pi l(w+d_i)}{\sqrt{3}(d_i+2w)^2} \qquad\qquad (5.5)$$

where internal tube diameter (d_i), tube length (l), and wall thickness (w). The calculated porosity and roughness were found to be P = 0.885 and R = 92.517, respectively, calculated at d_i=180, w=6, and l=2.5×1000 nm. Whereas in the case of bare TiO_2, P and R were found to be 0.723 and 208.831, respectively, for NTs prepared at the same conditions but with slightly varying dimensions d_i=80, w=8, and l=3×1000 nm.

5.2. Compositional Characterization:

Energy Dispersive X-ray (EDX) of the fabricated NTs was carried out to further investigate the Ti,Nb, and O weight percentages along the formed NTs. Ti/Nb/O weight ratio obtained was 30.19/28.69/41.13 as indicated in the bar chart (Figure 5.6). These percentages support the hypothesis of the formation of mixed oxide of TiO_2 and Nb_2O_5 on the surface of the Ti-45Nb substrate. And this comes in line with the previously reported electrochemical behavior that TiO_2 dissolves in the electrolyte at a faster rate than Nb_2O_5, and with the mechanisms proposed later in the defect equations section for Nb charge compensation by creating Ti vacancies [54]. It was also deduced from the EDX that Ti, Nb, and O elements are uniformly distributed along the NTs through line scan and mapping of different positions of the NTs as shown in the inset of Figure 5.6 [96]. However, EDX does not give any information about the oxidation state of the elements.
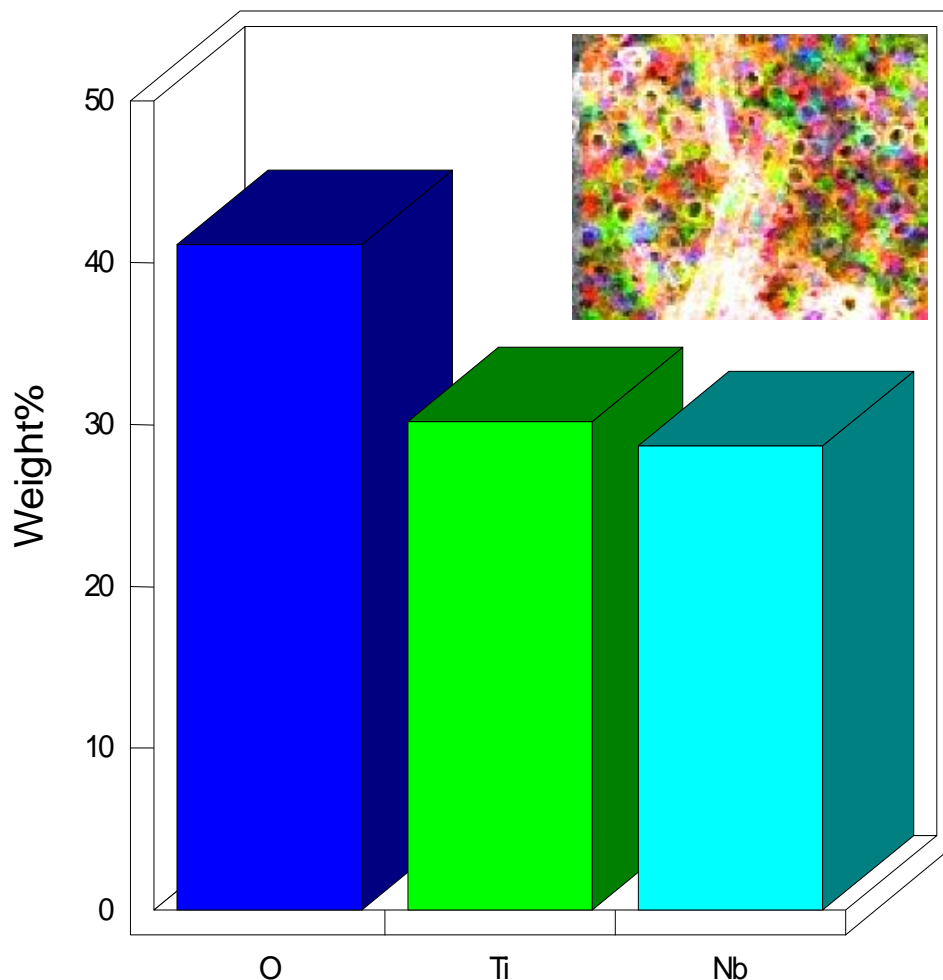
Figure 5.6. EDX weight percentage of Ti, NB, and O present in the NTs anodized in electrolyte C at 40 V for 60 min.

Therefore, XPS was used to confirm Nb presence and determine its chemical state within the oxide. Quantitative evaluation of the survey spectrum was done to determine the chemical composition of the oxide films in terms of atomic percentages. Previous studies showed the higher stability of Nb oxides against chemical etching caused by F^- ions and the preferential dissolution of Ti oxide during electrochemical anodization [34]. Peaks associated with tetravalent Ti and pentavalent Nb appear in XPS spectra (Figure 5.7) with the binding energies values of photoemission spectra corresponding to Ti2p, Nb3d, and metal oxides O1s being 464.88 ($2p_{1/2}$), 459.38 ($2p_{3/2}$), 207.68 ($3d_{3/2}$), 210.38 ($3d_{5/2}$), and 530.58 (O1s), respectively. For Ti2p, the spin orbit splitting was 5.5 eV conforming oxidation state of Ti^{4+} in anatase; while for the Nb3d it was 2.7 eV, which conforms to Nb^{5+} oxidation state. Also, Nb3d binding energy at 207.68 eV and not 206 eV further confirms

Nb^{5+} (Nb$_2$O$_5$) instead of Nb^{4+} (NbO$_2$) [97]. These findings confirm the results of both Raman and XRD where Nb$_2$O$_5$ is formed separately. Note that the position of the peak detected for 1s in the surface-sensitive mode manifested a little shift to lower energies than in the bulk mode.
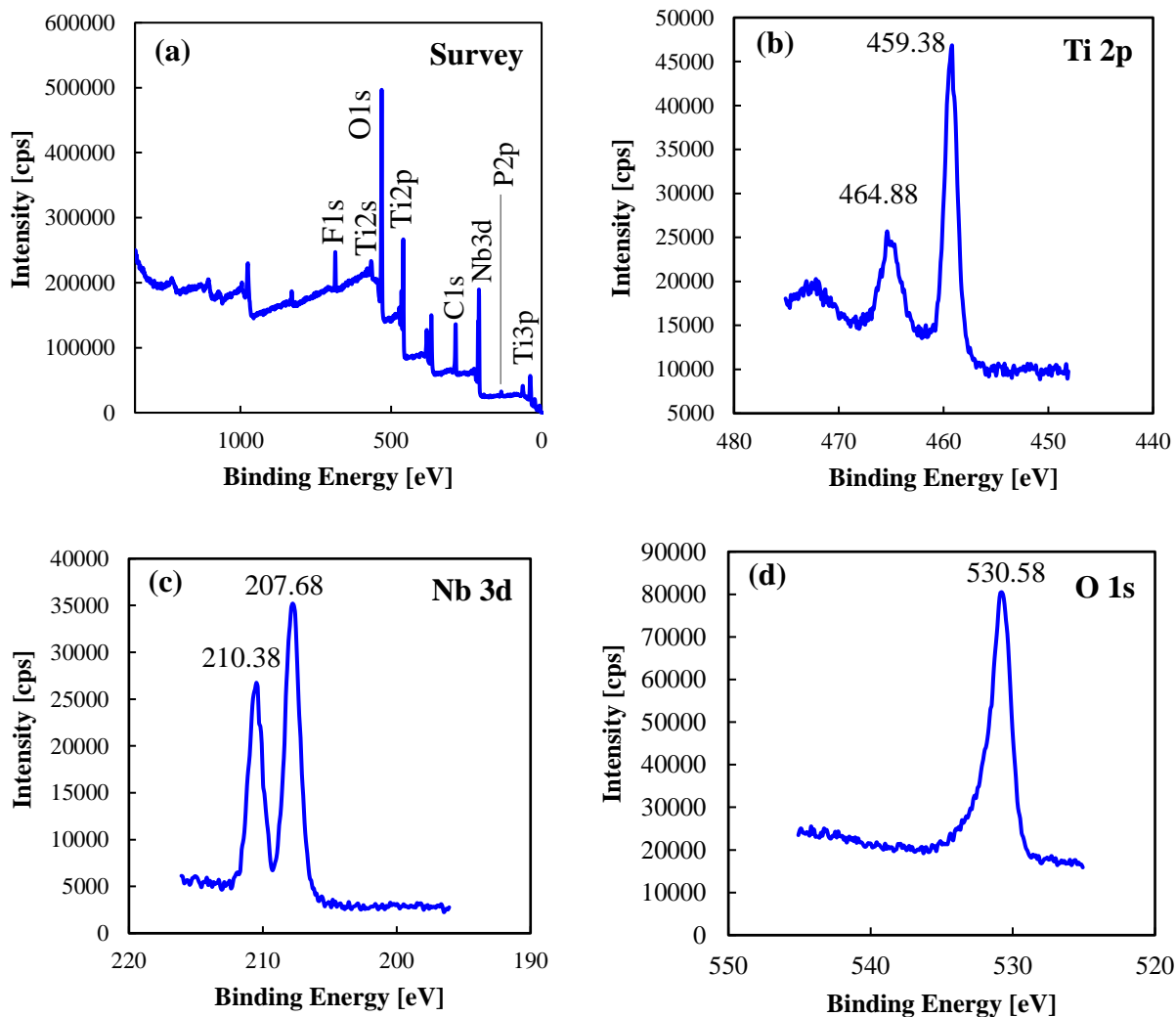
Figure 5.7. XPS spectra of the (a) global survey spectrum, (b) Ti 2p, (c) Nb 3d and (d) O 1s emission peaks for TiO$_2$/Nb$_2$O$_5$ NTs formed in electrolyte C at 40 V for 60 min.

5.3. Structural Characterization:

Understanding both physical and chemical properties of the oxide and being able to correlate these properties will enable us to better control the surface interactions through developing the required oxide properties. Some studies reported the effect of Nb addition on the grain size development, strain, and the phase transformation from anatase to rutile. However, very few systematic investigations have been carried out to correlated physical, structural and photo-electrochemical

properties. NTs surface stability and characteristics as well as phase transitions are affected by the NTs morphology, size, and crystal structure. In the following section will summarize the dependence of XRD and Raman spectra pattern on the size of NTs.

5.3.1. X-ray Diffraction (XRD) Analysis:

Generally, the formed nanotubes are characterized in terms of microstructure and photoelctrochemical performance and efforts are being done to correlate and link both characteristics together. Tremendous interest has been given to TiO_2 NTs [48,87,98,99], however TiO_2 doped or oxide mixture of TiO_2 with other oxides are not being well investigated yet. For instance, there has been a debate in the literature concerning the nature of phases and oxides NTs formed of Ti and Nb either as Nb-doped TiO_2 or for NTs grown on Ti-Nb alloy of various compositions. As a starter, some reported the formation of mixed oxide $Ti_xNb_yO_z$ while others stated that the formed NTs are combination of TiO_2 and Nb_2O_5 oxides [67,80]. Detailed XRD analysis has been conducted so as to resolve this issue through crystal size determination, pattern fitting and matching, and finally relate the proposed structure to the corresponding defect equations.

XRD measurements were carried out to study the effect of evolving crystal structure on the photoelecromechical properties of NTs formed on Ti-45Nb compared to NTs formed on Ti. XRD patterns show that at the beginning no oxide peaks were observed for both NTs, instead, only peaks from the substrate were recorded indicating the amorphous structure. After annealing, reflection peaks appeared for anatase-TiO_2, and with increasing temperature fraction of anatase present in the structure increased (Figure 5.8). Ti-45Nb NTs showed additional peaks for monoclinic Nb_2O_5 appeared indicating the formation of **composite** oxides. Increasing the annealing temperature to 650 ºC leads to the formation of rutile phase in case of NTs grown on bare Ti metal, however, in the case of Ti-45Nb, the presence of Nb hindered the formation of rutile phase at such elevated temperatures (Figure 5.9) and anatase remained the major phase. It was also noted that at higher annealing temperatures, Nb oxides crystallized into orthorhombic rather than monoclinic. The effect of Nb on the mechanism of anatase to rutile phase transformation was studied using peak intensity ratios extracted from XRD spectra to quantify the transformation from anatase to rutile. The anatase/rutile ratio was calculated empirically using Depero et al. relationship (Eq. 5.7):

$$R(T) = 0.679 \frac{I_R}{I_R + I_A} + 0.312 \left(\frac{I_R}{I_R + I_A} \right)^2 \qquad\qquad (5.7)$$

where R(T) is the rutile percentage at different temperatures, I_A is the intensity of anatase diffraction peak (101) ($2\theta = 25.1595°$), and I_R is the intensity of the main rutile diffraction peak (110) ($2\theta = 27.2794°$). It is observed that for samples with no Nb, the antase to rutile ratio reached 0.788 at 650 °C. The transformation from anatase to rutile took place due to coarsening of anatase crystal till it reached the critical size leading to the breakage of Ti-O bond and rearranging in the octahedral site to form rutile [100]. While for samples with Nb, rutile phase did not form till 650 °C and no peaks were observed. TiO_2 film breakdown occurred at 40 V unlike the TiO_2-Nb_2O_5 film confirming the role of Nb in stabilizing the film and suppressing the anodic titania transition from amorphous to crystalline, which is favorable to overcome the weak carrier transport of rutile phase [76,80]. In general, the mixed oxide layers on TiNb have higher mechanical and chemical stability than comparable pure TiO_2 NTs where considerable collapse of the NTs was observed [33,42,51].
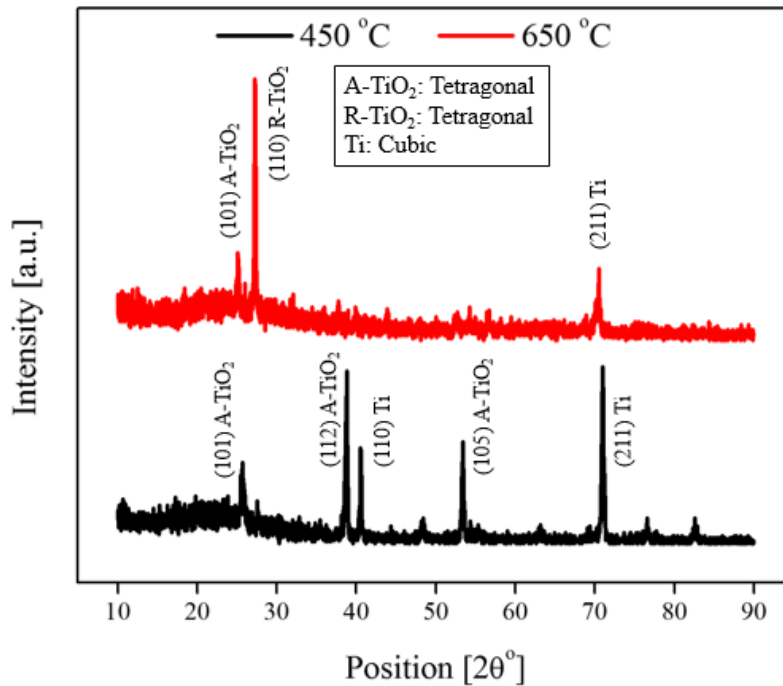
Figure 5.8. XRD pattern of TiO_2 NTs annealed at 450 and 650 °C.

Although some previous work reported the formation of mixed oxides [93], having Nb_2O_5 incorporated into the TiO_2 lattice, our results showed clear evidence of the formation of individual

Nb_2O_5 oxides [42]. Experimental and tabulated data were compared and monoclinic Nb_2O_5 peaks were observed as shown in Figure 5.9. The main anatase peak (101) found in TiO_2 at 25° [78] was slightly shifted to lower positions in TiO_2-Nb_2O_5 NTs (24.9°). The atomic radius of Nb^{5+} is 0.64 °A, whereas that of Ti^{4+} is 0.605 °A, making it easy for Nb^{5+} to substitute Ti^{4+} in the anatase lattice and hence causes a slight increase in the lattice d-spacing, which explains the decrease in the peak position. Pei et al. [101] reported that Nb^{5+} substituting Ti^{4+} in the lattice acts as an n-type dopant and forms hybridized states of Nb4d-Ti3d in the conduction band.
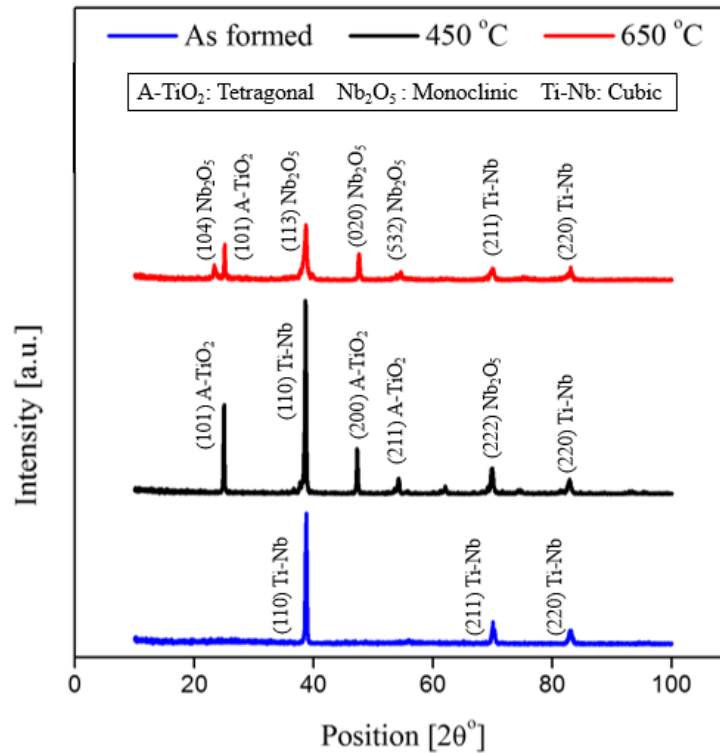
Figure 5.9. XRD pattern of the as formed TiO_2-Nb_2O_5 NTs and annealed at 450 and 650 ºC.

It is important to have a good understanding of physical and chemical properties of the formed oxide to be able to tailor its properties by controlling the various parameters such as crystallite size and induced lattice strain. In this regard, many studies have been carried out to investigate the effect of Nb doping on the TiO_2 lattice [74,75,102], whereas very few systematic researches have been conducted on TiO_2-Nb_2O_5. Accordingly, the mean crystallite size, lattice parameters and microstrain were calculated using Debye-Scherrer's equation, Bragg's equation and Wilson's equation (Eqs. 5.8, 5.9 a,b, 5.10) [103]. The results are listed in Tables 5.1 and 5.2.

$$d = \frac{0.9\lambda}{\beta \cos\theta} \tag{5.8}$$

$$n\lambda = 2d \sin\theta \tag{5.9}$$

$$\frac{1}{d^2} = \frac{h^2 + k^2}{a^2} + \frac{l^2}{c^2} \; Tetragonal \tag{5.9-a}$$

$$\frac{1}{d^2} = \frac{1}{\sin^2\beta}\left(\frac{h^2}{a^2} + \frac{k^2 \sin^2\beta}{b^2} + \frac{l^2}{c^2} - \frac{2hl \, \cos\beta}{ac}\right) Monoclinic \tag{5.9-b}$$

$$\varepsilon = \frac{\beta_\varepsilon}{4 \tan\theta} \tag{5.10}$$

where d is the mean crystallite size, the shape factor equals to 0.9, λ is the x-ray wavelength of 1.5406 Å, β is the instrument broadening due to crystallite size at half the maximum intensity (full-width at half-max or FWHM), which is obtained after instrumental correction (i.e. βstructural = βobserved – βstandard) using Si standard sample, θ is half the Bragg diffraction angle, n is integer number, d is the spacing between planes with Miller indices (hkl), and β_ε is the broadening due to lattice strain in radian.

Figure 5.8 shows that for bare TiO_2 NTs, increasing annealing temperature leads to narrowing of the peaks width, which indicates the extent of crystallinity of structure and the increase in the crystallite size and lattice parameters for both anatase and rutile. Whereas a decrease in the micro-strain was observed (Table 5.1). This might be referred to the higher temperature providing higher energy for the growth of the crystal grains, removal of the grain boundary defects, and relief of the internal stresses which in turn reduces the lattice strain [98,99]. Pabu at al. [99] reported that higher strain values are caused by excess amount of atom and defects present in the amorphous grain boundaries, which results in a stress field and introduces strain in the region.

As for TiO_2-Nb_2O_5 NTs, Table 5.2. indicates that anatase (101) lattice parameters were enlarged due to insertion of Nb with larger ion size into 4a Wyckoff site [65]. Both *a* and *c* lattice parameters increased from 3.762 and 9.457 Å to 3.838 and 10.315 Å. However, with increasing annealing temperature, a decrease in the crystallite size and lattice parameters, corresponding to peaks broadening and shift to lower diffraction angles, was observed for both phases present of tetragonal anatase and monoclinc pentoxide (Figure 5.9). This might be owing to the increased number of defects present within the lattice in addition to the role Nb plays in hindering the ability of the grains to grow and release the stresses and consequently reduce the strain. Moreover, it was

suggested that grain coarsening obstruction might be attributed to decreased ionic oxygen mobility [104].

Table 5.1. Summary of the lattice parameters, crystallite size, induced microstrain, and mass fraction of anatase and rutile phases present within TiO$_2$ NTs.

Annealing Temperature [°C]	Phase	Lattice Parameters [Å]		Crystallite Size [nm]	Micro-strain (ε)	Mass Fraction
		a = b	c			
450	Anatase (1 0 1)	3.762	9.457	24.37	0.00809	---
650	Anatase (1 0 1)	3.868	9.741	37.63	0.00585	0.21154
	Rutile (1 1 0)	4.623	2.966	41.57	0.005	0.78846

Table 5.2. Summary of the lattice parameters, crystallite size, induced microstrain, and mass fraction of tetragonal TiO$_2$ anatase and monoclinic Nb$_2$O$_5$ phases present within and TiO$_2$-Nb$_2$O$_5$ NTs.

Annealing Temperature [°C]	Phase	Lattice Parameters [Å]			Crystallite Size [nm]	Micro-strain (ε)
		a	b	c		
450	Tetragonal Anatase (1 0 1)	3.838		10.315	128.97	0.00253
	Monoclinic Nb$_2$O$_5$ (1 1 3)	4.572	3.448	13.141	52.80	0.00297
550	Tetragonal Anatase (1 0 1)	3.846		9.421	103.48	0.0029
	Monoclinic Nb$_2$O$_5$ (1 1 3)	4.033	3.803	12.89	45.67	0.0033
650	Tetragonal Anatase (1 0 1)	3.83		9.502	80.36	0.00341
	Monoclinic Nb$_2$O$_5$ (1 1 3)	4.016	3.634	12.837	21.12	0.00606

The previous experimental results could be correlated with the chemistry of point defects present in the structure. The XPS data confirmed the presence of Nb^{5+} and the XRD results depicted small

changes in the induced strain upon addition of Nb due to the resemblance of atomic radii in six-fold coordination for both Nb^{5+} (50.70 Å) and Ti^{4+} (0.68 Å), which corresponds to what Arbiol et al. [102] suggested that Nb insertion into the TiO_2 phases would be based mainly on how charge compensation is achieved instead of stresses being induced.

Generally, the anatase is considered n-type semiconductor due to the presence of oxygen vacancies at the ambient temperature and pressure. Other types of defects also exist within the anatase structure such as Ti vacancies and interstitials with different ionization degree. However, the most influential defects on the properties are oxygen vacancies (2+), Ti interstitial (Ti^{3+}), Ti vacancy (Ti^{4+}), and electronic defect caused by electron holes localized on the sites of O^- ion and electrons localized on the sites of Ti^{3+} in the lattice [102,105]. This also can be referred to the well-known fact of ioninc compounds tendency to form Schottky (cation V_{Ti}'''' and anion $V_O^{\bullet\bullet}$ vacancy) and Frenkel ($Ti_i^{\bullet\bullet\bullet}$) defects (Eq. 5.11) [65].

$$O_O^x \leftrightarrow V_O^{\bullet\bullet} + 2e' + \frac{1}{2}O_2(g) \tag{5.11-a}$$

$$2O_O + Ti_{Ti} \leftrightarrow Ti_i^{\bullet\bullet\bullet} + 3e' + O_2(g) \tag{5.11-b}$$

$$O_2 \leftrightarrow 2O_O + V_{Ti}'''' + 4h^{\bullet} \tag{5.11-c}$$

$$nil \leftrightarrow e' + h^{\bullet} \tag{5.11-d}$$

$$Ti_{Ti}^x + 2O_O^x \rightarrow V_{Ti}'''' + 2\,O_O^{\bullet\bullet} + TiO_2(surface) \tag{5.11-e}$$
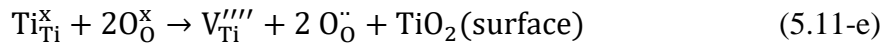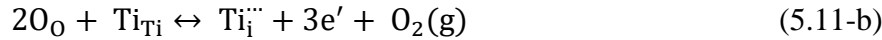
where O_O^x, $V_O^{\bullet\bullet}$, $Ti_i^{\bullet\bullet\bullet}$, V_{Ti}'''' represents oxygen ion of neutral charge on a regular oxygen site, doubly ionized oxygen vacancies, trivalent Ti interstitial, and tetra-valent Ti vacancies, respectively. While e' denotes electron and $h^{\bullet}$ denotes hole. Oxygen vacancies are considered the majority charge carriers. As the electrically charged vacancies are being compensated through electrons ejection to the conduction band.

As for the NTs grown on the Ti-45Nb surface, the expected charge compensation would be achieved by the following equilibria reactions (Eq. 5.12):

$$Nb_2O_5 \rightarrow 2\,Nb_{Ti}^{\bullet} + 4O_O^x + O_i'' \tag{5.12-a}$$

$$2Nb_2O_5 \rightarrow 4Nb_{Ti}^{\bullet} + V_{Ti}'''' + 10O_O^x \tag{5.12-b}$$

$$Nb_2O_5 \rightarrow 2Nb_{Ti}^{\cdot} + 2e' + 4O_O^x + \frac{1}{2}O_2(g) \qquad\qquad (5.12\text{-c})$$
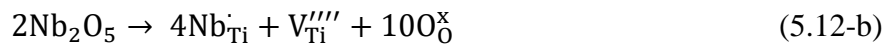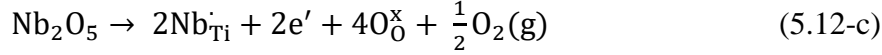
where, $Nb_{Ti}^{\cdot}$ accounts for Nb^{5+} substitutionally replacing cation Ti site (Ti^{4+}) in the lattice causing the above stated 3 mechanisms for charge compensation via insertion of oxygen interstitial (O_i'') per two Nb, fully ionized titanium vacancies (V_{Ti}'''') per four Nb, and formation of two free electrons (2 e') per two Nb. However, this free electron may reduce Ti^{4+} into Ti^{3+} (Ti_{Ti}') per Nb introduced. It was previously mentioned in literature that the reduction of Ti^{4+} is more likely to occur at higher temperatures and under reducing conditions. Annealing in oxidizing atmosphere would favor the formation of Ti vacancies as demonstrated by Sheppard et al. [106] and Mei et al. who assumed that charge compensation would be achieved by the formation of Ti vacancies. [74] One should expect the amount of oxygen vacancies to reduce at the expense of the extra positive charge added to the Ti lattice as a result of Nb introduction [102]. However, oxygen vacancies were reported to be the prevailing ionic defects instead of electronic Nb compensation when the NTs treatment is carried out in very low conditions of oxygen activity at which the behavior is intrinsic [106]. The following chemical equilibria governs the oxygen vacancies formation (Eq. 5.13):

$$O_O^x \leftrightarrow V_O^{\cdot\cdot} + 2e' + \frac{1}{2}O_2(g) \qquad\qquad (5.13)$$
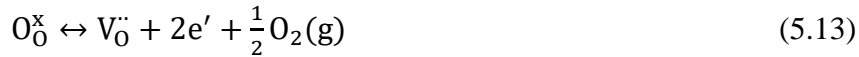
This would in turn has an influence on the photoelectrochemical properties as described below.

5.3.2. Raman Analysis:

Phase evaluation, bond configuration, and short-range order of annealed Ti and TiNb samples were further investigated using Raman spectroscopy to confirm the XRD results. From the Raman spectra displayed in Figure 5.10, the as-prepared NTs exhibited two very broad bands at 190 and 450 cm^{-1}, which are assigned to Ti-O bending and at 610 cm^{-1} for Ti-O stretching. Those bands with the additional broad feature appearing at 894 cm^{-1} confirms the existence of amorphous TiO_2 [107]. However, the annealed NTs showed the four well known characteristics bands present in TiO_2 at 144, 394, 518, and 630 cm^{-1} which are attributed to anatase TiO_2 of tetragonal structure with D^{4th} space groups [108-111]. These bands are associated with Eg (O-Ti-O symmetric stretching), B1g (O-Ti-O symmetric bending), A1g (O-Ti-O Antisymmetric bending), and Eg (O-Ti-O symmetric stretching) lattice vibrational modes of TiO_2 tetragonal anatase, respectively [112,113]. Additionally, weak shoulder appears at 196 cm^{-1} corresponding to Eg mode.
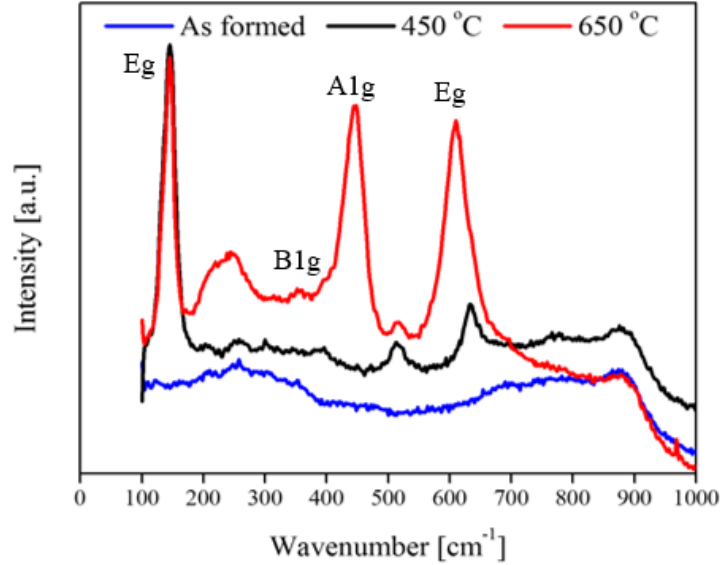
Figure 5.10. Raman spectra of as formed TiO_2 NTs, and TiO_2 NTs annealed at 450 and 650 ºC

As annealing temperature is increased from 450 to 650 °C (Figure 5.10), rutile starts to evolve as indicated by the bands at 242, 450 (Eg mode), and 615 (A1g mode) cm^{-1}. Although anatase peaks still exist, the rutile phase becomes the dominant at 650 °C. [114] Anatase to rutile transformation is observed to be hindered at elevated temperatures due to the presence of Nb. Such findings are consistent with XRD results and the finding of Pittman and Bell [115]. Accordingly, the optimum annealing temperature would be 450 °C, where anatase phase is dominant allowing enhanced electrons percolation and hence increased photocurrents. This is why it is preferred in photovoltaic applications [116].

On the other hand, as shown in Figure 5.11, the NTs grown on Ti-Nb alloy showed anatase structure with additional peak at 948 cm^{-1} which can be ascribed to Nb=O vibrations [71, 115]. Peaks shift and broadening due to distortion as well as polarization occurring to TiO_6 octahedra, internal strain, and charge imbalance as a result of Nb^{5+} being of higher valence and bigger ionic radius compared to Ti^{4+} was observed. The resulting non-stoichiometry accounts for the change in the lattice vibrations [117]. The Eg peaks shift to lower wave number at 144 and 630 compared to 148 and 648 are correlated with longer bond length. The shoulder peak appearing at 690 cm^{-1} refers to orthorhombic Nb_2O_5 (O-Nb-O symmetric stretching mode) [118].

Rutile to anatase weight ratio was found to follow linear relationship [$W_{R/A} = 3.64 \times (I_{446}/I_{396})$] during the study of physical crystalline mixtures of anatase and rutile. [114] This semi-quantitative

measure of the rutile to anatase weight ratio uses intensity of Raman peaks for rutile at 446 cm^{-1} and anatase at 396 cm^{-1}. The relative concentration of rutile increased from $W_{R/A} = 2.165$ at 450 ºC to $W_{R/A} = 8.9$ at 650 ºC. It is worth mentioning that this is applied with the limitation that it is semi-quantitative since the cross sections of Raman scattering of anatase and rutile vary with the degree of crystallinity [13]. The broad signal at 900 cm^{-1} corresponds to Ti=O stretching when the oxide is interacting with metal clusters [119]. Covalence / bond length / frequency correlations were used to relate Ti-O bond length (R) and Raman frequency shift (v) through the following relationship (Eq. 5.6):

$$\nu_{Ti-O} = 722e^{-1.54946(R-1.809)} \qquad\qquad (5.6)$$

Calculated bond lengths for Ti-O bonds present in the amorphous titania at 610 and 450 cm^{-1} are found to be 5×1.92 and 2.11 Å corresponding to TiO_6^{8-} octahedra, which agree with the average structures of TiO_2 anatase and rutile phases having average calculated bond lengths of 5×1.93 and 2.12 Å [114].

Raman bands observed for anatase at 630, 518, and 394 cm^{-1} (Figure 5.10) gave corresponding Ti-O bond lengths of 2×1.90, 3×2.02, and 2.19 Å compared to previously reported Ti-O bond lengths of 4×1.9338 and 2×1.9797 Å for bulk anatase, which indicate some degree of distortion in TiO_6^8. Also, the calculated bond length for the most intense Raman band observed at 144 cm^{-1} is 2.85 Å corresponding to Ti-Ti bonding in the octahedral chains.

As for NTs anodized on Ti-45Nb, bond length calculations support the findings of our XRD results of smaller crystallite size. The calculated Ti-O bond length equivalent to shifted Raman band at 648 cm^{-1} is slightly smaller [2×1.88 Å, and 2.83 Å] for the Raman band at 148 cm^{-1}, which is consistent with Ti-Ti bonding.
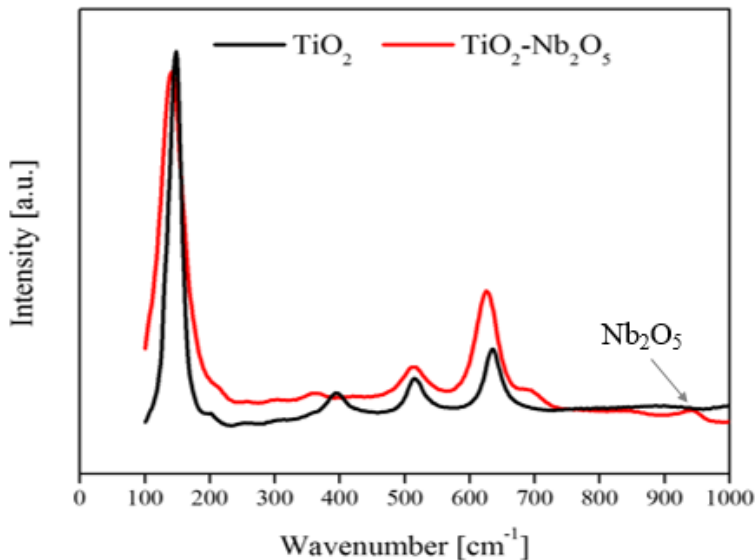
Figure 5.11. Raman spectra of as formed TiO_2 NTs, and TiO_2-Nb_2O_5 NTs annealed at 450 ℃.

5.4. Optical and Photoelectrochemical Characterization:

Figure 5.12a,b shows the absorption spectra of the fabricated TiO_2 NTs. The samples demonstrated light absorption till early visible light region. Some samples showed high absorption tail in the visible light region due to light scattering caused by the metal substrate underneath the NT arrays [78].
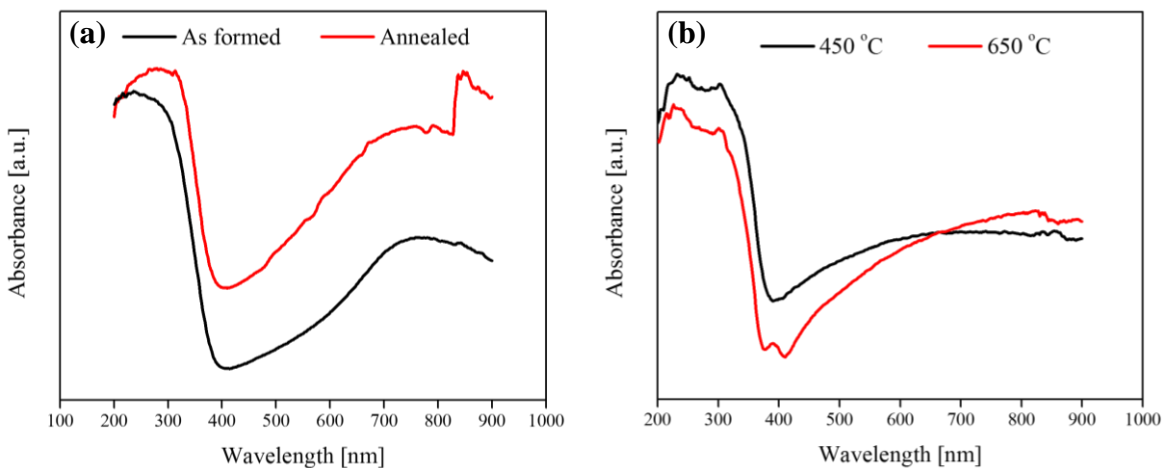
Figure 5.12. Absorption spectra of TiO_2 NTs; (a) as formed versus annealed at 450 ℃, (b) annealed at 450 versus 650 ℃.

The NT arrays grown on Ti-45Nb showed slightly shifted light absorption compared to those grown on Ti (Figure 5.13a), which could be attributed to the higher distortion in the crystal lattice

64

as a result of NT specific architecture in addition to the larger NTs diameters which will in turn cause stronger light scattering and thus better light-harvesting efficiencies [78,120]. Shallow defect states created by oxygen vacancies just below the conduction band by 0.75 eV and 1.18 eV facilitate the absorption of visible light, and thus the electrons present at these defect states can be easily diffused to the surface [121].

Moreover, earlier studies confirmed that red shift observed in the UV-vis spectrum is attributed to pentavalent oxide and demonstrated the absence of Burstein-Moss effect resulting from filling conduction band. Brancho and Barlett referred red shift to Nb(4d) states being within anatase TiO_2 conduction band, which is then thought to lead to absorption between impurity pairs [16]. In the present study, the formation of mixed oxide was noted and evidenced with Raman as well as XRD results. One more feature apparent in the absorption spectra of Ti-Nb NTs is the higher background level occurring at longer wavelengths (615 nm) is indication of more defects generated as well as trapped holes [122,123]. As noted in XRD results, upon annealing more defects are introduced into the system, this might explain the finding that annealed TiO_2-Nb_2O_5 NTs showed rather shifted light absorption.

The Ti-45Nb NTs, they absorbed till $\approx$ 390 nm corresponding to band gap of $\approx$ 3.2 eV by extrapolating the linear part of the absorption curves presented in the inset of Figure 5.13b while for tubes grown on Ti, they absorbed till $\approx$ 400 nm with band gap of 3.25 eV.
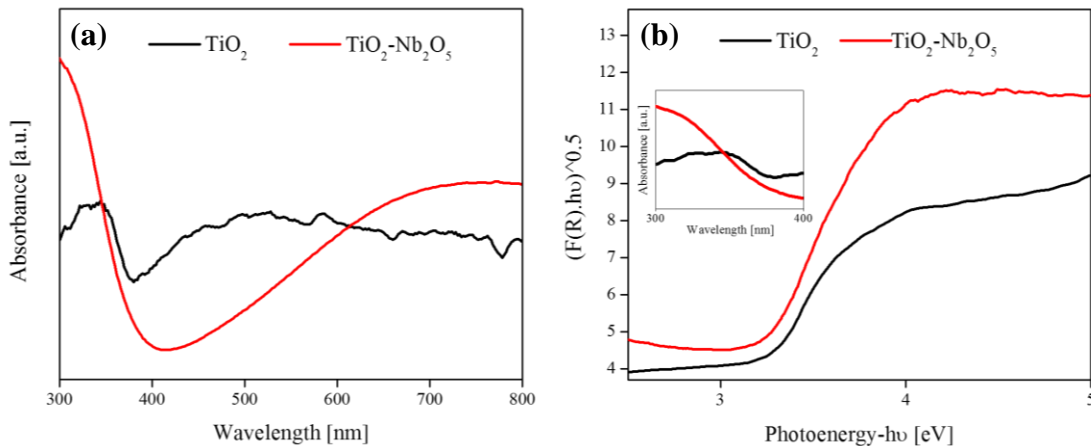
Figure 5.13. (a) The absorption spectra of TiO_2 compared to TiO_2-Nb_2O_5 NTs, and (b) Tauc plot of TiO_2 and TiO_2-Nb_2O_5.

Although the absorption was nearly the same for TiO_2 and TiO_2-Nb_2O_5 NTs, higher photocurrent was observed for TiO_2-Nb_2O_5 NTs (Figure 5.14). Photoelectrochemical measurements showed much higher photocurrent for NTs anodized on Ti-Nb alloys (0.3 mA/cm^2) than on Ti (0.18 mA/cm^2) prepared under the same conditions for the sake of comparison.

Several microstructural factors play a role in the resulting photocurrent behavior. These factors might have contradicting effect on the photoelectrochemical behavior. For instance, these factors include the defects, conductivity, absorption, crystallite size, lattice microstrain, surface roughness, and NTs dimensions. The mechanism by which each factor impacts the eventual photocurrent differs. Defects existing within the crystal lattice as stated above in the defect equations showed that the most dominant defects were oxygen vacancy and subsequently faster carrier mobility.
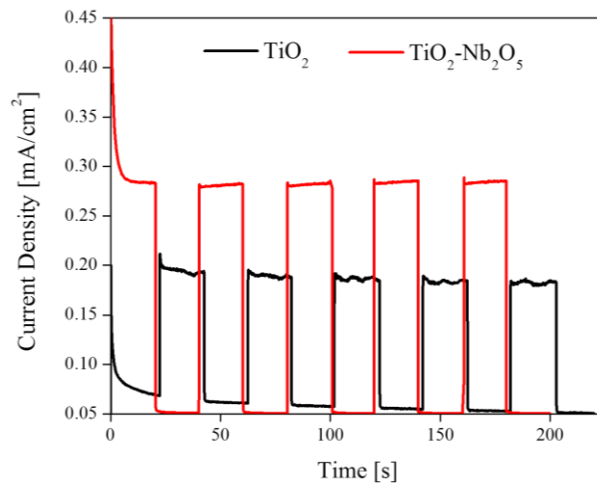
Figure 5.14. Photocurrent-time measurement of TiO_2 and TiO_2-Nb_2O_5 NTs.

In addition to the well-established understanding that Nb enhances the conductivity of TiO_2 NTs, and consequently accelerates the charge carrier transfer within the oxide, crystallite size as well as lattice microstarin also affect the charge carrier dynamics. The greater crystallite size of TiO_2-Nb_2O_5 compared to TiO_2 means reduced boundary crystallite region, which could be related to recombination sites of the photogenerated charge carriers and eventually higher charge collection efficiency [124]. The TiO_2-Nb_2O_5 NTs had smaller microstrain than TiO_2, indicating fewer substoichiometric Ti^{2+} and Ti^{3+} defects in the oxides NTs and thus had detrimental influence on the electron transport [125]. Hence, better charge dynamics contribute to the higher photocurrent. Having low recombination rate could indicate that formed defects and electron traps are shallow.

66

In Figure 5.14 TiO$_2$-Nb$_2$O$_5$ shows stable photocurrent over time, while TiO$_2$ NTs experienced slight decrease in photocurrent with time, which indicates more recombination occurring. This may indicate as well shallow localized states rather than deep ones.

Geometric smoothness and orderliness enhanced the charge transfer [126]. Therefore, charge mobility would be better for TiO$_2$-Nb$_2$O$_5$ NTs with much lower surface roughness (as calculated earlier) rather than TiO$_2$ NTs. Being able to fabricate thin-wall NTs of composite TiO$_2$ and Nb$_2$O$_5$ with relatively large diameter had a positive influence on both photon absorption due to the large diameter as mentioned earlier. Small wall thickness leads to efficient electron-hole separation since such wall thickness is being smaller than minority carrier (holes) diffusion length [127]. Furthermore, holes are not separated far from the semiconductor-electrolyte interface. Wall thickness restricts the anatase crystallite width. Potential drop across the wall thickness s governed by Eq. 5.14:

$$\Delta\phi_0 = kTr_0{}^2/6eL_D^2 \tag{5.14}$$

where T is temperature, r$_0$ is half wall width, L$_D$ is Debye length which can be represented as shown in Eq. 5.15 [127]:

$$L_D = [\varepsilon_0\varepsilon kT/2e^2N_D]^{1/2} \tag{5.15}$$

where N$_D$ is the number of ionized donors per unit volume [cm^3].

Incident Photon-to-Current Conversion Efficiency (IPCE) was measured for TiO$_2$ and TiO$_2$-Nb$_2$O$_5$ NTs in order to study the effect of Nb alloying on the performance of the material. The IPCE response is presented in Figure 5.15 where a shift towards longer wavelengths is evident. The cut-off of incident photon to current efficiency (IPCE) for the mixed oxide TiO$_2$-Nb$_2$O$_5$ NTs was shifted to higher wavelengths (475 nm) than TiO$_2$ (380 nm). Such enhancement in the photoresponse is attributed to improved electron mobility due to the aforementioned reasons and may indicate that band gap of TiO$_2$-Nb$_2$O$_5$ was slightly lowered (fermi level shifted near the conduction band).
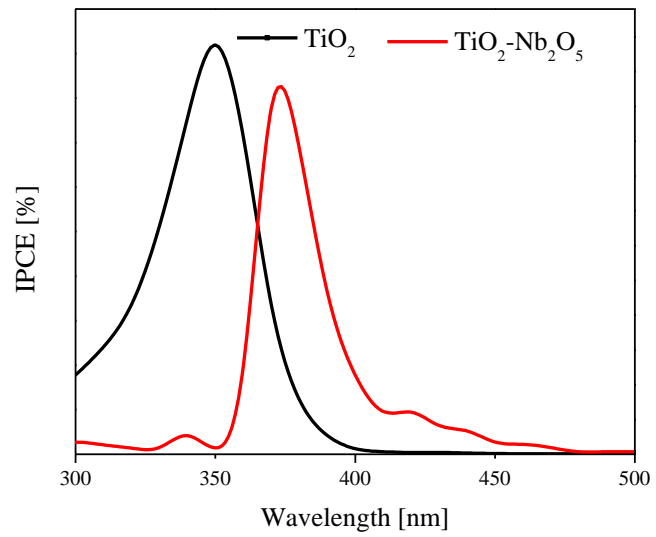
Figure 5.15. IPCE measurements of TiO_2 and TiO_2-Nb_2O_5.

Chapter VI

Conclusion and Future Recommendations

6. Chapter VI: Conclusion and Future Recommendation

6.1. Conclusions:

In the present study, ultra-thin wall nanotubes of complex oxides were successfully obtained with very good ordering and smoothness. The nanotubes were fabricated via anodization process in an organic electrolyte to produce 5 – 8 nm wall thickness, 180 – 200 nm diameter and 2 – 2.8 µm. Such geometry of large diameter would allow for maximum solar light absorption, whereas small wall thickness would allow better charge carrier transfer. Optimized annealing temperature to crystalline the amorphous oxide was found to be at 450 ℃. Raising annealing temperature up till 650 ℃ did not result in the formation of rutile emphasizing the role of Nb in stabilizing the anatase phase. Some compositional and structural characterization techniques of Raman, XRD, XPS, and EDX were combined to help study and revealed the formation of complex oxides of TiO_2-Nb_2O_5 on the expense of $Ti_xNb_yO_z$ reported elsewhere. Besides Nb peak appearing in the Raman spectra, such findings were confirmed via crystal size measurements, lattice parameters, and induced microstrain. The attained nanotubes exhibited enhanced stability over a wide range of annealing temperatures where the transition from anatase to rutile shifted to higher temperature. Besides the NTs arrays showed better mechanical stability and higher resistance to scratch and detachment from the substrate. A correlation between the resultant structure with photocurrent was made to elucidate the increase in the photocurrent, thus the more efficient water splitting. To this end, correlation between structure, property, and function was demonstrated and accomplished to aid design and tailor photoanodes with controlled morphology, crystallinity, shallow trap states (local defects), and electronic properties of Ti-Nb based photoanodes via anodization and post thermal treatment.

6.2. Future Work:

Having been able to fabricate mixed oxide nanotubes of TiO_2 and TiO_2-Nb_2O_5 with ultra-thin walls, electrochemical enhancement was achieved as a result of NTs morphology on addition to the Nb existence which enhanced the electrochemical efficiency. Suggestion for future work would be co-doping the nanotubes, i.e to combine cationic doping (Nb) with anionic doping (Nitrogen, N). This could be performed through annealing the obtained NTs in different atmospheres such as Hydrogen (H_2) and ammonia (NH_3) rather than just air. Although the effect of both medium on the optical and electrical performance is not well understood yet, earlier studies reported that H_2

and NH_3 annealing would passivate surface traps and hence improve charge carrier separation and collection by reducing recombination in addition to decreasing the band gap by creating defect band just below the conduction band and consequently improve the absorption and shift it to the visible region of the solar spectrum. Although N-doping could be hard to achieve since it is unstable and easy to diffuse away of the structure, Nb presence within TiO_2-Nb_2O_5 was reported to enhance N-insertion and thus gives better stability of the obtained layer. This is expected to boost the photoelectrode efficiency. To develop deep understanding of the reactions occurring at the surface of the photoelectrode, impedance and Mott Schottky are to be performed. This would give clear visualization and understanding of the electronic structure of the resulting mixed oxide/oxynitride photoanodes.

References

7. References:

[1] The World's Energy Problem and what we can do about it, American Academy of Arts and Science, Berkeley, November 2007.

[2] Jafari, Tahereh, Ehsan Moharreri, Alireza Shirazi Amin, Ran Miao, Wenqiao Song, and Steven L. Suib. "Photocatalytic water splitting—the untamed dream: a review of recent advances." *Molecules* 21, no. 7 (2016): 900.

[3] Chen, Zhebo, Huyen N. Dinh, and Eric Miller. "Photoelectrochemical water splitting." *SpringerBriefs in Energy*, New York (2013): 49-61.

[4] Herron, Jeffrey A., Jiyong Kim, Aniruddha A. Upadhye, George W. Huber, and Christos T. Maravelias. "A general framework for the assessment of solar fuel technologies." *Energy & Environmental Science* 8, no. 1 (2015): 126-157.

[5] Chen, Xiaoping, Zhixiang Zhang, Lina Chi, Aathira Krishnadas Nair, Wenfeng Shangguan, and Zheng Jiang. "Recent advances in visible-light-driven photoelectrochemical water splitting: Catalyst nanostructures and reaction systems." *Nano-Micro Letters* 8, no. 1 (2016): 1-12.

[6] Why LIFE: Tackling the Global Energy Crisis, Lawrence Livermore National Laboratory, November 2014.

[7] Byrne, John, Kristen Hughes, Wilson Rickerson, and Lado Kurdgelashvili. "American policy conflict in the greenhouse: Divergent trends in federal, regional, state, and local green energy and climate change policy." *Energy Policy* 35, no. 9 (2007): 4555-4573.

[8] Solomon, Susan, Gian-Kasper Plattner, Reto Knutti, and Pierre Friedlingstein. "Irreversible climate change due to carbon dioxide emissions." *Proceedings of the national academy of sciences* 106, no. 6 (2009): 1704-1709.

[9] Di Primio, Rolando, Brian Horsfield, and Mario A. Guzman-Vega. "Determining the temperature of petroleum formation from the kinetic properties of petroleum asphaltenes." *Nature* 406, no. 6792 (2000): 173-176.

[10] Barbier, Enrico. "Geothermal energy technology and current status: an overview." *Renewable and Sustainable Energy Reviews* 6, no. 1 (2002): 3-65.

[11] Dincer, Ibrahim, and Calin Zamfirescu. *Sustainable energy systems and applications*. Springer Science & Business Media, 2011.

[12] Parida, Bhubaneswari, S Iniyan, and Ranko Goic. "A review of solar photovoltaic technologies." *Renewable and sustainable energy reviews* 15, no. 3 (2011): 1625-1636.

[13] Xie, W. T., Y. J. Dai, R. Z. Wang, and K. Sumathy. "Concentrated solar energy applications using Fresnel lenses: A review." *Renewable and Sustainable Energy Reviews* 15, no. 6 (2011): 2588-2606.

[14] Roger, Isolda, Michael A. Shipman, and Mark D. Symes. "Earth-abundant catalysts for electrochemical and photoelectrochemical water splitting." *Nature Reviews Chemistry* 1, no. 0003 (2017): 1-13.

[15] Smestad, Greg P. "Light, Water, Hydrogen: The Solar Generation of Hydrogen by Water Photoelectrolysis, Craig A. Grimes, Oomman K. Varghese, Sudhir Ranjan. *Springer*, New York, USA (2008), ISBN: 978-0-387-33198-0." (2009): 387.

[16] Brancho, James J., and Bart M. Bartlett. "Challenges in co-alloyed titanium oxynitrides, a promising class of photochemically active materials." *Chemistry of Materials* 27, no. 21 (2015): 7207-7217.

[17] Chen, Zhebo, Huyen N. Dinh, and Eric Miller. "Photoelectrochemical water splitting." *SpringerBriefs in Energy,* New York (2013): 49-61.

[18] Fujishima, Akira, and Kenichi Honda. "Electrochemical photolysis of water at a semiconductor electrode." *Nature* 238, no. 5358 (1972): 37-38.

[19] Linsebigler, Amy L., Guangquan Lu, and John T. Yates Jr. "Photocatalysis on TiO_2 surfaces: principles, mechanisms, and selected results." *Chemical Reviews* 95, no. 3 (1995): 735-758.

[20] Kudo, Akihiko, and Yugo Miseki. "Heterogeneous photocatalyst materials for water splitting." *Chemical Society Reviews* 38, no. 1 (2009): 253-278.

[21] Maeda, Kazuhiko, and Kazunari Domen. "Photocatalytic water splitting: recent progress and future challenges." *The Journal of Physical Chemistry Letters* 1, no. 18 (2010): 2655-2661.

[22] Kubacka, Anna, Marcos Fernández-García, and Gerardo Colón. "Advanced nanoarchitectures for solar photocatalytic applications." *Chemical Reviews* 112, no. 3 (2012): 1555-1614.

[23] Osterloh, Frank E. "Inorganic nanostructures for photoelectrochemical and photocatalytic water splitting." *Chemical Society Reviews* 42, no. 6 (2013): 2294-2320.

[24] Li, Yunguo, Yan-Ling Li, Baisheng Sa, and Rajeev Ahuja. "Review of two-dimensional materials for photocatalytic water splitting from a theoretical perspective." *Catalysis Science & Technology* 7, no. 3 (2017): 545-559.

[25] Maeda, Kazuhiko. "Photocatalytic water splitting using semiconductor particles: history and recent developments. " *Journal of Photochemistry and Photobiology C: Photochemistry Reviews* 12, no. 4 (2011): 237–268.

[26] T. Bak, J. Nowotny, M. Rekas, C.C. Sorrell "Photo-electrochemical hydrogen generation from water using solar energy. Materials-related aspects" *International Journal of Hydrogen Energy* 27 (2002): 991–1022.

[27] Subramanian, Vaidyanathan Ravi, et al. "TiO$_2$ nanotubes and its composites: Photocatalytic and other photo-driven applications." *Journal of Materials Research* 28.03 (2013): 280-293.

[28] Zhelong Jiang, Yuxin Tang, Qiuling Tay, Yanyan Zhang, Oleksandr I. Malyi, Danping Wang, Jiyang Deng, Yuekun Lai, Huanfu Zhou, Xiaodong Chen, Zhili Dong, and Zhong Chen "Understanding the Role of Nanostructures for Efficient Hydrogen Generation on Immobilized Photocatalysts" *Advanced Energy Material* (2013): 3, 1368–1380.

[29] Dubey, Mukul, and Hongshan He. "Morphological and Photovoltaic Studies of TiO$_2$ NTs for High Efficiency Solar Cells." *In Scanning Electron Microscopy*. InTech, 2012.

[30] Yang, Peidong, ed. The chemistry of nanostructured materials. *World Scientific*, 2003.

[31] Xiao, Fang-Xing. "Construction of highly ordered ZnO–TiO$_2$ nanotube arrays (ZnO/TNTs) heterostructure for photocatalytic application." *ACS applied materials & interfaces* 4, no. 12 (2012): 7055-7063.

[32] Yongjing Lin, Guangbi Yuan, Rui Liu, Sa Zhou, Stafford W. Sheehan, Dunwei Wang "Semiconductor nanostructure-based photoelectrochemical water splitting: A brief review" *Chemical Physical Letters* 507, (2011): 209-215.

[33] Feng, Xinjian, Jan M. Macak, and Patrik Schmuki. "Flexible self-organization of two size-scales oxide nanotubes on Ti45Nb alloy." *Electrochemistry Communications* 9, no. 9 (2007): 2403-2407.

[34] Feng, Xinjian, Jan M. Macak, S. P. Albu, and Patrik Schmuki. "Electrochemical formation of self-organized anodic nanotube coating on Ti–28Zr–8Nb biomedical alloy surface." *Acta Biomaterialia* 4, no. 2 (2008): 318-323.

[35] Zwilling, Valérie, Marc Aucouturier, and Evelyne Darque-Ceretti. "Anodic oxidation of titanium and TA6V alloy in chromic media. An electrochemical approach." *Electrochimica Acta* 45, no. 6 (1999): 921-929.

[36] Gong, Dawei, Craig A. Grimes, Oomman K. Varghese, Wenchong Hu, R. S. Singh, Zhi Chen, and Elizabeth C. Dickey. "Titanium oxide nanotube arrays prepared by anodic oxidation." *Journal of Materials Research* 16, no. 12 (2001): 3331-3334.

[37] Beranek, R., H. Hildebrand, and Patrik Schmuki. "Self-organized porous titanium oxide prepared in H_2SO_4/HF electrolytes." *Electrochemical and solid-state letters* 6, no. 3 (2003): B12-B14.

[38] Taveira, L. V., Jan M. Macak, Hiroaki Tsuchiya, L. F. P. Dick, and Patrik Schmuki. "Initiation and growth of self-organized TiO_2 nanotubes anodically formed in $NH_4F/(NH_4)_2SO_4$ electrolytes." *Journal of the Electrochemical Society* 152, no. 10 (2005): B405-B410.

[39] Macak, Jan M., Hiroaki Tsuchiya, and Patrik Schmuki. "High-aspect-ratio TiO_2 nanotubes by anodization of titanium." *Angewandte Chemie International Edition* 44, no. 14 (2005): 2100-2102.

[40] Ghicov, Andrei, Hiroaki Tsuchiya, Jan M. Macak, and Patrik Schmuki. "Titanium oxide nanotubes prepared in phosphate electrolytes." *Electrochemistry Communications* 7, no. 5 (2005): 505-509.

[41] Macak, Jan M., Hiroaki Tsuchiya, Luciano Taveira, Saule Aldabergerova, and Patrik Schmuki. "Smooth anodic TiO₂ nanotubes." *Angewandte Chemie International Edition* 44, no. 45 (2005): 7463-7465.

[42] Ghicov, Andrei, Saule Aldabergenova, Hiroaki Tsuchyia, and Patrik Schmuki. "TiO₂–Nb₂O₅ nanotubes with electrochemically tunable morphologies." *Angewandte Chemie International Edition* 45, no. 42 (2006): 6993-6996.

[43] Yasuda, Kouji, and Patrik Schmuki. "Formation of self-Organized Zirconium Titanate nanotube layers by alloy anodization." *Advanced materials* 19, no. 13 (2007): 1757-1760.

[44] Tsuchiya, Hiroaki, Jan M. Macak, Andrei Ghicov, and Patrik Schmuki. "Self-Organization of Anodic Nanotubes on Two Size Scales." *Small* 2, no. 7 (2006): 888-891.

[45] Mor, Gopal K., Oomman K. Varghese, Maggie Paulose, Karthik Shankar, and Craig A. Grimes. "A review on highly ordered, vertically oriented TiO₂ nanotube arrays: fabrication, material properties, and solar energy applications." *Solar Energy Materials and Solar Cells* 90, no. 14 (2006): 2011-2075.

[46] Tsuchiya, Hiroaki, Jan M. Macak, Andrei Ghicov, Yee Chin Tang, Shinji Fujimoto, Mitsuo Niinomi, Toshiharu Noda, and Patrik Schmuki. "Nanotube oxide coating on Ti–29Nb–13Ta–4.6 Zr alloy prepared by self-organizing anodization." *Electrochimica Acta* 52, no. 1 (2006): 94-101.

[47] Liu, Qiang, Dongyan Ding, and Congqin Ning "Anodic fabrication of Ti-Nb-Zr-O nanotube arrays" *Journal of Nanomaterials*, Volume (2014): 1-7.

[48] Acevedo-Peña, Próspero, Federico González, Gonzalo González, and Ignacio González. "The effect of anatase crystal orientation on the photoelectrochemical performance of anodic TiO₂ nanotubes." *Physical Chemistry Chemical Physics* 16, no. 47 (2014): 26213-26220.

[49] Deyab, Nourhan M., Patrick Steegstra, Annick Hubin, Marie-Paule Delplancke, Hubert Rahier, and Nageh K. Allam. "Influence of electrolyte composition on the formation of mixed oxide nanotube arrays for solar fuel production." *Journal of power sources* 280, (2015): 339-346.

[50] Ning, Xuewen, Xixin Wang, Xiaofei Yu, Jiaxin Li, and Jianling Zhao. "Preparation and capacitance properties of Mn-doped TiO₂ nanotube arrays by anodisation of Ti–Mn alloy." *Journal of Alloys and Compounds* 658, (2016): 177-182.

[51] Jang, Seung-Hyun, Han-Cheol Choe, Yeong-Mu Ko, and William A. Brantley. "Electrochemical characteristics of nanotubes formed on Ti–Nb alloys." *Thin Solid Films* 517, no. 17 (2009): 5038-5043.

[52] Jin, Ming, Xin Lu, Yi Qiao, Lu-Ning Wang, and Alex A. Volinsky. "Fabrication and characterization of anodic oxide nanotubes on TiNb alloys." *Rare Metals* 35, no. 2 (2016): 140-148.

[53] Xu, Zhengchao, Qi Li, Shian Gao, and Jianku Shang. "Synthesis and characterization of niobium-doped TiO_2 nanotube arrays by anodization of Ti–20Nb alloys." *Journal of Materials Science & Technology* 28, no. 10 (2012): 865-870.

[54] Ding, Dongyan, Congqin Ning, Lin Huang, Fangchun Jin, Yongqiang Hao, Shuo Bai, Yan Li, Ming Li, and Dali Mao. "Anodic fabrication and bioactivity of Nb-doped TiO_2 nanotubes." *Nanotechnology* 20, no. 30 (2009): 1-6.

[55] Fornell, J., N. T. C. Oliveira, E. Pellicer, N. Van Steenberge, M. D. Baró, C. Bolfarini, and J. Sort. "Anodic formation of self-organized Ti (Nb, Sn) oxide nanotube arrays with tuneable aspect ratio and size distribution." *Electrochemistry Communications* 33, (2013): 84-87.

[56] Hernández-López, J. M., A. Conde, J. De Damborenea, and M. A. Arenas. "Correlation of the nanostructure of the anodic layers fabricated on Ti13Nb13Zr with the electrochemical impedance response." *Corrosion Science* 94 (2015): 61-69.

[57] Saji, Viswanathan S., Han Cheol Choe, and William A. Brantley. "An electrochemical study on self-ordered nanoporous and nanotubular oxide on Ti–35Nb–5Ta–7Zr alloy for biomedical applications." *Acta Biomaterialia* 5, no. 6 (2009): 2303-2310.

[58] Sieber, I., H. Hildebrand, A. Friedrich, and Patrik Schmuki. "Formation of self-organized niobium porous oxide on niobium." *Electrochemistry Communications* 7, no. 1 (2005): 97-100.

[59] Sieber, Irina V., and Patrik Schmuki. "Porous tantalum oxide prepared by electrochemical anodic oxidation." *Journal of the Electrochemical Society* 152, no. 9 (2005): C639-C644.

[60] Tsuchiya, Hiroaki, and Patrik Schmuki. "Thick self-organized porous zirconium oxide formed in H_2SO_4/NH_4F electrolytes." *Electrochemistry Communications* 6, no. 11 (2004): 1131-1134.

[61] Choe, H. C., Y. M. Ko, and William Arthur Brantley. "Nanotube formation and surface study of new ternary titanium alloys." *Proc NSTI-Nanotech Boston* 1, (2008): 454-457.

[62] Macak, Jan M., Hiroaki Tsuchiya, Luciano Taveira, Andrei Ghicov, and Patrik Schmuki. "Self-organized nanotubular oxide layers on Ti-6Al-7Nb and Ti-6Al-4V formed by anodization in NH4F solutions." *Journal of Biomedical Materials Research Part A* 75, no. 4 (2005): 928-933.

[63] Macak, Jan M., F. Schmidt-Stein, and Patrik Schmuki. "Efficient oxygen reduction on layers of ordered TiO_2 nanotubes loaded with Au nanoparticles." *Electrochemistry Communications* 9, no. 7 (2007): 1783-1787.

[64] Varghese, Oomman K., Dawei Gong, Maggie Paulose, Keat G. Ong, and Craig A. Grimes. "Hydrogen sensing using titania nanotubes." *Sensors and Actuators B: Chemical 93*, no. 1 (2003): 338-344.

[65] Breault, Tanya M., and Bart M. Bartlett. "Lowering the band gap of anatase-structured TiO2 by coalloying with Nb and N: electronic structure and photocatalytic degradation of methylene blue dye." *The Journal of Physical Chemistry C* 116, no. 10 (2012): 5986-5994.

[66] Zhao, Zhao, Xiaoyan Zhang, Guoqiang Zhang, Zhenyu Liu, Dan Qu, Xiang Miao, Pingyun Feng, and Zaicheng Sun. "Effect of defects on photocatalytic activity of rutile TiO_2 nanorods." *Nano Research* 8, no. 12 (2015): 4061-4071.

[67] Khan, Sovann, Haneol Cho, Donghun Kim, Sang Soo Han, Kyu Hwan Lee, So-Hye Cho, Taeseup Song, and Heechae Choi. "Defect engineering toward strong photocatalysis of Nb-doped anatase TiO 2: Computational predictions and experimental verifications." *Applied Catalysis B: Environmental* 206 (2017): 520-530.

[68] Zhu, Jiefang, and Michael Zäch. "Nanostructured materials for photocatalytic hydrogen production." *Current Opinion in Colloid & Interface Science* 14, no. 4 (2009): 260-269.

[69] Choi, Heechae, Sovann Khan, Junghyun Choi, Duong TT Dinh, Seung Yong Lee, Ungyu Paik, So-Hye Cho, and Seungchul Kim. "Synergetic control of band gap and structural transformation for optimizing TiO_2 photocatalysts." *Applied Catalysis B: Environmental* 210 (2017): 513-521.

[70] Cottineau, Thomas, Nicolas Béalu, Pierre-Alexandre Gross, Sergey N. Pronkin, Nicolas Keller, Elena R. Savinova, and Valérie Keller. "One step synthesis of niobium doped titania nanotube arrays to form (N, Nb) co-doped TiO_2 with high visible light photoelectrochemical activity." *Journal of Materials Chemistry A* 1, no. 6 (2013): 2151-2160.

[71] Mattsson, Andreas, Michael Leideborg, Karin Larsson, Gunnar Westin, and Lars Österlund. "Adsorption and solar light decomposition of acetone on anatase TiO_2 and niobium doped TiO_2 thin films." *The Journal of Physical Chemistry B* 110, no. 3 (2006): 1210-1220.

[72] Allam, Nageh K., Adam J. Poncheri, and Mostafa A. El-Sayed. "Vertically oriented Ti–Pd mixed oxynitride nanotube arrays for enhanced photoelectrochemical water splitting." *ACS nano* 5, no. 6 (2011): 5056-5066.

[73] Li, Yan, Dongyan Ding, Congqin Ning, Shuo Bai, Lin Huang, Ming Li, and Dali Mao. "Thermal stability and in vitro bioactivity of Ti–Al–V–O nanostructures fabricated on Ti6Al4V alloy." *Nanotechnology* 20, no. 6 (2009): 1-6.

[74] Mei, Bastian, Harriet Byford, Michal Bledowski, Lidong Wang, Jennifer Strunk, Martin Muhler, and Radim Beranek. "Beneficial effect of Nb doping on the photoelectrochemical properties of TiO_2 and TiO_2-polyheptazine hybrids." *Solar Energy Materials and Solar Cells* 117 (2013): 48-53.

[75] Xu, Li, Gaorui Liang, and Ming Yin. "A promising electrode material modified by Nb-doped TiO_2 nanotubes for electrochemical degradation of AR 73." *Chemosphere* 173 (2017): 425-434.

[76] Ozkan, Selda, Anca Mazare, and Patrik Schmuki. "Extracting the limiting factors in photocurrent measurements on TiO_2 nanotubes and enhancing the photoelectrochemical properties by Nb doping." *Electrochimica Acta* 176 (2015): 819-826.

[77] Allam, Nageh K., Faisal Alamgir, and Mostafa A. El-Sayed. "Enhanced photoassisted water electrolysis using vertically oriented anodically fabricated Ti− Nb− Zr− O mixed oxide nanotube arrays." *ACS nano* 4, no. 10 (2010): 5819-5826.

[78] Xu, Zhengchao, Weiyi Yang, Qi Li, Shian Gao, and Jian Ku Shang. "Passivated n–p co-doping of niobium and nitrogen into self-organized TiO_2 nanotube arrays for enhanced visible light photocatalytic performance." *Applied Catalysis B: Environmental* 144 (2014): 343-352.

[79] Yang, Min, Himendra Jha, Ning Liu, and Patrik Schmuki. "Increased photocurrent response in Nb-doped TiO_2 nanotubes." *Journal of Materials Chemistry* 21, no. 39 (2011): 15205-15208.

[80] Zorn, G., A. Lesman, and I. Gotman. "Oxide formation on low modulus Ti45Nb alloy by anodic versus thermal oxidation." *Surface and Coatings Technology* 201, no. 3 (2006): 612-618.

[81] Grimes, Craig A., and Gopal K. Mor. *TiO_2 nanotube arrays: synthesis, properties, and applications*. Springer Science & Business Media, 2009.

[82] Gao, Xianfeng, Junhong Chen, and Chris Yuan. "Enhancing the performance of free-standing TiO_2 nanotube arrays based dye-sensitized solar cells via ultraprecise control of the nanotube wall thickness." *Journal of Power Sources* 240 (2013): 503-509.

[83] Liang, Suzhen, Jingfu He, Zhihu Sun, Qinghua Liu, Yong Jiang, Hao Cheng, Bo He, Zhi Xie, and Shiqiang Wei. "Improving photoelectrochemical water splitting activity of TiO_2 nanotube arrays by tuning geometrical parameters." *The Journal of Physical Chemistry C* 116, no. 16 (2012): 9049-9053.

[84] Wu, C., Y. Zhuo, P. Zhu, Bo Chi, Jian Pu, and Jian Li. "Tunable fabrication of TiO_2 nanotube arrays with high aspect ratio and its application in dye sensitized solar cell." *Journal of Inorganic Materials* 24, no. 5 (2009): 897-901.

[85] Amer, Ahmad W., Seifallah M. Mohamed, Ahmed M. Hafez, Siham Y. AlQaradawi, Amina S. Aljaber, and Nageh K. Allam. "Self-assembled zirconia nanotube arrays: fabrication mechanism, energy consideration and optical activity." *RSC Advances* 4, no. 68 (2014): 36336-36343.

[86] Mohamed, Ahmad M., Amina S. Aljaber, Siham Y. AlQaradawi, and Nageh K. Allam. "TiO_2 nanotubes with ultrathin walls for enhanced water splitting." *Chemical Communications* 51, no. 63 (2015): 12617-12620.

[87] Nowotny, Janusz, Mohammad Abdul Alim, Tadeusz Bak, Mohammad Asri Idris, Mihail Ionescu, Kathryn Prince, Mohd Zainizan Sahdan, Kamaruzzaman Sopian, Mohd Asri Mat Teridi, and Wolfgang Sigmund. "Defect chemistry and defect engineering of TiO_2-based semiconductors for solar energy conversion." *Chemical Society Reviews* 44, no. 23 (2015): 8424-8442.

[88] Lin, Zhong, Bruno R. Carvalho, Ethan Kahn, Ruitao Lv, Rahul Rao, Humberto Terrones, Marcos A. Pimenta, and Mauricio Terrones. "Defect engineering of two-dimensional transition metal dichalcogenides." *2D Materials* 3, no. 2 (2016): 1-21.

[89] M. Saleem, M.F. Al-Kuhaili, S.M.A. Durrani, A.H.Y. Hendi, I.A. Bakhtiari, S. Ali "Influence of hydrogen annealing on the optoelectronic properties of WO_3 thin films" *International Journal of Hydrogen Energy* 40 (2015): 12343-12351.

[90] KuechGroup. "Defect Engineering and Nanoscopic Process." AMPS. November 16, 2017. http://amps.che.wisc.edu/research_defecteng.php

[91] Marchiori, Chiara, Giovanni Di Liberto, Guido Soliveri, Laura Loconte, Leonardo Lo Presti, Daniela Meroni, Michele Ceotto et al. "Unraveling the cooperative mechanism of visible-light absorption in bulk N, Nb codoped TiO_2 powders of nanomaterials." *The Journal of Physical Chemistry C* 118, no. 41 (2014): 24152-24164.

[92] Shaheen, Basamat Saif El Din. "Towards efficient photoanodes for solar fuel production." M.Sc. thesis, The American University in Cairo, 2014.

[93] Das, Chittaranjan, Poulomi Roy, Min Yang, Himendra Jha, and Patrik Schmuki. "Nb doped TiO_2 nanotubes for enhanced photoelectrochemical water-splitting." *Nanoscale* 3, no. 8 (2011): 3094-3096.

[94] Saji, Viswanathan S., Han Cheol Choe, and William A. Brantley. "Nanotubular oxide layer formation on Ti–13Nb–13Zr alloy as a function of applied potential." *Journal of materials science* 44, no. 15 (2009): 3975-3982.

[95] Yang, Min, Guang Yang, Erdmann Spiecker, Kiyoung Lee, and Patrik Schmuki. "Ordered "superlattice" TiO2/Nb2O5 nanotube arrays with improved ion insertion stability." *Chemical Communications* 49, no. 5 (2013): 460-462.

[96] Barea, Eva, Xueqing Xu, Victoria González-Pedro, Teresa Ripollés-Sanchis, Francisco Fabregat-Santiago, and Juan Bisquert. "Origin of efficiency enhancement in Nb_2O_5 coated titanium dioxide nanorod based dye sensitized solar cells." *Energy & Environmental Science* 4, no. 9 (2011): 3414-3419.

[97] Lim, Jonghun, Palanichamy Murugan, Narayanan Lakshminarasimhan, Jae Young Kim, Jae Sung Lee, Sang-Hyup Lee, and Wonyong Choi. "Synergic photocatalytic effects of nitrogen and niobium co-doping in TiO 2 for the redox conversion of aquatic pollutants under visible light." *Journal of Catalysis* 310 (2014): 91-99.

[98] Sun, Yan, Kangping Yan, Guixin Wang, Wei Guo, and Tingli Ma. "Effect of annealing temperature on the hydrogen production of TiO_2 nanotube arrays in a two-compartment photoelectrochemical cell." *The Journal of Physical Chemistry C* 115, no. 26 (2011): 12844-12849.

[99] Prabu, K. Monikanda, and S. Perumal. "Micro Strain and Morphological Studies of Anatase and Rutile Phase TiO_2 Nanocrystals Prepared via Sol-Gel and Solvothermal Method-A Comparative Study." (2015).

[100] Manikandan, K., S. Arumugam, and G. Chandrasekaran. "Effect of annealing temperature on titania nanoparticles." In *AIP Conference Proceedings*, vol. 1591, no. 1, pp. 128-130. AIP, 2014.

[101] Pei, Linjuan, Min Yang, Dan Zhang, Lei Zhang, Peng Chen, Yanyan Song, and Yang Gan. "Photoelectrochemical activities and low content Nb-doping effects on one-dimensional self-ordered Nb_2O_5–TiO_2 nanotubes." *Rsc Advances* 5, no. 12 (2015): 9138-9142.

[102] Arbiol, J., J. Cerda, G. Dezanneau, A. Cirera, F. Peiro, A. Cornet, and J. R. Morante. "Effects of Nb doping on the TiO_2 anatase-to-rutile phase transition." *Journal of Applied Physics* 92, no. 2 (2002): 853-861.

[103] Suryanarayana, Challapalli, and M. Grant Norton. *X-ray diffraction: a practical approach.* Springer Science & Business Media, 2013.

[104] Fehse, Marcus, Sara Cavaliere, P. E. Lippens, Iuliia Savych, A. Iadecola, Laure Monconduit, D. J. Jones et al. "Nb-doped TiO_2 nanofibers for lithium ion batteries." *The Journal of Physical Chemistry C* 117, no. 27 (2013): 13827-13835.

[105] Hanzu, Ilie, Thierry Djenizian, and Philippe Knauth. "Electrical and point defect properties of TiO2 nanotubes fabricated by electrochemical anodization." *The Journal of Physical Chemistry C* 115, no. 13 (2011): 5989-5996.

[106] Sheppard, L. R., T. Dittrich, and M. K. Nowotny. "The impact of niobium surface segregation on charge separation in niobium-doped titanium dioxide."*The Journal of Physical Chemistry C* 116, no. 39 (2012): 20923-20929.

[107] Lamberti, Andrea, Angelica Chiodoni, Nadia Shahzad, Stefano Bianco, Marzia Quaglio, and Candido F. Pirri. "Ultrafast room-temperature crystallization of TiO_2 nanotubes exploiting water-vapor treatment." *Scientific reports* 5 (2015).

[108] Xing, Junheng, Hui Li, Zhengbin Xia, Jiangqiong Chen, Yanhong Zhang, and Li Zhong. "Influence of substrate morphology on the growth and properties of TiO_2 nanotubes in HBF_4-based electrolyte." *Electrochimica Acta* 134 (2014): 242-248.

[109] Xu, Xijin, Chengchun Tang, Haibo Zeng, Tianyou Zhai, Shanqing Zhang, Huijun Zhao, Yoshio Bando, and Dmitri Golberg. "Structural transformation, photocatalytic, and field-emission properties of ridged TiO_2 nanotubes." *ACS applied materials & interfaces* 3, no. 4 (2011): 1352-1358.

[110] Kang, Soon Hyung, Jae-Yup Kim, Hyun Sik Kim, and Yung-Eun Sung. "Formation and mechanistic study of self-ordered TiO_2 nanotubes on Ti substrate." *Journal of Industrial and Engineering Chemistry* 14, no. 1 (2008): 52-59.

[111] Maiyalagan, T., B. Viswanathan, and U. V. Varadaraju. "Fabrication and characterization of uniform TiO_2 nanotube arrays by sol--gel template method." *Bulletin of Materials Science* 29, no. 7 (2006).

[112] Tian, Fang, Yupeng Zhang, Jun Zhang, and Chunxu Pan. "Raman spectroscopy: a new approach to measure the percentage of anatase TiO_2 exposed (001) facets." *The Journal of Physical Chemistry C* 116, no. 13 (2012): 7515-7519.

[113] Yu, Ying, C. Yu Jimmy, Jia-Guo Yu, Yuk-Chun Kwok, Yan-Ke Che, Jin-Cai Zhao, Lu Ding, Wei-Kun Ge, and Po-Keung Wong. "Enhancement of photocatalytic activity of mesoporous TiO_2 by using carbon nanotubes." *Applied Catalysis A: General* 289, no. 2 (2005): 186-196.

[114] Hardcastle, F. D. "Raman spectroscopy of titania (TiO_2) nanotubular water-splitting catalysts." *Journal of the Arkansas Academy of Science* 65, no. 1 (2011): 43-48.

[115] Pittman, Rusty M., and Alexis T. Bell. "Raman studies of the structure of niobium oxide/titanium oxide ($Nb_2O_5.TiO_2$)." *The Journal of Physical Chemistry* 97, no. 47 (1993): 12178-12185.

[116] Regonini, Domenico, A. Jaroenworaluck, R. Stevens, and Christopher R. Bowen. "Effect of heat treatment on the properties and structure of TiO_2 nanotubes: phase composition and chemical composition." *Surface and interface analysis* 42, no. 3 (2010): 139-144.

[117] Gautam, Subodh K., Arkaprava Das, S. Ojha, D. K. Shukla, D. M. Phase, and Fouran Singh. "Electronic structure modification and Fermi level shifting in niobium-doped anatase titanium dioxide thin films: a comparative study of NEXAFS, work function and stiffening of phonons." *Physical Chemistry Chemical Physics* 18, no. 5 (2016): 3618-3627.

[118] Ou, Jian Zhen, Rozina A. Rani, Moon-Ho Ham, Matthew R. Field, Yuan Zhang, Haidong Zheng, Peter Reece et al. "Elevated temperature anodized Nb_2O_5: a photoanode material with exceptionally large photoconversion efficiencies." *ACS nano* 6, no. 5 (2012): 4045-4053.

[119] Roguska, A., A. Kudelski, M. Pisarek, M. Lewandowska, M. Dolata, and M. Janik-Czachor. "Raman investigations of TiO_2 nanotube substrates covered with thin Ag or Cu deposits." *Journal of Raman Spectroscopy* 40, no. 11 (2009): 1652-1656.

[120] Zhu, Kai, Nathan R. Neale, Alexander Miedaner, and Arthur J. Frank. "Enhanced charge-collection efficiencies and light scattering in dye-sensitized solar cells using oriented TiO_2 nanotubes arrays." *Nano letters* 7, no. 1 (2007): 69-74.

[121] Hussein Znad, Ming H. Ang, and Moses O. Tade "Ta/TiO2 -and Nb/TiO2 -Mixed Oxides as Efficient Solar Photocatalysts: Preparation, Characterization, and Photocatalytic Activity" *International Journal of Photoenergy*, 2012.

[122] Yoon, Songhak, Alexandra E. Maegli, Arnim Eyssler, Matthias Trottmann, Takashi Hisatomi, Céline Marie Leroy, Michael Grätzel, and Anke Weidenkaff. "Synthesis and characterization of La (Ti, Nb)(O, N)$_3$ for photocatalytic water oxidation." *Energy Procedia* 22 (2012): 41-47.

[123] Samir, Menna, Mohamed Salama, and Nageh K. Allam. "Sub-100 nm TiO_2 tubular architectures for efficient solar energy conversion." *Journal of Materials Chemistry A* 4, no. 24 (2016): 9375-9380.

[124] Freitas, R. G., M. A. Santanna, and E. C. Pereira. "Dependence of TiO_2 nanotube microstructural and electronic properties on water splitting." *Journal of Power Sources* 251 (2014): 178-186.

[125] Regonini, Domenico, A. Schmidt, C. G. Aneziris, T. Graule, and F. J. Clemens. "Impact of the Anodizing Potential on the Electron Transport Properties of Nb-doped TiO_2 Nanotubes." *Electrochimica Acta* 169 (2015): 210-218.

[126] Zhang, Zhonghai, Md Faruk Hossain, and Takakazu Takahashi. "Photoelectrochemical water splitting on highly smooth and ordered TiO_2 nanotube arrays for hydrogen generation." *International journal of hydrogen energy* 35, no. 16 (2010): 8528-8535.

[127] Paulose, Maggie, Gopal K. Mor, Oomman K. Varghese, Karthik Shankar, and Craig A. Grimes. "Visible light photoelectrochemical and water-photoelectrolysis properties of titania nanotube arrays." *Journal of photochemistry and photobiology A: Chemistry* 178, no. 1 (2006): 8-15.